ORBITALLY EXCITED CHARM-STRANGE MESONS

A DISSERTATION
SUBMITTED TO THE DEPARTMENT OF PHYSICS
AND THE COMMITTEE ON GRADUATE STUDIES
OF ILLINOIS INSTITUTE OF TECHNOLOGY
IN PARTIAL FULFILLMENT OF THE REQUIREMENTS
FOR THE DEGREE OF
DOCTOR OF PHILOSOPHY

PENELOPE A. KASPER
May 1996

Contents

List of Tables

List of Figures

Chapter 1

THEORETICAL MOTIVATION

1.1 Introduction

This thesis describes an attempt to measure the properties of mesons containing a charm quark and a strange quark in a state of orbital angular momentum $L > 0$, and compare these with the predictions of theoretical models based on heavy quark effective theory. The study of mesons containing one heavy quark and one light quark is an ideal testing ground for the one-body problem in hadron physics. As the heavy quark's mass increases, its motion decreases approaching the behavior of a fixed force center. Thus the meson's properties will increasingly be governed by the dynamics of the light quark which will approach a universal limit [1].

The c and b quarks have masses which are much greater than the QCD scale Λ_{QCD}. The physics of hadrons containing one of these quarks is greatly simplified by using an effective theory constructed by taking the limit of QCD where the masses of such heavy quarks go to infinity with their four-velocities fixed. In this limit, new symmetries appear which can be used to predict the properties of such hadrons [2]. (Top quarks decay before they form hadrons.) For mesons containing a heavy quark of finite mass m_Q these symmetries are broken by effects of order Λ_{QCD}/m_Q. Because $m_b \gg \Lambda_{QCD}$, heavy quark symmetry should provide an excellent description of the B and B_s mesons. It is plausible that the properties of D mesons and even K mesons should also reflect approximate heavy-quark symmetry.

Table 1.1: Quark Model of $L = 0$ Heavy-Light Mesons

S_Q	$S_{\overline{q}}$	S	L	J^p	Meson
1/2	1/2	0	0	0^-	D^0, B^0
		1		1^-	D^*,B^*

The lowest lying states containing a light antiquark and a heavy quark (denoted $\overline{q}$ and Q respectively) are the $\overline{K}$, D and $\overline{B}$ mesons corresponding to relative angular momentum $L = 0$ and spin singlets. The spin triplet states $\overline{K^*}(892)$, $D^*(2010)$ and $\overline{B^*}(5325)$ have also been identified and their spacings from the spin singlet states are consistent with the expected $1/m_Q$ approach to the heavy quark limit.

$$\frac{m(D^*) - m(D)}{m(B^*) - m(B)} = \frac{145 MeV/c^2}{46 MeV/c^2} = 3.15 \approx \frac{m(b)}{m(c)} \tag{1.1}$$

The next lightest $Q\overline{q}$ states are the $L = 1$ (p-wave) states. There are expected to be 4 $L = 1$ states for each $Q\overline{q}$ pair: a spin singlet state ($J^p = 1^+$), and 3 spin triplet states ($J^p = 0^+, 1^+, 2^+$). Hence there are 12 p-wave charm mesons corresponding to the light quark being u, d or s. The charm p-wave mesons are known as D^{**} states. The first p-wave charm meson was reported by the ARGUS collaboration in 1985 [3]. Since then six of the twelve expected p-wave charm states have been observed [4]-[17]. The other six are expected to be very wide and hence difficult to identify.

Evidence for the existence of orbitally excited B meson states has been reported recently [18]. The B^{**} states would be particularly useful in tagging B^0 and $\overline{B}^0$ to study CP violation. If we can identify all the D^{**} states we may see how well we can expect the models to predict the B^{**} states. An understanding of the charm hadrons is also needed because the beauty hadrons decay to charm hadrons and, for making measurements on beauty hadrons, a good knowledge of the decay products is essential [20].

Falk and Peskin [21] have recently pointed out that heavy quark spin symmetry

Table 1.2: Quark Model of $L = 1$ Heavy-Light Mesons

$S_{\overline{q}}$	L	$j^p(\overline{q})$	S_Q	J^p	Meson
1/2	1	$\frac{1}{2}^+$	1/2	0^+, 1^+	D_0, $D_1(j = 1/2)$
		$\frac{3}{2}^+$		1^+, 2^+	$D_1(j = 3/2)$, D_2

provides strong constraints on the helicity probabilities of the heavy mesons produced by the fragmentation/hadronization of a heavy quark. They show the possibility of detecting a net polarization of the initial heavy quark from the angular distribution of the decay products. They define a parameter w_j which can be determined from this angular distribution. This is discussed in more detail in Section 1.5.

1.2 Masses of P-wave Mesons With One Heavy Quark

Heavy-quark systems can be well described by non-relativistic potential models [24],[25]. Almost all phenomenological models parametrize the spin-independent part of the inter-quark interaction with a Coulomb type potential due to single gluon exchange and a linear confining potential. The $L = 1$ charm mesons probe the inter-quark potential at larger distances than charmonium. Heavy Quark Effective Theory uses the symmetries of the heavy quark limit to predict mass splittings and relationships between different decay amplitudes.

In the heavy quark approximation the only non-zero spin-dependent part of the inter-quark potential is the spin-orbit interaction of the light quark. For mesons with non-zero orbital angular momentum the total spin $(S_q + S_Q)$ is no longer a good quantum number. Instead the light quark's spin couples to the orbital angular momentum and the energy levels are characterized by $j = L + S_{\overline{q}}$, the total angular momentum of the light quark.

For $L = 1$ mesons, taking the heavy mass limit results in two degenerate $j = 3/2$ states (2^+ and 1^+) and two degenerate $j = 1/2$ states (1^+ and 0^+), see Table 1.2. For a finite mass heavy quark the mass splitting within a doublet is expected to be inversely proportional to the mass of the heavy quark. The excited kaon states identified as the $j = 3/2$ doublet are the $K_1(1270)$ and the $K_2^*(1430)$ with a mass difference of 160 MeV/c^2. The excited charm states identified as the $j = 3/2$ doublet are the $D_1(2420)$ and the $D_2^*(2460)$ with a mass difference of 40 MeV/c^2. This change in mass splitting is consistent with the expected $1/m_Q$ variation. Note that for a finite mass heavy quark the two $J = 1$ states can mix, so the observed states may not be pure $j = 3/2$ and $j = 1/2$ in this case. Table 1.3 compares theoretical and experimental values of masses of p-wave mesons.

1.3 Decay Properties of P-wave Mesons

A successful model of hadrons must address not only hadronic spectra but also the internal structures of hadronic systems. Of course a spectrum and its associated quantum numbers (spin, parity, isospin etc.) depend on this structure but the most sensitive measures of the internal structure of hadrons are their couplings to other hadrons and to electromagnetic and weak currents.

The $L = 1$ charm mesons decay strongly, mostly through two-body decays. Table 1.4 shows the allowed two-body decay modes of the p-wave charm mesons. Note that the relative angular momentum of the decay products must be even to conserve parity. It can be seen that the spin 2 state decays via a D-wave to either a D^* or D, the spin 1 state decays via either a D-wave or S-wave to a D^* and the spin zero state decays via an S-wave to a D.

Heavy quark symmetry predicts that all strong decay amplitudes arising from the emission of light quanta such as π, ρ, etc., are independent of heavy quark flavor. Also, for a given flavor, the two states of a doublet (defined by the angular momentum of the light quark) should have the same total width, and the ratio of partial widths is predicted by the theory. The decays of excited mesons are usually described by the emission of a pseudoscalar particle from a quark [26]. In this model the amplitudes

Table 1.3: Comparison of Theoretical and Experimental Masses of P-wave Mesons

		Theory			Experiment				
$Q\bar{q}$	J_j	*DeR*[13] *Gev*	*GK*[5] *Gev*	*EHQ*[9] *Gev*	*E687*[35] *Gev*	*ARGUS* [28] – [34] *Gev*	*CLEO* [24] – [27] *Gev*	*PDG*[39] *Gev*	*DELP*[38] *Gev*
$s\bar{u}$	$2_{3/2}$		1.43					1.43	
	$1_{3/2}$		1.37					1.40	
	$1_{1/2}$		1.35					1.27	
	$0_{1/2}$		1.24					1.43	
$c\bar{u}$	$2_{3/2}$	2.42	2.50		2.453	2.455	2.465		
					2.453	2.469			
	$1_{3/2}$	2.39	2.47		2.422		2.421		
	$1_{1/2}$	2.31	2.46						
	$0_{1/2}$	2.30	2.40						
$c\bar{s}$	$2_{3/2}$	2.57	2.59	2.537			2.573		
	$1_{3/2}$	2.55	2.56	2.502	2.535	2.535	2.535		
	$1_{1/2}$	2.525	2.55						
	$0_{1/2}$	2.52	2.48						
$b\bar{u}$	$2_{3/2}$		5.80	5.767					5.732*
	$1_{3/2}$		5.78	5.755					
	$1_{1/2}$		5.78						
	$0_{1/2}$		5.76						
$b\bar{s}$	$2_{3/2}$		5.88	5.846					
	$1_{3/2}$		5.86	5.834					
	$1_{1/2}$		5.86						
	$0_{1/2}$		5.83						

* Delphi have observed a single broad resonance which is not assigned any spin parity.

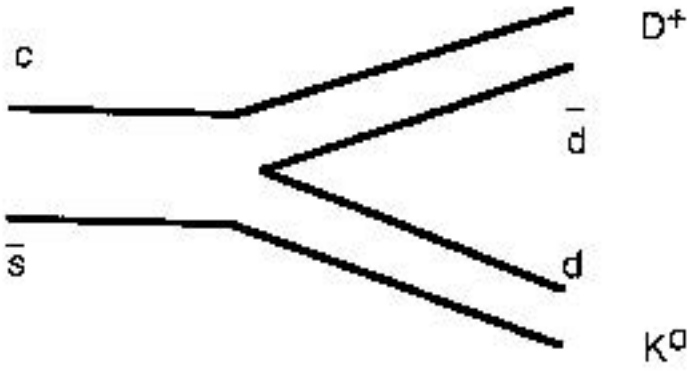

Figure 1.1: Feynman Diagrams for the Decay of a Charm-Strange P-wave Meson

Table 1.4: Two-body Decay Modes for P-wave Charm Mesons

initial state	final state			
J^P	$J_1^{P_1}$	$J_2^{P_2}$	relative angular momentum	example decay
2^+	1^-	0^-	2	$D_{s2}^{**} \to D^{*+}K_S$
	0^-	0^-	2	$D_{s2}^{**} \to D^+K_S$
1^+	1^-	0^-	0	$D_{s1}^{**} \to D^{*+}K_S$
	1^-	0^-	2	$D_{s1}^{**} \to D^{*0}K^+$
0^+	0^-	0^-	0	$D_{s0}^{**} \to D^0K^+$

Table 1.5: P-wave Meson Decay Amplitudes

Initial State	Final state	Decay Width [1] excluding kinematic factors
2^+	$1^-\ 0^-$	$\frac{3}{10}D^2$
	$0^-\ 0^-$	$\frac{1}{5}D^2$
$1^+(3/2)$	$1^-\ 0^-$	$\frac{1}{5}D^2$
$1^+(1/2)$	$1^-\ 0^-$	$\frac{1}{2}S^2$
0^+	$0^-\ 0^-$	$\frac{1}{2}S^2$

for the decay of p-wave mesons can be described by two real parameters S and D corresponding to S- and D-wave decays [26, 1]. The decay amplitudes are shown in Table 1.5. It can be seen that in the heavy quark limit the $j = 1/2$ state decays only through an S-wave, while the $j = 3/2$ state decays only through a D-wave.

While heavy quark symmetry does not relate S-wave to D-wave decay amplitudes, the constituent quark model suggests that S-wave decay amplitudes are very strong. This may explain the difficulty in observing members of the $j = 1/2^+$ mulitplets which consequently are expected to have large widths. Since the quark model predicts that S-wave widths are an order of magnitude larger than the D-wave widths even a weak mixing of the $J = 1$ states with $j = 1/2$ and $j = 3/2$ could have a substantial effect on the widths of the $j = 3/2^+$ D_1 states. Note also that the partial widths are proportional to q^{2L+1} where q is the momentum of the final state mesons in the center of mass of the decaying meson and L is the relative angular momentum of the final state mesons. This means that for decays close to threshold such as $D_s^{**} \to D^*K$ the D-wave amplitude will be suppressed. Table 1.6 compares theoretical and experimental values of the widths of p-wave mesons.

Table 1.6: Comparison of Theoretical and Experimental Widths of P-wave Mesons

		Theory			Experiment		
$Q\overline{q}$	J_j	Ros[1] MeV/c^2	GK[26] MeV/c^2	EHQ[28] MeV/c^2	E687[16] Mev/c^2	ARGUS [3]-[14] MeV/c^2	CLEO [5]-[8] MeV/c^2
$c\overline{u}$	$2_{3/2}$	37	63	28	25± 10	15± 12	20± 10
	$1_{3/2}$	24	26	18	15± 8	14± 6	23± 7
	$1_{1/2}$		250				
	$0_{1/2}$		290				
$c\overline{s}$	$2_{3/2}$		21	7			16± 5
	$1_{3/2}$		0.3	< 1	< 3.2	< 3.9	< 2.3
	$1_{1/2}$		140				
	$0_{1/2}$		310				

1.4 Properties of P-wave Charm-Strange Mesons

The p-wave $c\bar{s}$ states can decay to D^*K or DK. Two states have been observed at masses of 2535 Mev/c^2 [10, 16] and 2573 Mev/c^2 [6], the first decaying to D^*K and the second to DK. The state at 2535 MeV/c^2 is thought to be the $J = 1$, $j = 3/2$ state. It would be useful to confirm the spin of this D^*K resonance. If the D^{**} is produced unpolarized then its spin cannot be determined from the angular distribution of its decay. However the spin of the D^{**} determines the helicity of the daughter D^*.

The helicity λ of the D^* governs the distribution with respect to the angle θ between the K and the π from the D^* decay in the D^* rest frame (see Figure 1.2).

$$W(\theta) = \begin{cases} \frac{3}{2}\sin^2\theta & \lambda = \pm 1 \\ 3\cos^2\theta & \lambda = 0 \end{cases} \tag{1.2}$$

The helicity distribution of the D^*s from D^{**} decay is determined by the Clebsch-Gordon coefficients. A pure D-wave decay of a spin 2 object leads to

$$W(\theta) = \frac{3}{2}\sin^2\theta \tag{1.3}$$

while the decay of a spin 1 resonance leads to

$$W(\theta) = \begin{cases} (1 + 3\cos^2\theta)/2 & \text{(pure D-wave)} \\ 1 & \text{(pure S-wave)} \end{cases} \tag{1.4}$$

Measurement of this angular distribution would determine the spin of the state at 2535 Mev/c^2.

CLEO has observed a peak in the D^0K^+ mass spectrum at 2573 Mev/c^2 which they suggest is the 2^+ state. The allowed decay modes of the 2^+ state are DK and D^*K but the latter is expected to be suppressed because of limited phase space. Godfrey and Kokoski [26] predict the partial width for the decay to DK to be 6 to 10 times that for the decay to D^*K. The decay to $D_s\pi^0$ is forbidden by isospin conservation.

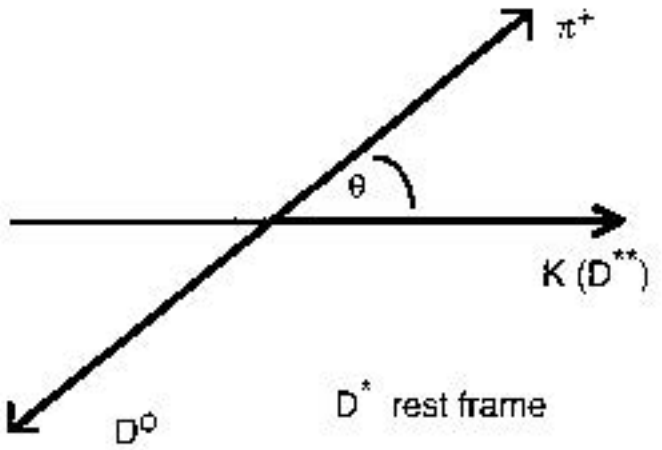

Figure 1.2: Kinematics for a state decaying to $D^{*+}K^0$ followed by $D^{*+} \to D^0\pi^+$

1.5 Polarization of Excited Heavy Mesons

Falk and Peskin [21] discuss the production via fragmentation of excited heavy mesons and baryons and explore the possibility of detecting a net polarization of the initial heavy quark, either in a polarization of the final state or in anisotropies in the decay products of the excited hadron. They begin with a heavy quark ejected at relativistic speed from a hard reaction. This process is typically calculable in perturbation theory and is completed in a short time compared to the time scale of the nonperturbative strong interactions. Over a longer time scale, a fragmentation process occurs which eventually forms a physical hadron containing the heavy quark. The axis linking the center-of-mass frame of the heavy quark to the center-of-mass of the hard process is a preferred direction which is called the fragmentation axis. The z axis is taken to be along this line. For a system of light degrees of freedom of spin j, they define the Falk-Peskin parameter w_j as the probability that fragmentation leads to a state with the maximum value of $|j^z|$. The parameter w_j takes values between 0 and 1. (See Figure 1.3)

We will consider the case where $j = 3/2$. For a meson with $J = 2$ the spin of the heavy quark must be along the same direction as j. In the decay $D^{**}_{s2} \to DK$ let θ denote the angle between the kaon and the fragmentation axis in the D^{**} rest frame.

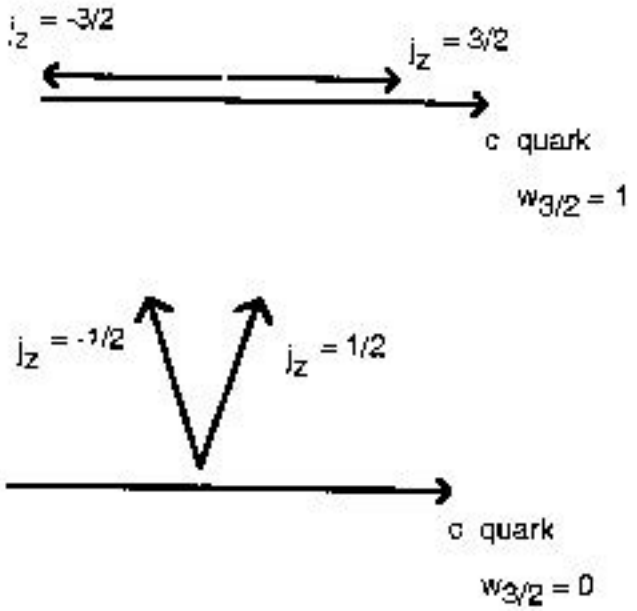

Figure 1.3: Helicity states for extreme values of $w_{3/2}$

(See Figure 1.4) The angular distribution for this decay is given by

$$\frac{1}{\Gamma}\frac{d\Gamma}{d\cos\theta} = \frac{1}{4}[1 + 3\cos^2\theta - 6w_{3/2}(\cos^2\theta - 1/3)] \tag{1.5}$$

The Falk-Peskin parameter $w_{3/2}$ can be extracted from experiment if the angular distribution is measured. This angular distribution has been measured by ARGUS [9, 12] for the non strange D^{**} and the results suggest that $w_{3/2}$ is close to zero. Once $w_{3/2}$ is known one can make predictions for the angular distributions of the remaining excited D meson decays.

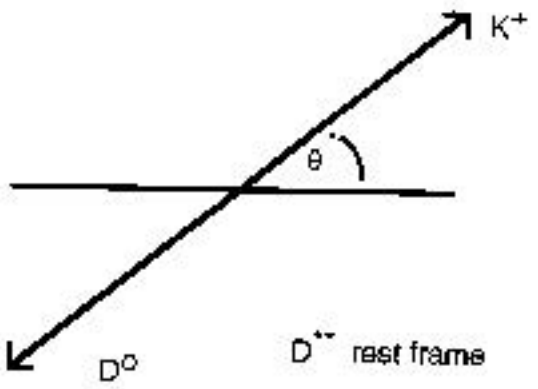

Figure 1.4: Decay angle for $D_s^{**} \to D^0 K^+$

Chapter 2

THE TAGGED PHOTON SPECTROMETER

Fermilab Experiment E791 is a high statistics charm particle experiment which took data at the Tagged Photon Laboratory (TPL) during the 1991 fixed target run. It was the fourth in a series of charm experiments using the Tagged Photon Spectrometer. Over 20 billion events were recorded and the aim of reconstructing 100,000 charm decays has been well exceeded. The spectrometer is shown in Figure 2.1 and is described in detail in this chapter.

2.1 The Beam

The Fermilab Tevatron accelerates protons to an energy of 800 GeV. During the 1991 fixed target run it operated on a cycle of 57 seconds accelerating the protons for 34 sec (the interspill period), then slowly extracting them over a 23 second spill. The beam was sent to the switchyard where it was split into three beams for the Proton, Meson and Neutrino areas. The beam for the proton area was split further into the P-west, P-center, P-east and Wide-band beams. The Tagged Photon Lab is in the P-east beamline. The layout of the accelerator and beamlines is shown in Figure 2.2. The beam for the experiment was created by the 800 GeV/c protons from the Tevatron interacting with a 30 cm beryllium target. The secondary beamline magnets were

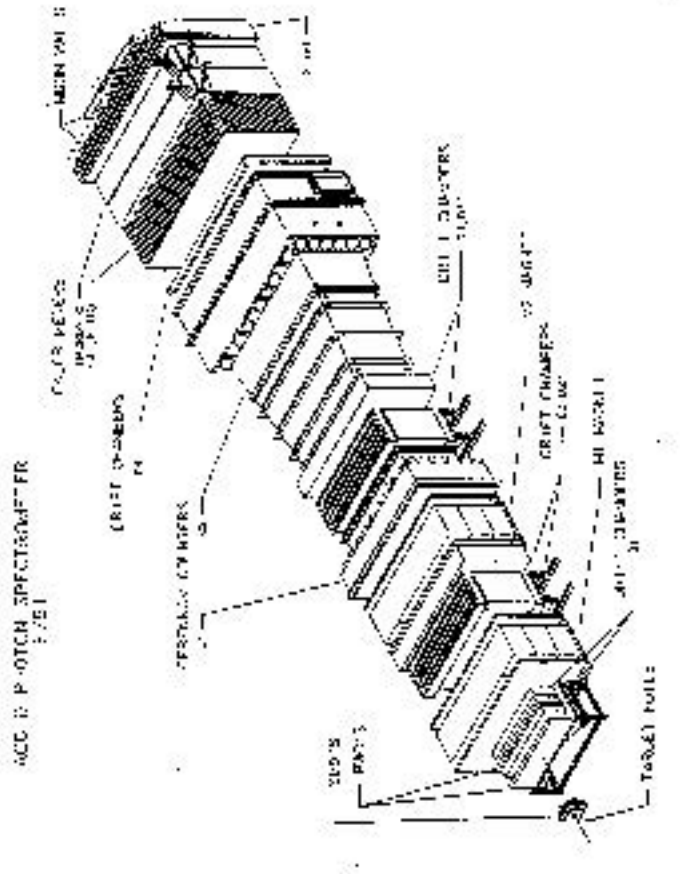

Figure 2.1: E791 Spectrometer

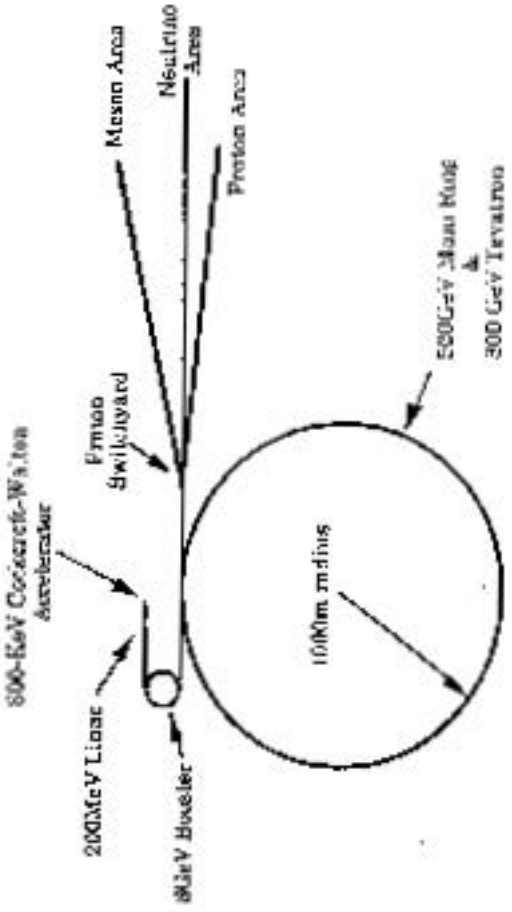

Figure 2.2: Fermilab Tevatron and Experimental Areas [30]

tuned to transport negative particles with a momentum of 500 GeV/c downstream to the E791 target in TPL. The beam consisted mostly of pions (98%). The first two experiments at TPL used a photon beam and although high energy photons produce more charm per hadronic interaction it is possible to get a higher intensity with a pion beam. A negative beam was used to avoid proton contamination.

During the run we took about 2×10^{12} primary protons per spill which resulted in about 2×10^{6} secondary pions per second incident on our target. The beam profile on planes 5 and 6 (x and y directions) of the Silicon Microstrip detectors (SMDs), just upstream of the target, is shown in Figure 2.3.

2.2 The Target

The target consisted of five disks each about 1 cm in diameter. The most upstream target disk was platinum 0.5 mm thick and the other four were diamond 1.6 mm thick. Each target was approx .006 of a proton interaction length. There was a gap of 1.5 cm between targets. The thinness of the disks provides a strong constraint on the z-position of the primary vertex and the air gaps between them provided a volume for reconstructing secondary vertices uncontaminated by secondary interactions. Dense materials were chosen to allow thin targets which would still provide enough material for about 2% of the pions to interact and also provide a good chance for the shorter lived particles to decay in the air gaps. The two different target materials allow a measurement of the dependence of charm cross section on atomic number. Details of the targets are given in Table 2.1.

2.3 The Silicon Microstrip Detectors

It is important to measure the tracks near the target with good resolution in order to be able to separate the primary and secondary vertices. Silicon Microstrip Detectors (SMDs) were used to measure the tracks of charged particles in the target region.

An SMD consists of a wafer of silicon 300 μm thick, ion-implanted on both sides. Boron was implanted on the upper face to form p-type strips over which a layer of

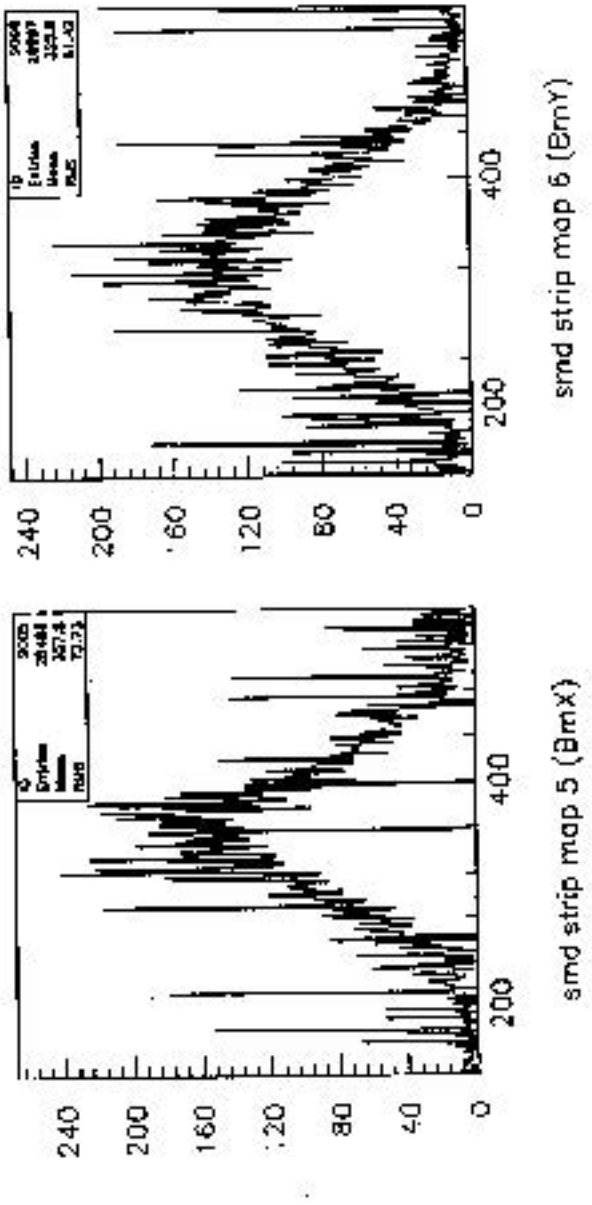

Figure 2.3: Beam Profile (a) x view, (b) y view

Table 2.1: E791 Target

z-position (cm)	material	thickness (cm)	radiation length	interaction length
-8.191	Platinum	0.052	0.169	0.00584
-6.690	carbon	0.157	0.012	0.00589
-5.154	carbon	0.157	0.012	0.00586
-3.594	carbon	0.153	0.012	0.00582
-2.060	carbon	0.158	0.012	0.00582

aluminum served as an ohmic contact. The spacing between the strips inner (pitch) was 25 microns on the planes closest to the target and 50 microns on the other planes. The other face of the silicon wafer was implanted with a continuous layer of arsenic over which was deposited a layer of aluminum. A reverse bias voltage was applied across this p-i-n diode structure which created a region depleted of charge carriers. When a charged particle passes through the detector it liberates about 24,000 electron-hole pairs. This charge can be collected at the nearest strip in 10 nsec. The signals were fanned out to pre-amplifiers and then transmitted to discriminator cards.

Six planes of SMDs upstream of the target together with 8 planes of proportional wire chambers (PWCs) provide beam tracking. Seventeen planes downstream of the target are used to measure the tracks of charged particles produced by interactions in the target. The SMD system had a geometrical acceptance of about ± 125 mrad. Overall the SMDs were about 90% efficient with about 0.1% noise. The parameters of the SMDs are given in Table 2.2.

Figure 2.4(a) shows the z-distribution of primary interaction vertices, clearly showing the foil structure of the target. The peak near z=0 is due to interactions in the

Table 2.2: SMD Parameters

plane	orientation	z-position (cm)	pitch (μm)	width (cm)	efficiency
1	y	-80.250	25	0.96	0.85
2	x	-79.919	25	0.96	0.85
3	w	-74.529	25:50	1.28	0.98
4	w	-33.163	25:50	1.28	0.98
5	x	-30.133	25:50	1.12	0.98
6	y	-29.483	25:50	1.12	0.98
7	y	0.670	25:50	2.48	0.83
8	x	1.000	25:50	2.48	0.85
9	x	1.931	50	2.56	0.93
10	y	3.015	50	2.56	0.95
11	v	6.684	50	2.56	0.96
12	y	11.046	50	3.84	0.98
13	x	11.342	50	3.84	0.97
14	v	14.956	50	3.84	0.94
15	x	19.915	50	5.00	0.90
16	y	20.254	50	5.00	0.88
17	v	23.878	50	5.00	0.98
18	v	27.558	50:200	9.60	0.98
19	x	31.848	50:200	9.60	0.96
20	y	34.548	50:200	9.60	0.98
21	x	37.248	50:200	9.60	0.99
22	v	39.948	50:200	9.60	0.99

Table 2.3: Magnet Parameters

	M1	M2
Z-position (cm)	273.5	617.7
aperture (cm^2)	174×86	171×88
length (cm)	165	208
current (amps)	2500	1800
p_T kick (Gev/c)	0.21	0.32

interaction counter. Figure 2.4(b) shows the z-distribution of secondary vertices. The transverse resolution of each plane came close to the theoretical value of pitch/$\sqrt{12}$.

2.4 Downstream Tracking and Momentum Measurement

The momentum of charged particles is determined by measuring the curvature of the tracks in a magnetic field. Two large-aperture magnets provide the field and the trajectories are measured with drift chambers. The details of the magnets are given in Table 2.3. The main component of the magnetic field was in the vertical direction so particle trajectories were bent in the horizontal direction. The magnetic field was measured by Ziptrack [31, 32] before data taking and fine tuned for each run by reconstructing K_s particles (see Fig. 2.5). Ziptrack is a Fermilab magnet mapping machine which used three small, mutually perpendicular coils with a common center to measure the field.

A drift chamber is a device that uses the drift time of ionization electrons in a gas to measure the spatial position of an ionizing particle. Drift chambers consist of

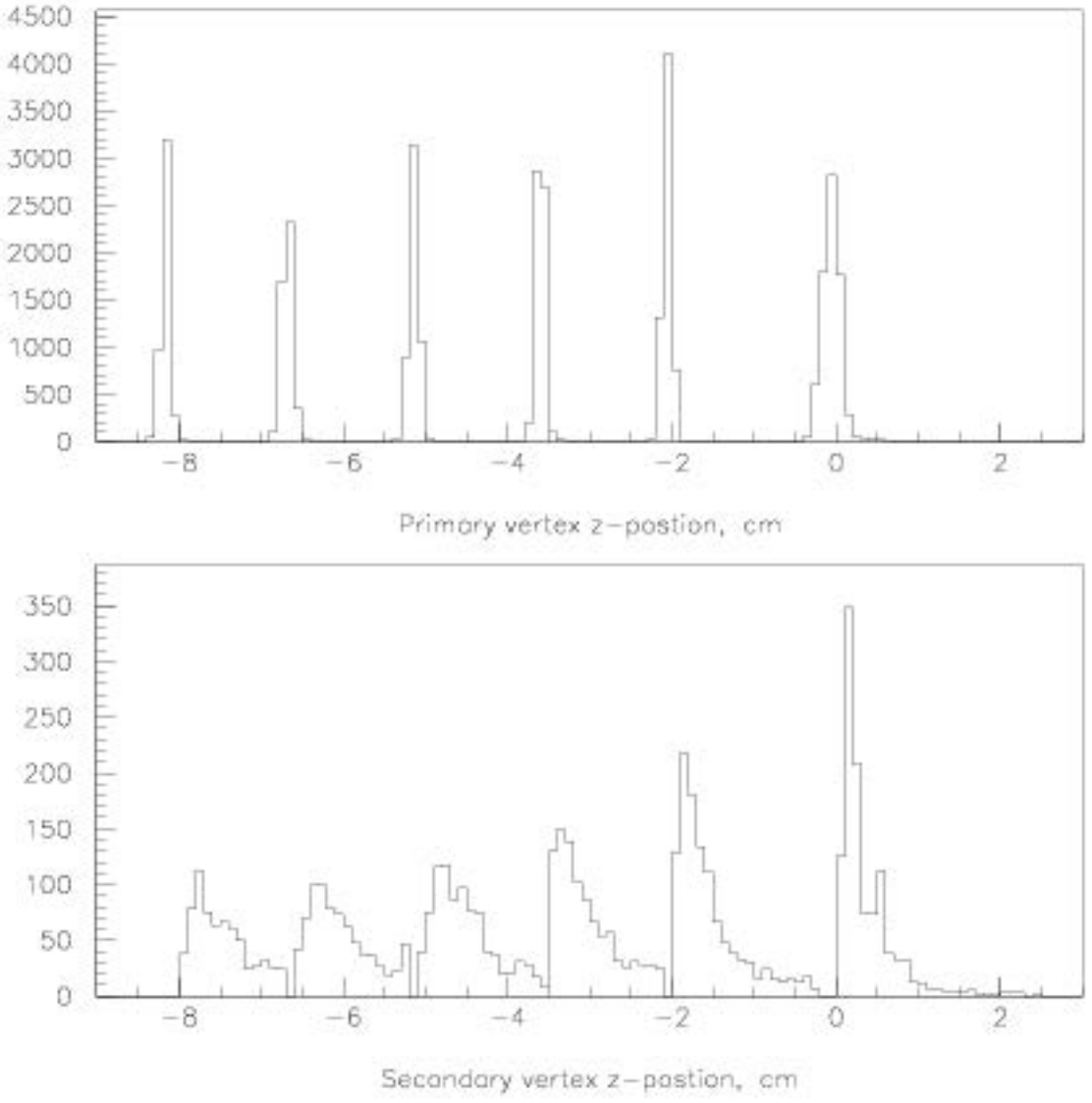

Figure 2.4: (a) Primary Vertex z position (b) Secondary Vertex z position

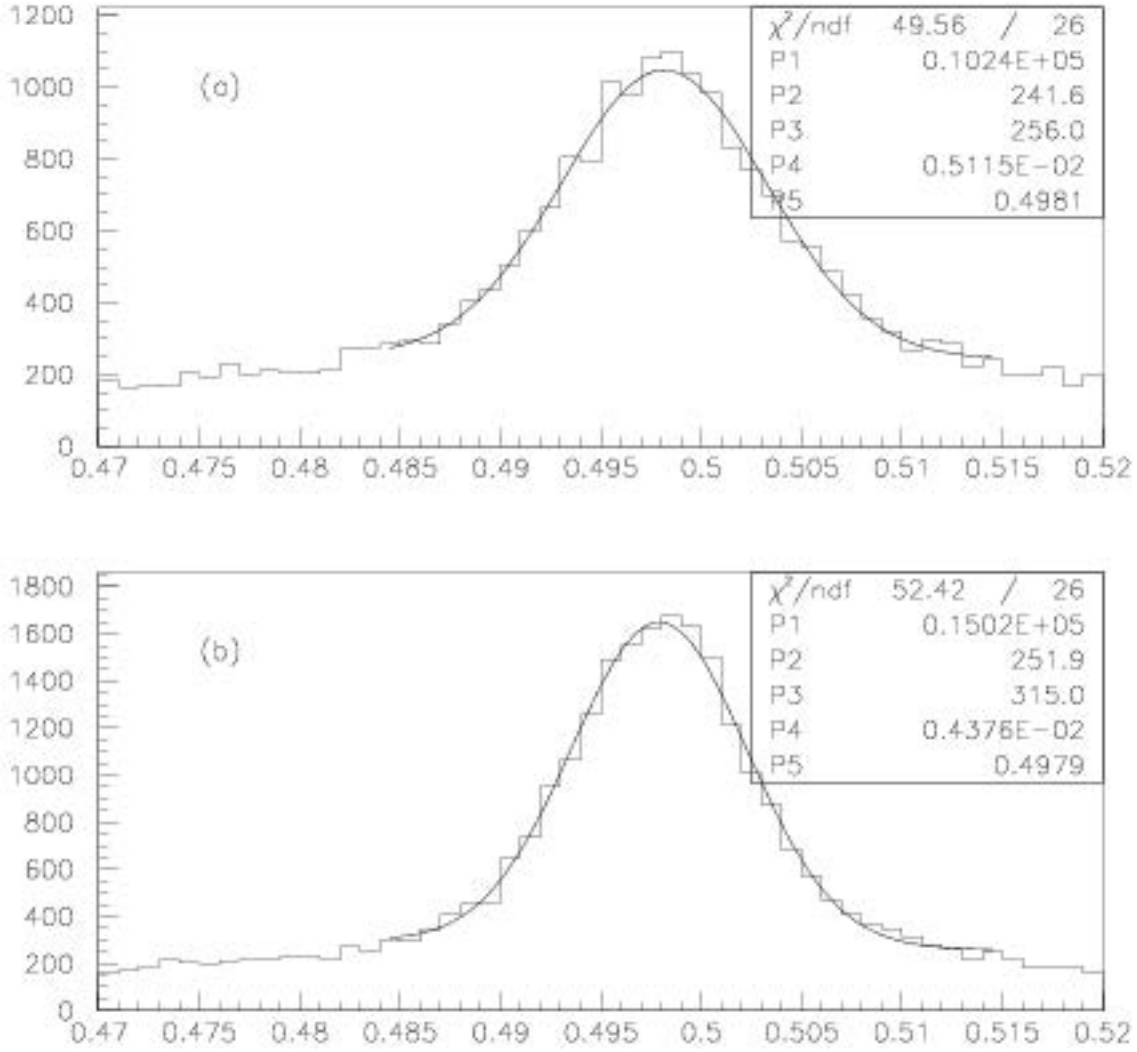

Figure 2.5: K_s Mass Spectrum (a) Track Momentum Measured with One Magnet, (b) Track Momentum Measured with Two Magnets

sense planes, made up of alternating sense wires and field shaping wires, sandwiched between cathode planes to form drift cells around each sense wire. By using sets of closely spaced U, V and X views, the physical location in space of charged particle trajectories could be found. The chambers were filled with a mixture of argon and carbon dioxide. When a charged particle passes through the gas, the gas becomes ionized and the electrons drift toward the sense wire. When the electron gets near the sense wire a charge avalanche occurs. The charge collected is passed to a time-to-digital converter (TDC) via a discriminator.

There were a total of 35 drift chamber planes grouped into 11 assemblies (an assembly is a set of planes used to determine a space point). These assemblies were further grouped into four chambers D1 through D4. All planes were in one of 3 orientations X, U or V as shown in Figure 2.6. D1 also had X′ planes which were offset by half a cell to help resolve ambiguity arising from the fact that one cannot tell which side of the wire a particle passed. Details of the drift chambers are given in Table 2.4. The resolution varied from about 260 μm for D3 to 500 μm for D4. The average efficiency was about 90%. However the central region of the drift chambers had very low efficiency due to the high rate there. This lowered the efficiency for reconstructing high momentum tracks. Two planes of Proportional Wire Chambers (PWCs) which measured the position in the Y-direction were placed just upstream of D1 and between D1A and D1B to improve tracking resolution.

2.5 The Čerenkov Detectors

Charm particles decay predominantly into final states containing a strange particle, either K mesons or hyperons (Λ, Σ), which decay into protons (or neutrons) and pions. Hence being able to identify the kaons and protons among the more abundant pions is very useful. Particle identification was accomplished by two large gas-filled threshold Čerenkov counters C1 and C2. A charged particle moving through a medium of refractive index n at a speed greater than the speed of light in that medium will emit light at an angle $\cos\theta = 1/(\beta n)$. Two particles of the same momentum but different masses will be travelling at different speeds, hence for some particular refractive

Table 2.4: Drift Chamber Parameters

DC assembly	cell size (cm) U/V	X	active area x×y (cm^2)	z-position (cm)
D1-A	0.446	0.476	86 × 65	144
D1-A	0.446	0.476	114 × 65	182
D2-1	0.892	0.953	182 × 130	384
D2-2	0.892	0.953	182 × 130	426
D2-3	0.892	0.953	210 × 130	468
D2-4	0.892	0.953	228 × 130	499
D3-1	1.487	1.588	254 × 130	930
D3-2	1.487	1.588	254 × 130	972
D3-3	1.487	1.588	254 × 130	1014
D3-4	1.487	1.588	302 × 130	1045
D4	2.97	3.18	508 × 240	1744

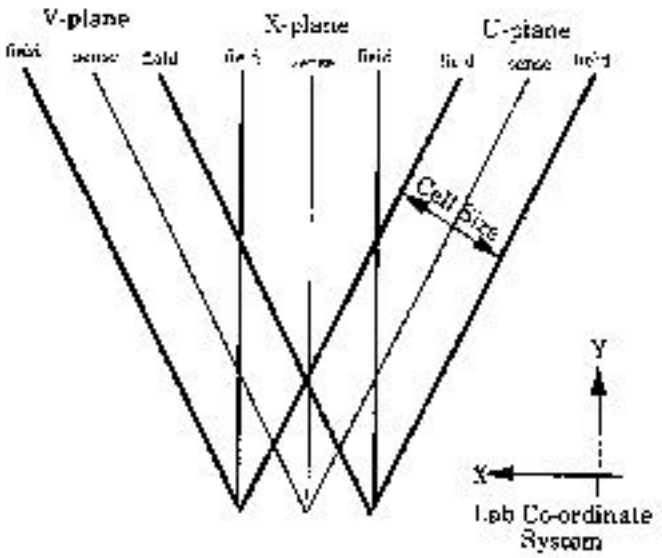

Figure 2.6: Orientation of Drift Chamber Planes [30]

index, one will emit Čerenkov light whereas the other will not. The two detectors had different gas mixtures to provide maximum discrimination between different mass particles (π, K, P) at typical momenta for this experiment (see Fig. 2.7).

These counters operated at atmospheric pressure with a segmented mirror arrangement. The Čerenkov light was reflected by mirrors into Winston cones which passed the light to photomultplier tubes (PMTs). The face of each PMT was coated with a layer of waveshifter to shift the wavelength of the incident light (160 nm - 250 nm) to a wavelength in the region where the PMTs were sensitive (350 nm - 500 nm).

2.6 The Calorimeters

A calorimeter is a device which measures the total energy deposited by a particle or group of particles. The TPL calorimeters are sampling calorimeters which periodically sample the development of a shower initiated by an incident particle. There are two types of sampling calorimeter, distinguished by whether the incident particle initiates an electromagnetic or hadronic shower.

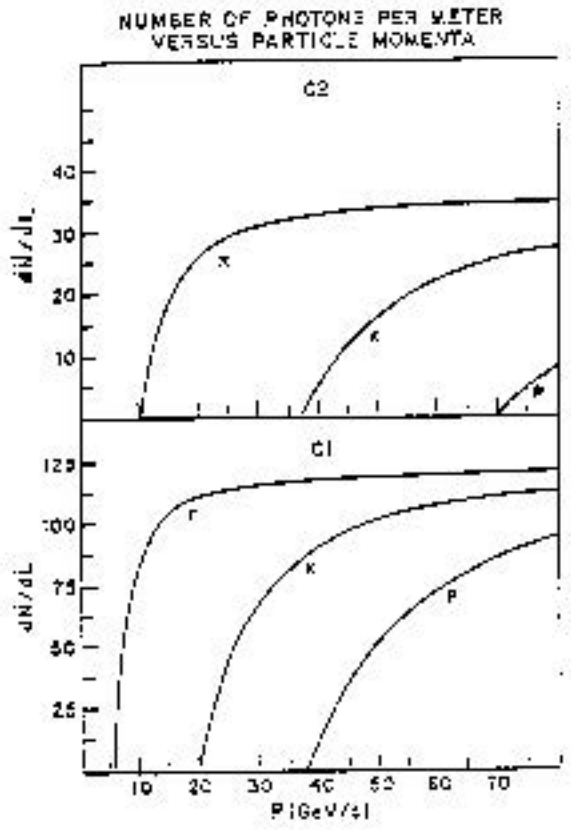

Figure 2.7: Threshold Curves for the E791 Čerenkov Counters

Table 2.5: Čerenkov Counter Parameters

	C1	C2
gas mixture	100% N_2	80% He, 20% N_2
refractive index	1.000290	1.000086
length (m)	3.7	6.6
number of cells	28	32
pion threshold (Gev/c)	6	11
kaon threshold (Gev/c)	20	36
proton threshold (Gev/c)	38	69

Electrons and positrons with energies above 100 MeV lose energy almost entirely through bremsstrahlung. The emitted photons typically carry off a large fraction of the electron's energy. For photons with energy greater than 100 MeV the major interaction is pair production. In this manner a single initial electron, positron or photon can develop into an electromagnetic shower. The measurable signal can be considered as the sum of the signals from the track segments of the positrons and electrons.

The physical processes that cause the development of a hadron shower are considerably different from the processes in electromagnetic showers. When an incident hadron interacts, about half the incident energy is passed on to additional fast secondary particles. The remainder is consumed in multiparticle production of slow pions. This results in a shower with a highly collimated core surrounded by lower energy particles which extend a considerable distance away from the shower axis. Fluctuations in hadron shower development producing a range of different particles with vastly different detection characteristics mean that a hadron calorimeter will have a much poorer energy resolution than that of an electromagnetic calorimeter.

The SLIC (Segmented Liquid Ionization Calorimeter) is an electromagnetic calorimeter used for identifying electrons and photons. The hadron calorimeter at TPL is known as the Hadrometer. The energy deposited in the calorimeters was used to form the transverse energy (ET) trigger (see page 33). The calorimeters are the only detectors in the TPL spectrometer which detect neutral particles.

2.6.1 The SLIC

The SLIC is composed of 60 layers of lead and liquid scintillator[1], each layer corresponding to 1/3 of a radiation length. The liquid scintillator layers are divided into strips 3.17 cm wide by means of teflon coated sheets of aluminum which have square wave corrugations. The first layer, the "U" view, has corrugations at an angle of +20.5 deg to the vertical, the next layer, the "V" view, has corrugations that are at −20.5 deg to the vertical, and the next layer, the "Y" view, has corrugations that are

[1] NE235A

horizontal. The following layers repeat the U, V, Y sequence. Between the layers of liquid scintillator are lead radiators which are actually AL-Pb-Al laminate. Each of the corrugation channels forms a light pipe. The light generated in the scintillator layers propagates along the teflon channels by total internal reflection. At one end light is reflected by a mirror with a reflectivity of about 80%. The light reaching the other end exits the SLIC through a lucite window. This light is collected by a waveshifter bar which picks up light from all 20 layers in depth of a given view. A photomultipier tube glued to the end of each wavebar converts the light to current pulses. Under ideal conditions at least 10% of the light incident upon the wavebar should be transmitted along the wavebar to the PMT. However it was discovered before the run that several wavebars on the bottom face of the SLIC had been contaminated by oil leaks and had very low light yield at the PMT. These wavebars were replaced and the oil leaks were patched before data taking began. Each readout, plus the associated liquid scintillation region is called a counter. There are 109 counters in each of the U and V views, and 116 counters in the Y view. Each PMT had two outputs: the anode output went to an analog-to-digital converter (ADC) for digitization and the output from the last dynode went to a weighted sum module for the ET trigger. Typically 60% of an electromagnetic shower was contained within a single counter of width 3.17 cm, so the energy deposited in neighboring counters could be used to find the shower position with a resolution of about 0.5 cm. A nitrogen laser-driven light pulser system was used to feed light via fiber optic cables to all phototubes of the SLIC and HADROMETER. This system was used for setting up the system and testing all components from the phototubes through to the ADCs.

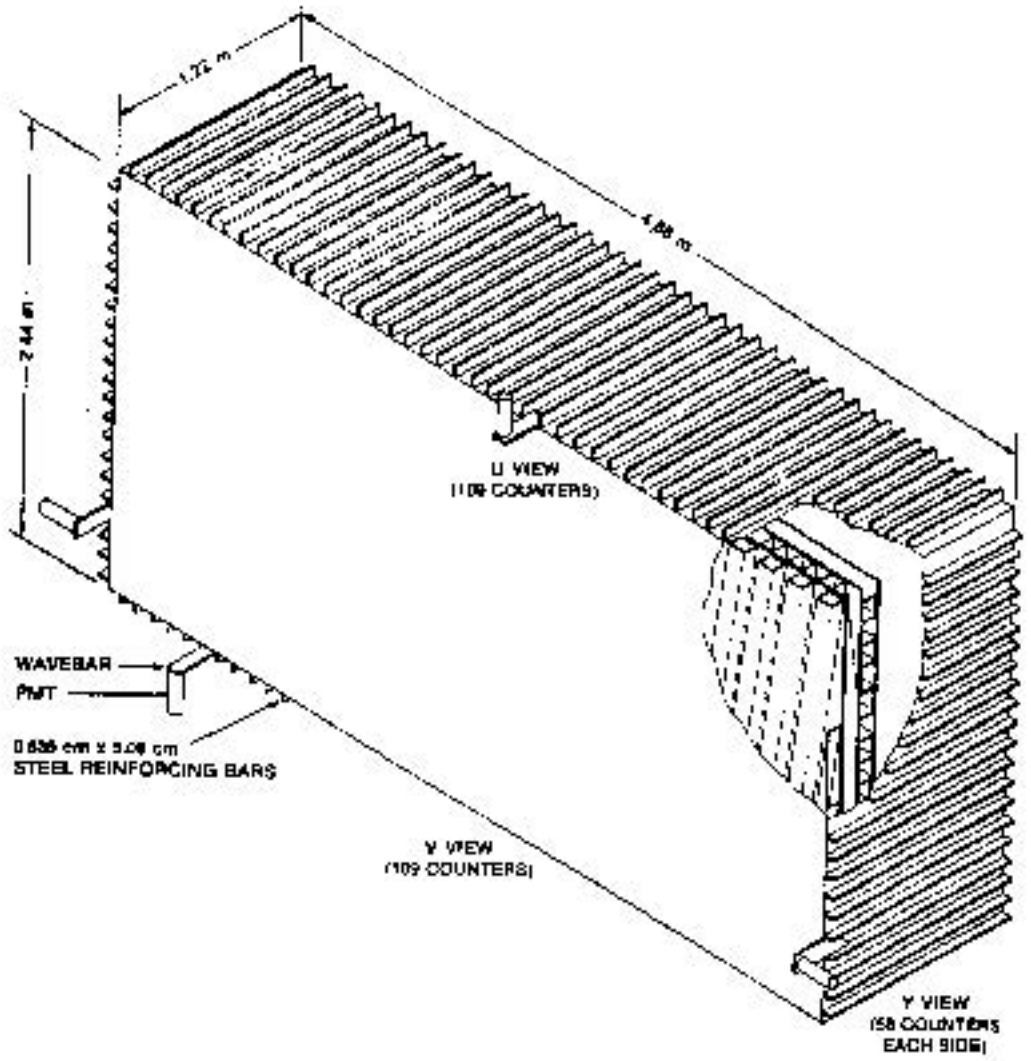

Figure 2.8: SLIC

2.6.2 The Hadrometer

The Hadrometer consisted of 36 alternating layers of 1-inch thick steel plate and 3/8-inch thick, 5.7-inch wide scintillator strips. The scintillator layers alternated with 33 vertical "X" strips and 19 horizontal "Y" strips. The Y strips were further divided at the center. The Hadrometer was divided into front and back modules. The first 9 upstream layers of each view were were joined by lucite light pipes which fed the scintillator light into PMTs. Similarly the 9 downstream layers of each view were joined by light pipes. Like the SLIC each PMT had two outputs: the anode signal went to an ADC, and the dynode signal to the ET trigger. The hadrometer provided the only source of information on neutral hadrons. However because of the poor energy resolution ($dE/E = 0.75/\sqrt{(E)}$) the main use of the Hadrometer was in the trigger.

2.7 Muon Wall

Just downstream of the Hadrometer is a steel wall 40 inches thick. Almost all particles except muons and neutrinos were absorbed by this steel. Downstream of the steel wall are two layers of scintillation counters for muon identification: a set of vertical strips known as the X Muon Wall and a set of horizontal strips known as the Y Muon Wall. The geometry is shown in Figure 2.7. The scintillator light was fed into PMTs, the output of which fed into discrimators which set a latch bit if there was a signal above the threshold of the discriminator. The signal was also fed into a TDC so the time of arrival of the signal could be used to determine the position of the particle along the length of the scintillator. There is also a set of muon counters at the upstream end of the spectrometer, known as the Front Muon Wall. This was only used as part of a muon trigger for calorimeter calibration runs, and to veto halo muons in real events.

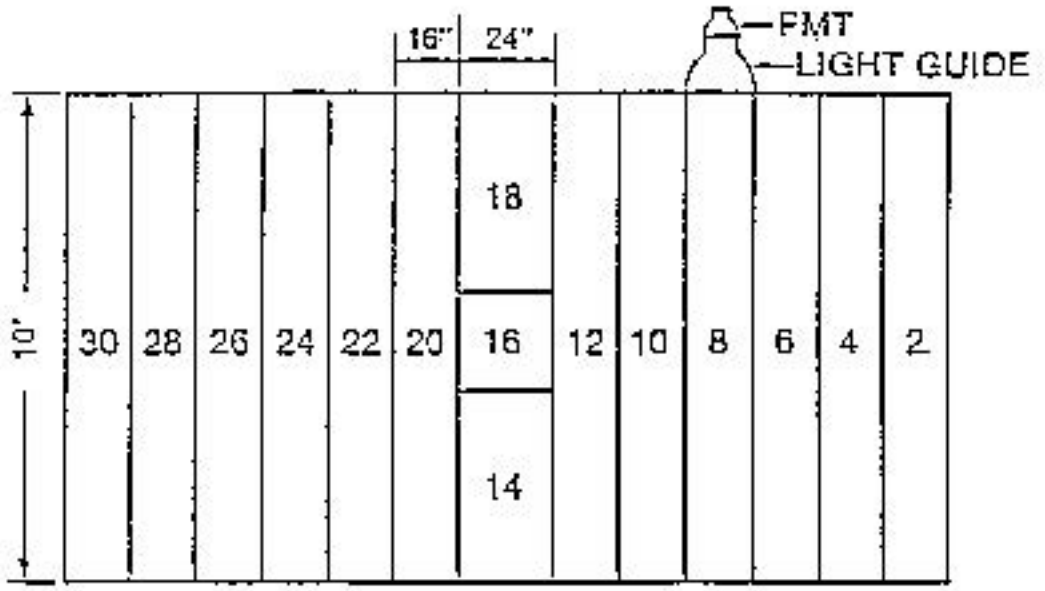

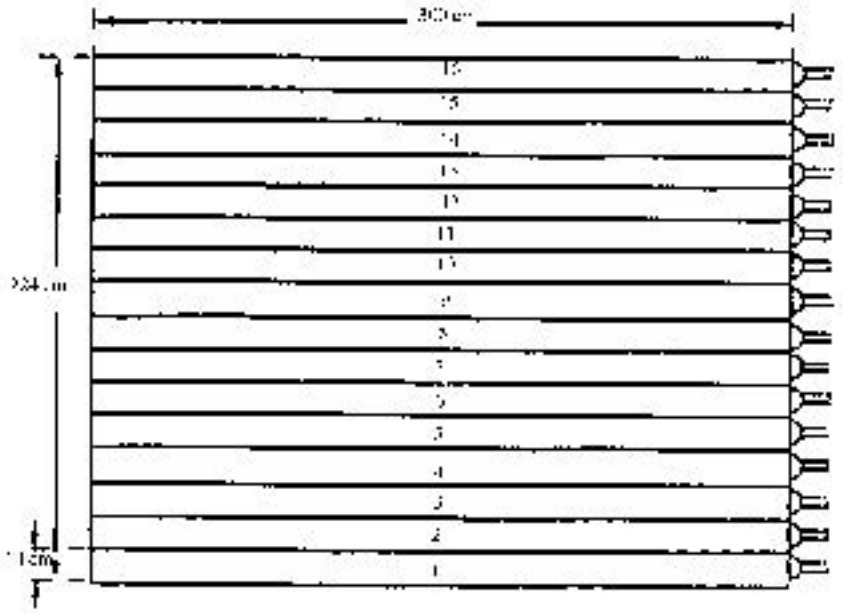

Figure 2.9: Muon Wall (a) X counters, (b) Y counters

Chapter 3

TRIGGER AND DATA ACQUISITION

3.1 Trigger

About one interaction in a thousand results in the production of charm quarks. These events are difficult to recognize in real time. The strategy of E791 was to use a very open trigger, writing as many events to tape as possible online and then selecting charm events offline. The main elements in the trigger were three scintillator paddles (the beam spot counter, the halo counter and the interaction counter) and the calorimeters. A beam particle passing through the target was signaled by a coincidence between the beam spot and interaction counters. Events with more than one beam particle were rejected by vetoing events where either the signal in the beam spot counter counter was too high, or where there was a signal in the halo counter or where the total energy in the calorimeters was too high. About 2% of incident particles interacted in the target. The interaction was detected by a signal in the interaction counter more than 4.5 times that expected from the passage of a minimum ionizing particle.

Charm events have on average a higher transverse energy (ET) than events containing only lighter quarks. The ET of an event was measured by summing the energy in the calorimeters, with the signal from each channel being weighted by the distance

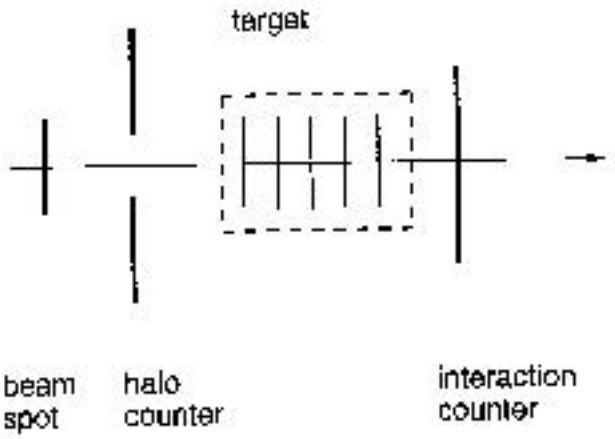

Figure 3.1: Trigger Configuration

from the center of the detector. Most events were triggered with this ET trigger which required a single beam particle, an interaction, and an ET above a certain threshold. Smaller numbers of beam triggers and interaction triggers were taken for monitoring purposes.

The threshold for the ET trigger was set so that the data rate saturated the Data Acquisition system. This resulted in quite a low threshold so that the main effect of the ET trigger was to reject non-interacting beam particles which passed the interaction counter threshold.

3.2 Data Acquistion

The open trigger strategy of E791 required the development of a very fast Data Acquisition system. Twenty-four thousand channels were digitized by ADCs, TDCs, and latches, then read out by 16 parallel controllers. To achieve a 50 μsec dead time most of the front end digitizers that had been used in previous experiments at TPL were replaced by faster systems. Events were recorded at a rate of 9000 per second

during the spill and buffered to eight parallel 80-MByte FIFO memories. Each FIFO was attached to a specific set of front end controllers and contained a particular segment of each event. The FIFOs were read out continuously by a six crate VME system containing a total of 54 CPU cards. Each VME crate was attached to each FIFO to form a 6×8 switching matrix. Six events could thus be built in parallel. The CPUs also compressed events and prepared them for writing to tape. Seven Exabyte 8-mm tape drives were attached to each VME crate. Thus a total of 42 tape drives in parallel continuously recorded data at a rate of 9.6 Mbytes per second. The 42 tapes were changed after every 3 hours of beam time. During the six month run from July 1991 until January 1992 twenty billion physics events were recorded on 24000 8-mm tapes.

Chapter 4

CALIBRATION OF THE CALORIMETERS

The aim of the calibration process was to measure the ratio of ADC counts to energy deposited for each channel of the calorimeters. This ratio is known as a calibration constant. Muons were used for the initial calibration of both the SLIC and Hadrometer. Muons are minimum ionizing particles and will deposit approximately the same amount of energy independent of their momentum. The peak of the single muon peak can be used to obtain a relative channel-to-channel calibration of the phototube gains.

A muon beam was produced by closing the collimators in our beam line. The muons were well dispersed and hit all channels of the calorimeters. The analysis magnets were turned off so the muons travelled parallel to the beamline and therefore the distance travelled through each counter was the same.

We used a coincidence between the Front muon wall and Back Muon wall as a trigger and recorded several million events in each calibration run. We did a muon run approximately once every two weeks during the experiment to monitor the gains of each channel.

4.1 Calibration of the Hadrometer

Muons were identified in the data by looking for a coincidence between front and back sections of the hadrometer in both X and Y channels. Knowing the X and Y position of the muon, we plotted the muon signal as a function of the position of the shower in the scintillator. (A muon depositing energy close to the phototube will give a bigger signal than one further away.) We then fitted an attenuation curve for each channel. This was only done once — we assume that the shape of the attenuation curve does not change over the course of the experiment. (see Fig. 4.1).

For each muon run we identified muons and corrected the signal for attenuation to get the equivalent signal at $x = 0$ (for Y counters) or $y = 0$ (for X counters). For each channel we plotted a histogram of the muon signal and extracted the peak position. On average this was about 6 ADC counts. (See Fig. 4.2) From previous experiments using this calorimeter it was known that a muon gives the same signal as would be seen when a pion of energy 2.4 GeV passes through the Hadrometer.

The absolute calibration was checked using pions from normal data. The high multiplicity of tracks in E791 compared to previous experiments and the poor resolution of the Hadrometer made it difficult to measure the absolute calibration using pions.

4.2 Calibration of the SLIC

The SLIC was also calibrated with muons in a similar fashion to the Hadrometer. Muons were identified by looking for a 3-fold coincidence in the U, V, and Y views. Attenuation curves were fitted, the muon signal was histogrammed and the peak was extracted for each channel. The muon peak for SLIC channels was also about 6 ADC counts.

Electrons were used for the absolute calibration of the SLIC. An electron beam was produced by putting a lead convertor downstream of the primary target, and tuning the beamline for 20 GeV/c. An extra piece of aluminum was placed near the secondary target to increase the number of electrons radiating a bremstrahlung photon which

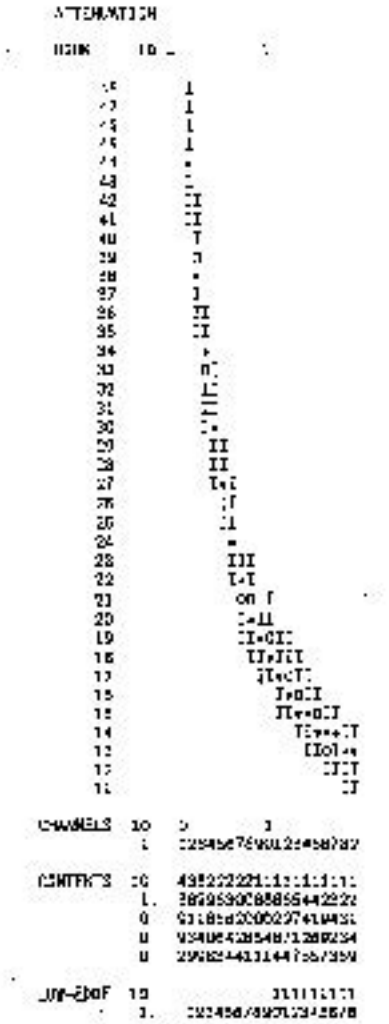

Figure 4.1: Attenuation curve for a Hadrometer channel

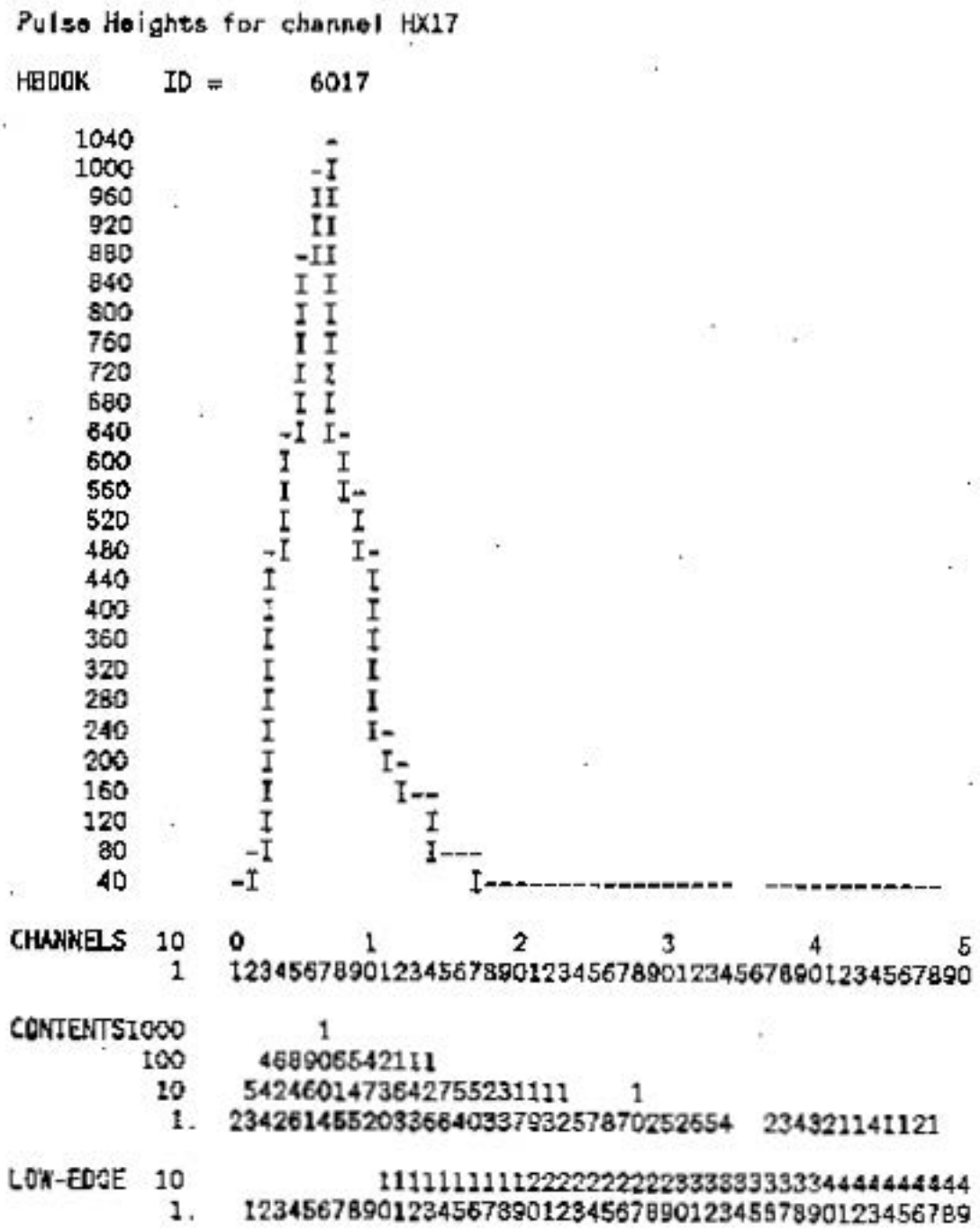

Figure 4.2: Muon pulse heights for Hadrometer channel HX17

could then convert to an e^+e^- pair, thus increasing the spread of momentum in the beam and allowing both east and west sides of the SLIC to be calibrated. The analysis magnets were turned on to allow the momentum of the track to be determined, and to spread the electrons over as many channels of the SLIC as possible.

The electrons were only in the central plane and so could not be used to calibrate the Y channels. About 50% of the U and V channels were calibrated using the electrons. For electron runs, the momentum p of each track was found from the drift chamber data. The gains on each channel were adjusted by an iterative procedure until we got $E/p = 1.00$, where the energy E was determined from the energy deposited by the electron. By comparing the muon and electron calibrations for those channels calibrated by both methods we obtained a muon equivalent energy and used this to correct the gains on those channels calibrated with muons only. The muon equivalent energy was found to vary from 340 Mev to 424 Mev depending on the geometry of the channels. In the center of the SLIC a wavebar collected the light from a single corrugation. For outer channels a double-width wavebar collected the light from two corrugations. Due to space restrictions some channels on the east side had only a single-width wavebar to collect the light from two corrugations and hence only collected half the light. For this reason these channels had considerably poorer resolution.

The Y channels were calibrated by finding isolated electromagnetic showers in normal data and requiring that the energy in the Y view be equal to that in the U and V views, using only U and V channels that were calibrated with electrons. The muon equivalent energy for the different types of channels is given in Table 4.1.

Ten muon runs were done during the course of the experiment. For each channel the gain was plotted as a function of time and fitted to a straight line. The fitted values were used to create 10 calibration files. When reconstructing data, the calibration file with the latest run number earlier than the run being reconstructed was used to convert ADC counts to energy in GeV.

The width of the E/p plot provided a measure of the energy resolution. We plotted E/p for different momenta and then plotted $(\sigma_{E/p})^2$ vs. $1/p$ (see Fig. 4.3). The fitted

Table 4.1: Muon Equivalent Energy (MeV) for SLIC

geometry type	U and V channels	Y channels
single width channels	352	424
double width channels		
full readout	371	400
half readout	341	–

energy resolution was

$$(\sigma_E/E)^2 = (17\%/\sqrt{E})^2 + (11\%)^2$$

4.3 Monitoring of the Calorimeters

During data taking the state of the calorimeters was monitored continuously. A small fraction of events was sent by the data acquisition system to an event pool for monitoring all elements of the spectrometer. Particpation plots for all planes of the calorimeters were made continuously so that any dead channels would be quickly noticed. Dead channels could result from any of several causes including failures of high voltage power supplies, burnt out resistors in phototube bases and failure of ADC modules.

The data from the ADCs was pedestal subtracted and compressed (*ie.* only channels with a signal of at least one count were read out). The pedestals of the ADCs were monitored during the interspill period and the values downloaded to a memory in the ADC module for automatic subtraction.

The high voltage power supplies for the phototubes were monitored continously

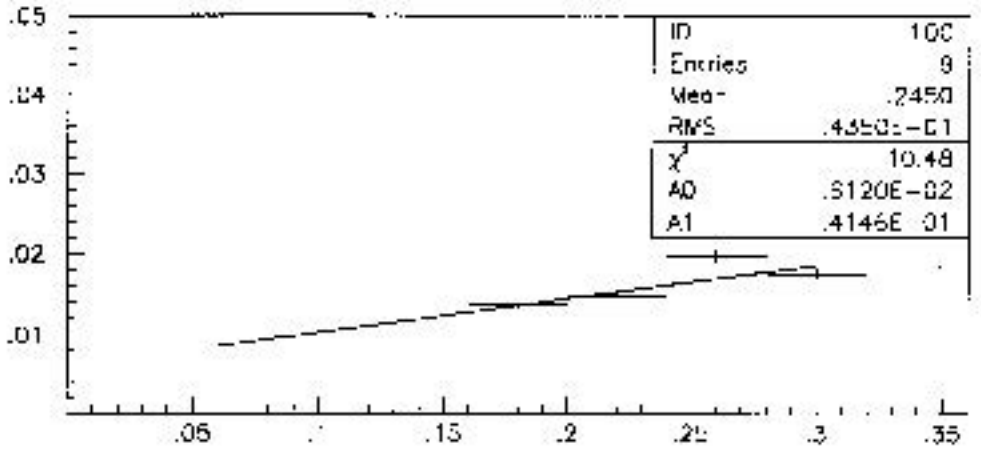

Figure 4.3: $\sigma(E/p)^2$ vs. $1/p$

during the run and error messages were posted to a screen in the control room if one or more channels was outside the acceptable range.

Chapter 5

EVENT RECONSTRUCTION AND SELECTION

The data sample consists of about 20 billion events on 24000 8-mm tapes. Each set of 42 tapes with data recorded over about a three hour period is known as a run. The total data set was divided into approximately 600 runs. It was an enormous task to reduce this to a manageable set of events for physics analysis.

5.1 Event Reconstruction

5.1.1 Track reconstruction

Charged tracks were first reconstructed in the silicon system. First one dimensional tracks were reconstructed in each view. Four hits were required in the X and Y views and three hits in the V view. These tracks were then combined to form three dimensional tracks. The tracks were then projected downstream through the magnets and drift chambers. Tracks originating in the drift chambers were searched for using the hits remaining. The efficiency in the central region of the drift chambers is much lower than in the outer regions due to the high rate there. This reduces the efficiency of reconstructing high momentum tracks.

5.1.2 Vertex reconstruction

The software package called VTXSTR was used to reconstruct vertices. VTXSTR attempts to find a primary vertex among tracks that intercept the beam track. Once a good two prong vertex is found, additional tracks are added if they do not add too much χ^2 to the vertex fit. Secondary vertices are searched for among the tracks not included in the primary vertex, starting with pairs of tracks with small distances of closest approach. The resolution of primary vertices varied from 240 μm to 400 μm depending on target foil. The resolution of the vertices in the most upstream foil was the worst due to multiple scattering of the tracks in the downstream foils. The primary vertex reconstruction efficiency was 96%.

5.2 Event Selection

5.2.1 Pass0 - Alignment, Calibration

Before reconstruction of each run we created alignment and calibration files for each of the elements of the spectrometer.

5.2.2 Filtering

This stage of the data selection was done on large UNIX-based computer farms at four centers: the University of Mississippi, Centro Brasileiro de Pesquisas Fisicas (CBPF), Fermilab and Ohio State University (later moved to Kansas State University). For each event charged tracks were reconstructed in the SMDs and drift chambers, primary and secondary vertices found, and Čerenkov probabilities calculated.

In this first stage an event is kept if it contains one of the following:

- a secondary vertex in the SMD region,
- a secondary vertex in the region downstream of the SMDs that is a candidate for a Λ or K_s,
- a pair of tracks in the SMDs that form a good candidate for a ϕ.

Approximately three quarters are the data was analysed with this filter (Release 5 code). The filter cuts are shown in Table 5.1. The remainder was reconstructed with improved reconstruction code (Release 7) using the full magnetic field instead of a single bend point approximation and slightly modified filter requirements including the addition of a filter for diffractive jets. The SMD secondary vertex filter remained the same. More details of the Release 7 filter can be found in Ref.[39].

If the event passed this filter, the calorimetry and muon identification were done. About 18% of the events were selected by the filter and for these events the raw data plus values of variables calculated during reconstruction were written to data summary tapes (DSTs).

5.2.3 Stripping

This stage of event selection put tighter criteria on certain event types [40]. Particular event topologies were identified and tagged so they could more easily be selected for further analysis. There were two output streams from this stage. The events with candidates for a secondary vertex in the silicon are written to Stream A and events with Λ or K_s candidates were written to Stream B. Stream A selected 25% of filtered events and Stream B selected 18%.

5.2.4 Substripping

The Stream A and B strip tapes are used as input for many different substrips. The Kitchen Sink SubStrip (KSSS) uses the Stream A strip tapes as input and has three different output streams. Output Stream 3 selects D^0 (both 2-prong and 4-prong decays) and D^+ candidates.

Candidates for D^0 and D^+ particles were selected by looping over all possible combinations of two, three or four tracks and then selecting good candidates based on the values of the variables described below. The values of the cuts are shown in Table 5.2.

- CHIS: χ^2 of secondary vertex fit

- SDZ: The significance of separation of two vertices.
  $SDZ = \Delta z/\sigma_z$, where $\Delta z = z_{sec} - z_{pri}$ and $\sigma_z = \sqrt{(\sigma^2{}_{zpri} + \sigma^2{}_{zsec})}$

- DIP: The minimum distance between the primary vertex and line of flight of the charm particle candidate as determined by the location of the secondary vertex and the momenta of the daughter tracks.

- STGT: The number of standard deviations the secondary vertex is outside the nearest target foil. (A negative value of STGT means the secondary vertex is within a target foil.)

- PT2DK: The sum of the transverse momentum squared of all tracks in the charm candidate with respect to the direction defined by the sum of their momenta.

- SDCA: The distance of closest approach of a track to the primary vertex divided by the error in that distance.

- SDCAMIN: The minimum SDCA of all tracks in charm candidate

- PTB: The transverse momentum balance *ie.* the transverse momentum needed to be added to the momentum of the charm candidate to make it point back to the primary vertex from its calculated decay vertex location.

- CKVK: The probability that a track is a kaon based on Čerenkov counter information.

Table 5.1: Filter Cuts (Release 5)

FILTER		CUT	
SMD	2-prong	SDZ	> 6
Vertex	3 or more prong	SDZ	> 4
ESTR V	K_s	track χ^2/DOF	< 5
		track momentum	0.5 – 500 GeV/c
		DCA	< 0.5 cm
		z-position of decay	> 10.0 cm
		mass window	0.470 – 0.520 GeV/c^2
ESTR V	Λ^0	track χ^2/DOF	< 5
		track momentum	0.5 – 500 GeV/c
		DCA	< 0.7 cm
		z-position of decay	> 10.0 cm
		p_{max}/p_{min}	> 2.67
		mass window	1.101 – 1.127 GeV/c^2
Φ		track χ^2/DOF	< 5
		track momentum	2 - 400 GeV
		mass window	1.0094 – 1.0294 GeV/c^2
		DCA	0.005
		K prob (each track)	≥ 0.12
		K prob (product)	≥ 0.05

Table 5.2: Kitchen Sink Substrip – Stream 3 Cuts

CUT	2-prong	3-prong	4-prong w/o D^*	4-prong with D^*
mass range (GeV/c^2)	1.75 - 2.0	1.72 - 2.0	1.7-2.0	1.7-2.0
total charge	0	+1 or -1	0	0
CHIS <	15	25	15	15
SDZ >	6.0	8.0	6.0	4.0
DIP (cm) <	.008	.007	.006	.007
PTB (GeV/c) <	0.8	0.7	0.8	0.8
SDCAMIN >	1.0	1.0	4.0	–
PT2DK (GeV^2) >	0.2	–	–	–

Chapter 6

SEARCH FOR D^{**}

This chapter describes a search for D_s^{**} mesons. The possible final states from the decay of the various D_s^{**} states are $D^{*+}K_s$, D^+K_s, $D^{*0}K^+$ and D^0K^+. I will describe here a search for the $D^{*+}K_s$, D^+K_s and D^0K^+ decay modes. (The D^{*0} mode will not be searched for because our π^0 detection efficiency is low.)

6.1 The Monte Carlo

The E791 Monte Carlo program models the interaction of the beam with the target and the subsequent interactions of the secondary particles with the TPL spectrometer. The foundation of the Monte Carlo is the the program PYTHIA[36] which models the QCD processes in hadron-hadron collisions that create charm quark pairs, and the fragmentation processes by which the charm quarks and the remnants of the beam and target particles are transformed into the final state hadrons. The decay of these hadrons is simulated using the known lifetimes. The final state particles are propagated through the spectrometer and the response of the detector is simulated taking account of processes such as multiple scattering, secondary interactions, photon conversions and bremsstrahlung. The digitization part of the Monte Carlo simulates the output of the detector taking account of efficiencies, noise and resolution. The output of the Monte Carlo is in the same format as the raw data.

Using this program I created a set of Monte Carlo events for each of the decay

modes of the D_s^{**} that I was searching for. These events were then put through the same reconstruction and analysis code that was used for the real data.

6.2 Event Selection

The starting point for my sample is stream 3 from the Kitchen Sink Substrip described in the previous chapter. These tapes were re-reconstructed with Release 7 code without rejecting any events so K_s candidates were available on the DST. Tracks are labelled SESTR if they were reconstructed from hits in both the SMDs and drift chambers and labelled ESTR if they were reconstructed from only drift chamber hits. The K_s candidates were searched for from either pairs of SESTR tracks or pairs of ESTR tracks. The combinatoric background was too high relative to the number of signal events to use one SESTR and one ESTR track. The cuts used are listed in table 6.1. Region 1 K_s candidates are those with a decay vertex upstream of the front face of the first magnet and Region 2 K_s candidates are those that decay downstream of this. The mass plots and momentum distributions of K_s, D^0, D^*, and D^+ candidates from the Kitchen Sink Substrip are shown in Figures 6.1 - 6.4.

6.3 Analysis Cuts

I further substrip these tapes to get three sets of tapes:

- Set 1 contains events with a K_s candidate and a D^0 candidate (KPI from KSSS).
- Set 2 contains events with a K_s candidate and a D^+ candidate (K2PI from KSSS)
- Set 3 contains events with a D^0 candidate (KPI from KSSS) and another track which is a charged kaon candidate (Čerenkov probability > 0.13).

These tapes were copied, removing duplicate events in each set. (Duplicate events arose because occasionally an incorrect tape was loaded at the filter stage where the tape number was not written internally and therefore could not be checked when

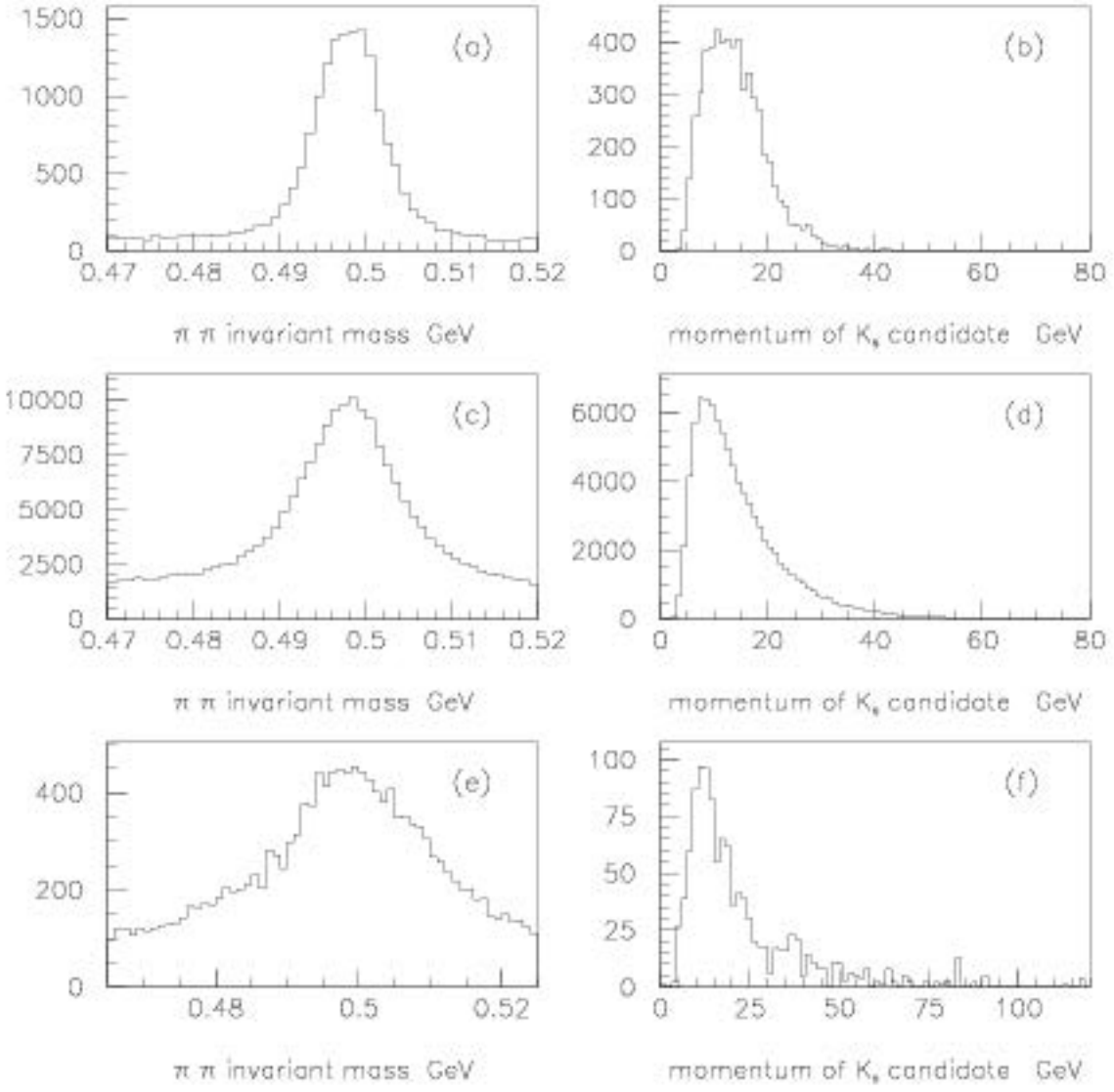

Figure 6.1: (a) K_s mass (SESTR), (b) K_s momentum (SESTR), (c) K_s mass (ESTR-reg1), (d) K_s momentum (ESTR-reg1), (e) K_s mass (ESTR-reg2), (f) K_s momentum (ESTR-reg2)

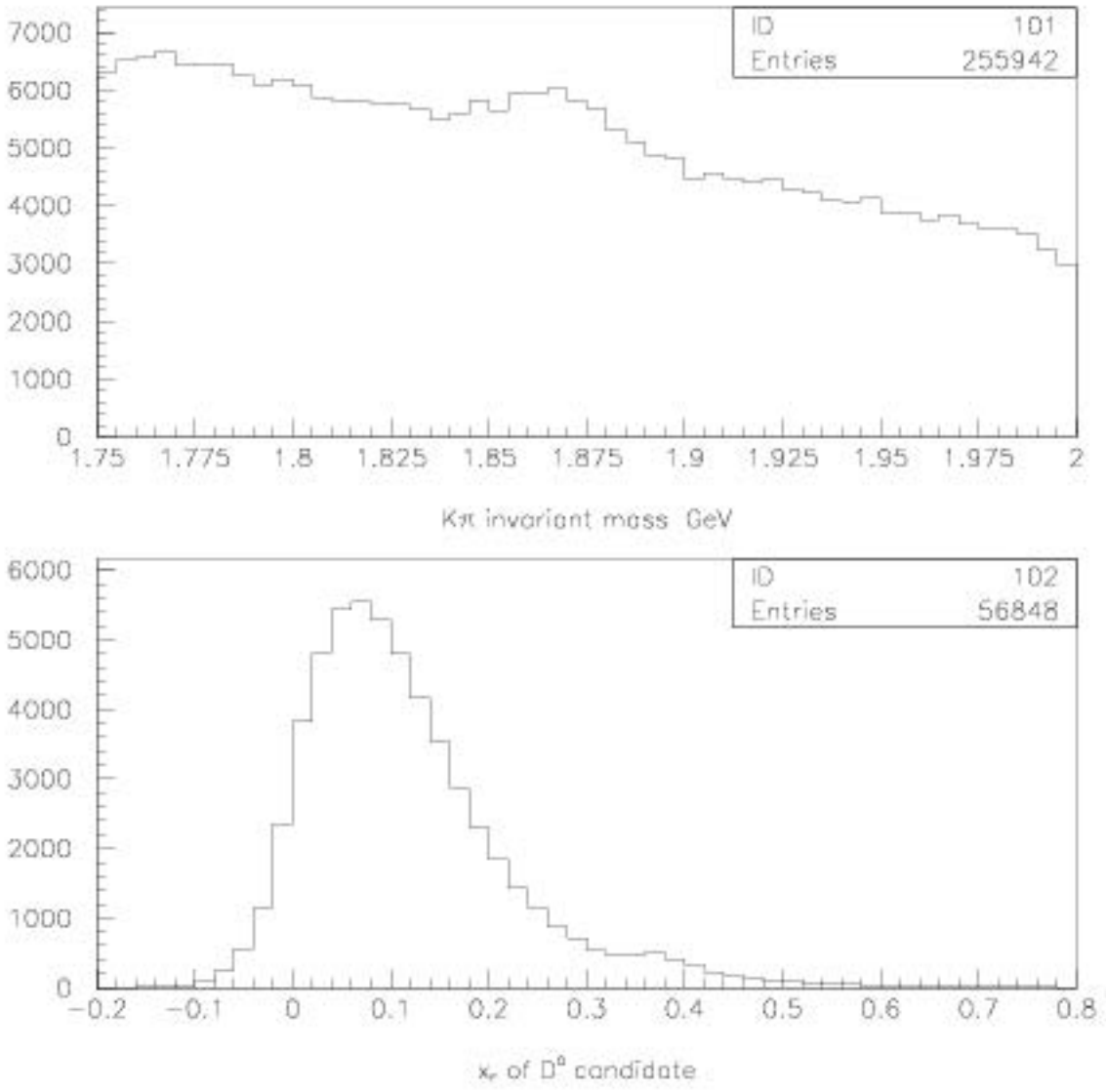

Figure 6.2: (a) D^0 candidate mass , (b) D^0 x_F distribution, at KSSS level of cuts

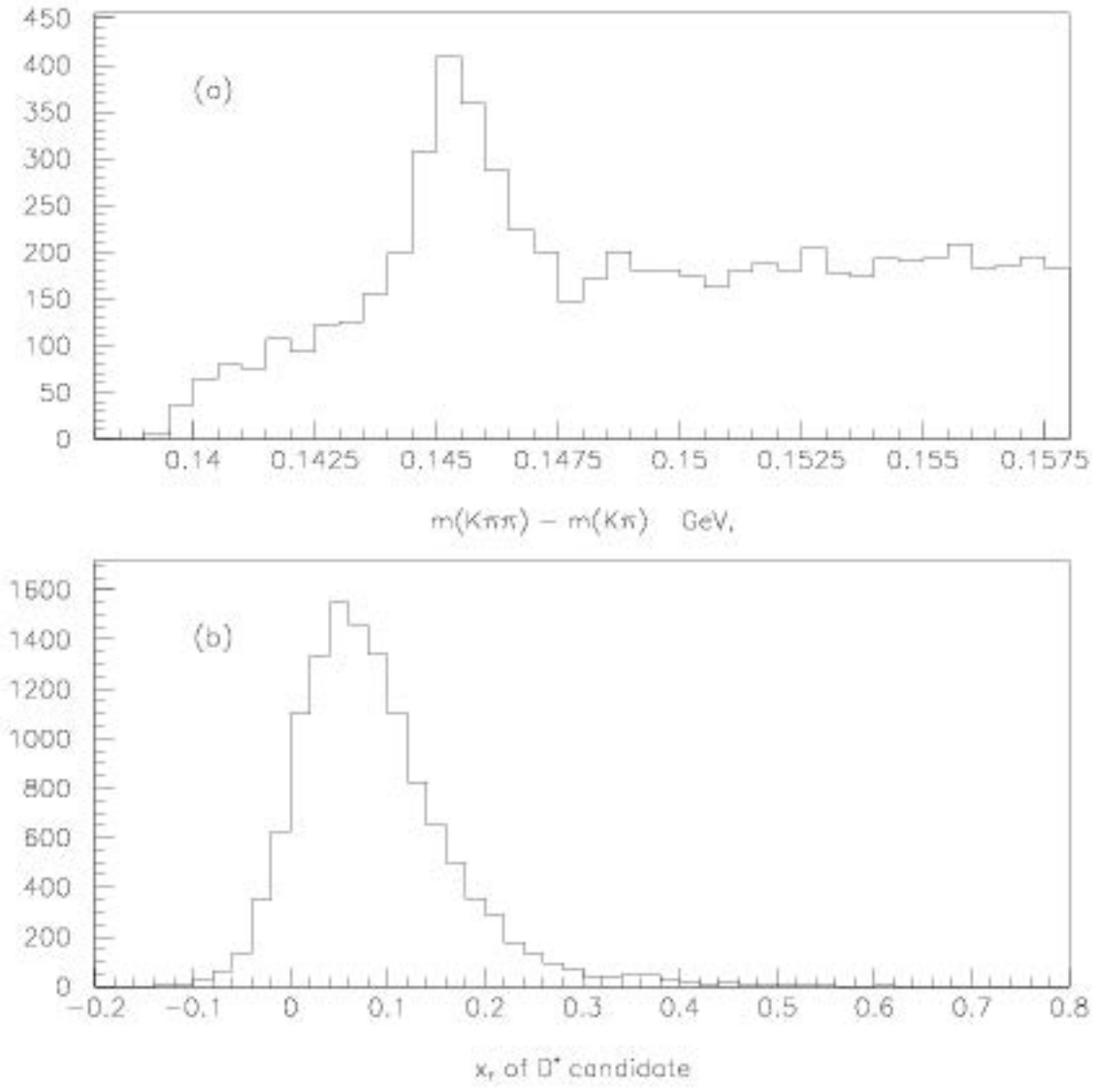

Figure 6.3: (a) D^* candidate mass , (b) D^* x_F distribution, at KSSS level of cuts

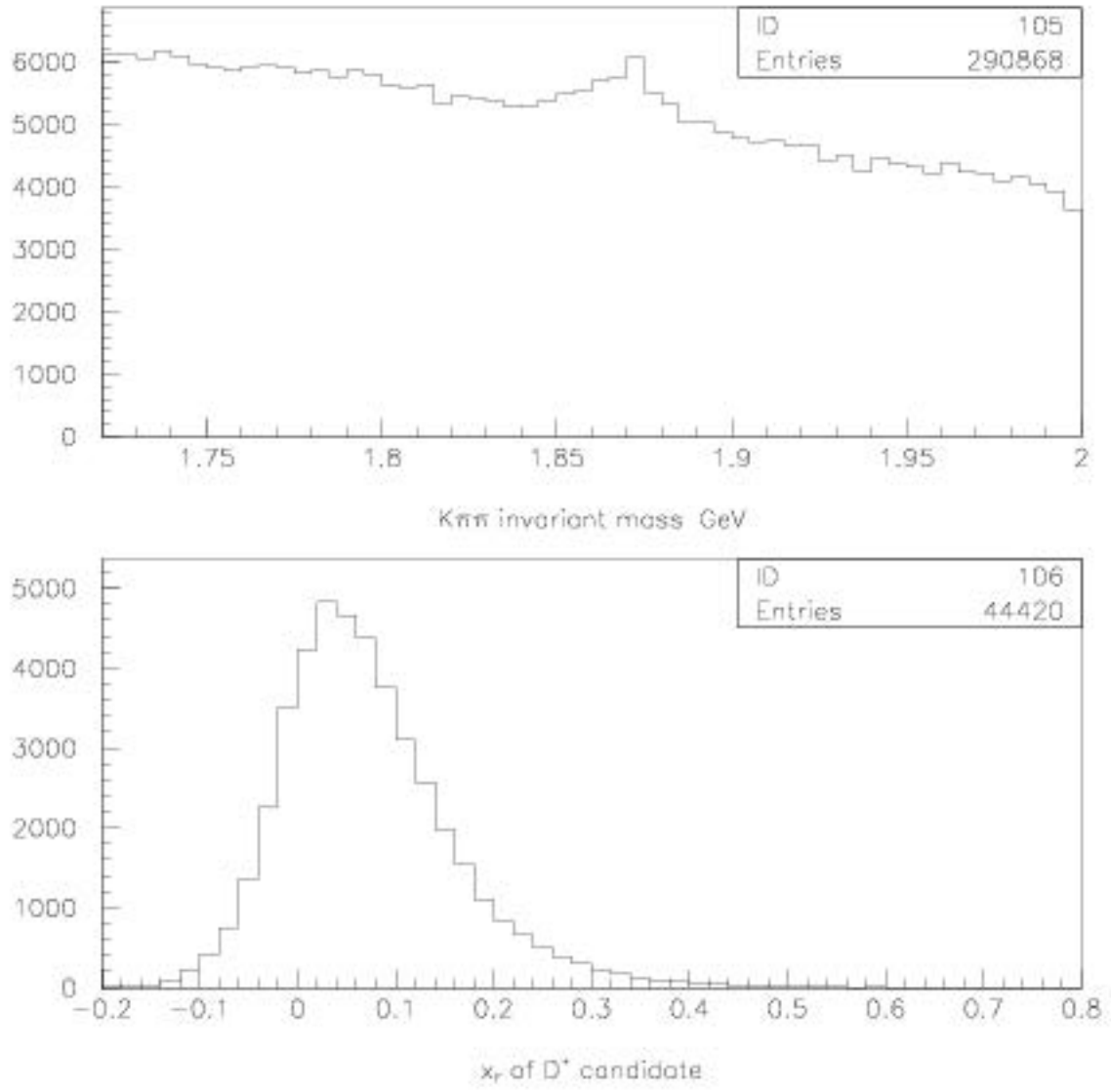

Figure 6.4: (a) D^+ candidate mass , (b) D^+ x_F distribution at KSSS level of cuts

Table 6.1: K_s Selection Cuts

CUT	SESTR-SESTR	REGION 1 ESTR-ESTR	REGION 2 ESTR-ESTR
mass range(GeV/c^2)	0.47 - 0.52	0.47 - 0.52	0.465 - 0.525
total charge	0	0	0
DCA (cm) <	-	1.2	0.7
SDZ >	15	-	-
DIP (cm) <	0.015	0.4 ($8 < z < 10$) 0.7 ($10 < z < 20$) 1.0 ($z > 20$)	1.0

reading the tape. Approximately 1% of events were rejected because they were duplicates.)

Before searching for D^{**} signals I needed to decide on the best way to optimize any D^{**} signal in an unbiassed way. I found that there was very little charm signal above background in events where the primary vertex was in the interaction counter so I rejected these events for all modes. After rejecting the events in the interaction counter I found that the D^* signal was reasonably clean so I made no further cuts at this stage except that for each pair of tracks making a D^0 candidate I allowed on one entry by choosing the track with the greatest Čerenkov probability to be the kaon.

For the other modes the D^+ and D^0 need to be optimized. The number of D^{**} events reconstructed will be proportional to the number of events in the D peak, and the background under the D^{**} will be proportional to the number of signal plus background of the D. Hence if we optimize $S/\sqrt{S+B}$ for the D^+ and D^0 we will have optimized $S/\sqrt{B}$ for the D^{**}. For each of the cut variables listed in Table 5.2 I plotted efficiency vs. cut and $S/\sqrt{(S+B)}$ vs. cut, tightening the cuts by an iterative

procedure until I had maximized $S/\sqrt{S+B}$. All cuts up to this point are shown in Table 6.2.

Figures 6.5 through 6.7 show the mass peaks with the tighter cuts as described above.

The SESTR K_s signal is very clean as can be seen from figure 6.1. The signal to background ratio for the ESTR K_s signal can be improved by cutting on the minimum distance between the projection of the reconstructed K_s track and the primary vertex (KSDIP). Figure 6.8 shows the K_s signal before and after a cut on KSDIP < 0.5 cm. It can be seen that this cut retains 90% of the signal while improving the signal to background ratio from 2.3 to 3.6, however the significance of the signal ($S/\sqrt{(S+B)}$) is reduced from 176.5 to 174.8. The Monte Carlo D^{**} signal becomes narrower as this cut is tightened (see Fig. 6.9). The D^+K_s and D^*K_s signals will be plotted both with and without this cut.

The cuts on the bachelor kaon from the decay $D_s^{**} \rightarrow D^0K^+$ were selected by optimizing $S/\sqrt{B}$ where the signal S was from Monte Carlo events and the background B was from data. The resulting cuts are: the K^+ must come from the primary vertex (in the vertex list) and must have a Čerenkov probability greater than 0.5. Because the Čerenkov probability is not modelled perfectly in the Monte Carlo I start with a looser cut on the Čerenkov probability at 0.13 and plot the D^0K^+ spectrum both with a loose cut and a tight cut on the Čerenkov probability. (I also require that the K^+ track be detected downstream of the first Čerenkov counter in order that Čerenkov identification be meaningful.

The D^{*+} - K_s and D^+ - K_s mass spectra are plotted using the cuts on the D^{*+} and D^+ as described above and $\pm 2\sigma$ mass windows for K_S, D^+, D^0 and $D^* - D^0$. The DK invariant masses are calculated using the momenta of the D^{*+}, D^+ and K_s as measured but fixing the masses to their nominal values from the Particle Data Group [19]. Using Monte Carlo data I found that this method gave a peak with a gaussian width of 1.6 MeV/c^2 compared to the method used by E687 which uses the mass difference between the D^{**} candidate and the D^* which gave a width of 5.0 MeV/c^2 (see Fig. 6.10).

Table 6.2: Analysis Cuts

CUT	2-prong w/o D^*	2-prong with D^*	3-prong
mass range(GeV/c^2)	1.75 - 2.0	1.75 - 2.0	1.72 - 2.0
total charge	0	0	+1 or -1
CHIS >	15	15	25
SDZ >	8.0	6.0	12.0
DIP (cm) <	0.004	0.007	0.005
PTB (GeV/c)<	0.4	0.7	0.35
STGT >	0.0	0.0	1.0
SDCAMIN >	5.0	1.0	4.0
PT2DK (GeV^2) >	0.6	0.2	0.35
ZPRI (cm)<	-0.5	-0.5	-0.5
KPROB>	-	-	0.11

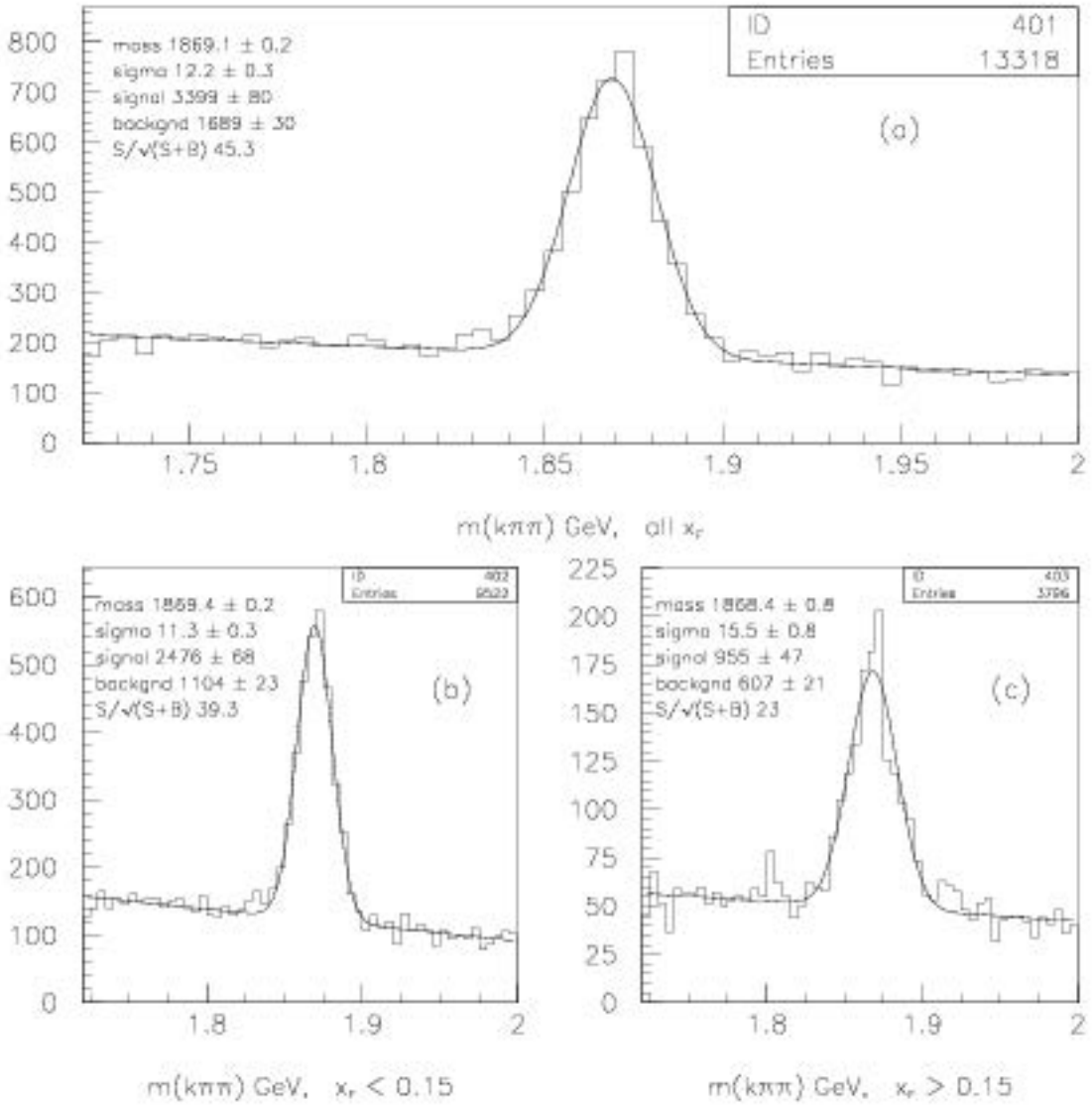

Figure 6.5: D^+ signal for different x_F bins after optimization of cuts (a) all x_F, (b)$x_F < 0.15$, (c)$x_F > 0.15$

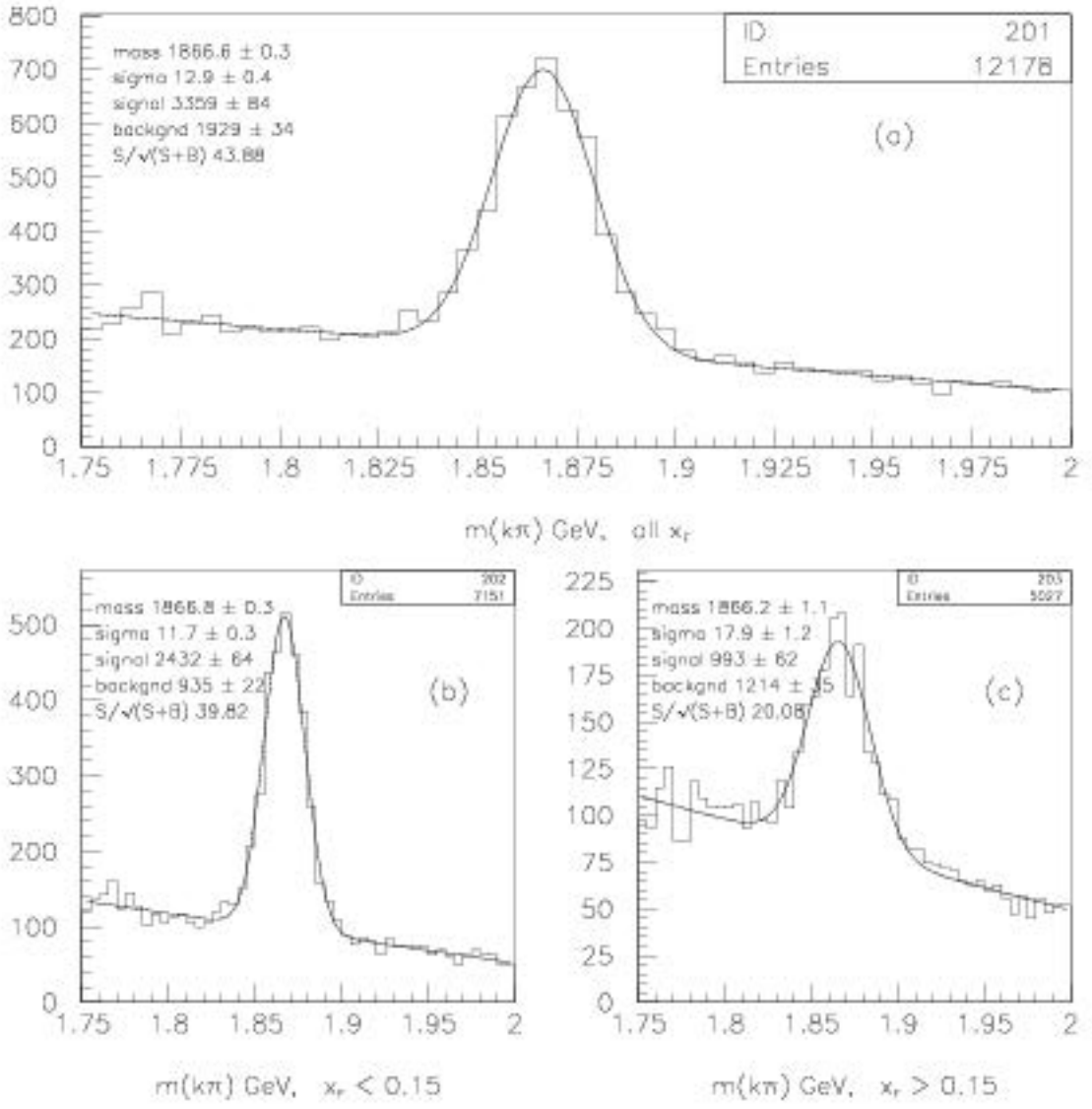

Figure 6.6: D^0 signal for different x_F bins after optimization of cuts, (a) all x_F, (b)$x_F < 0.15$, (c)$x_F > 0.15$

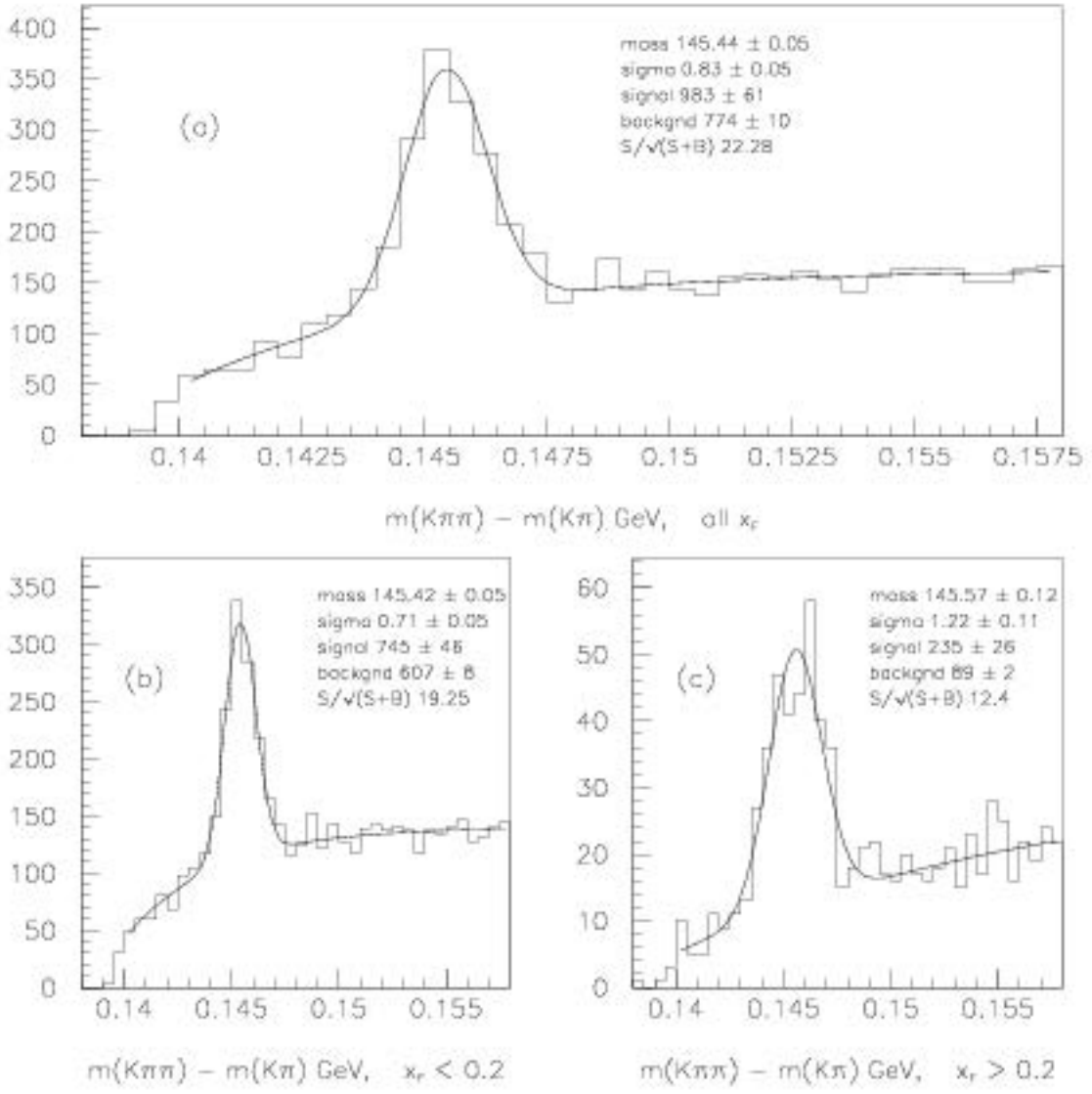

Figure 6.7: D^* signal after optimization of cuts, (a) all x_F, (b) $x_F < 0.2$, (c) $x_F > 0.2$

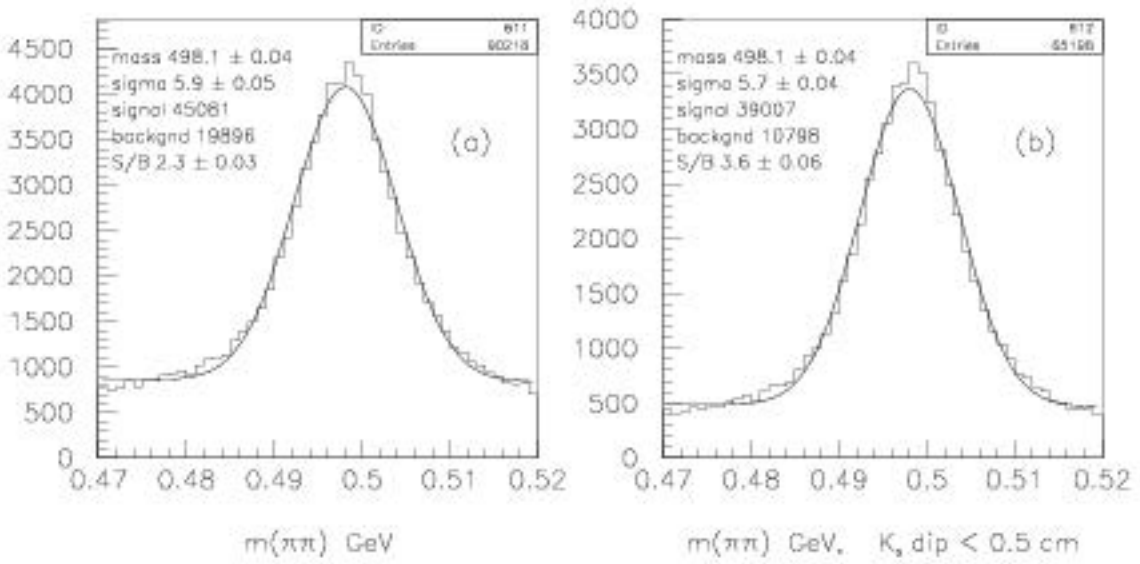

Figure 6.8: (a) K_s before cut on KSDIP, (b) K_s signal, KSDIP $< 0.5cm$

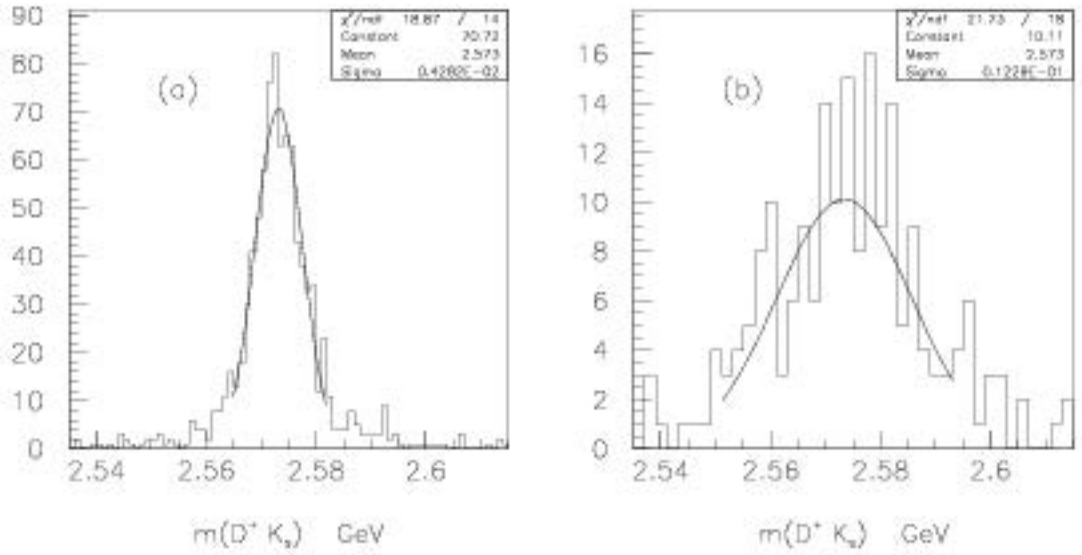

Figure 6.9: Monte Carlo D^{**} (a) KSDIP< 0.5 cm (b) KSDIP> 0.5 cm

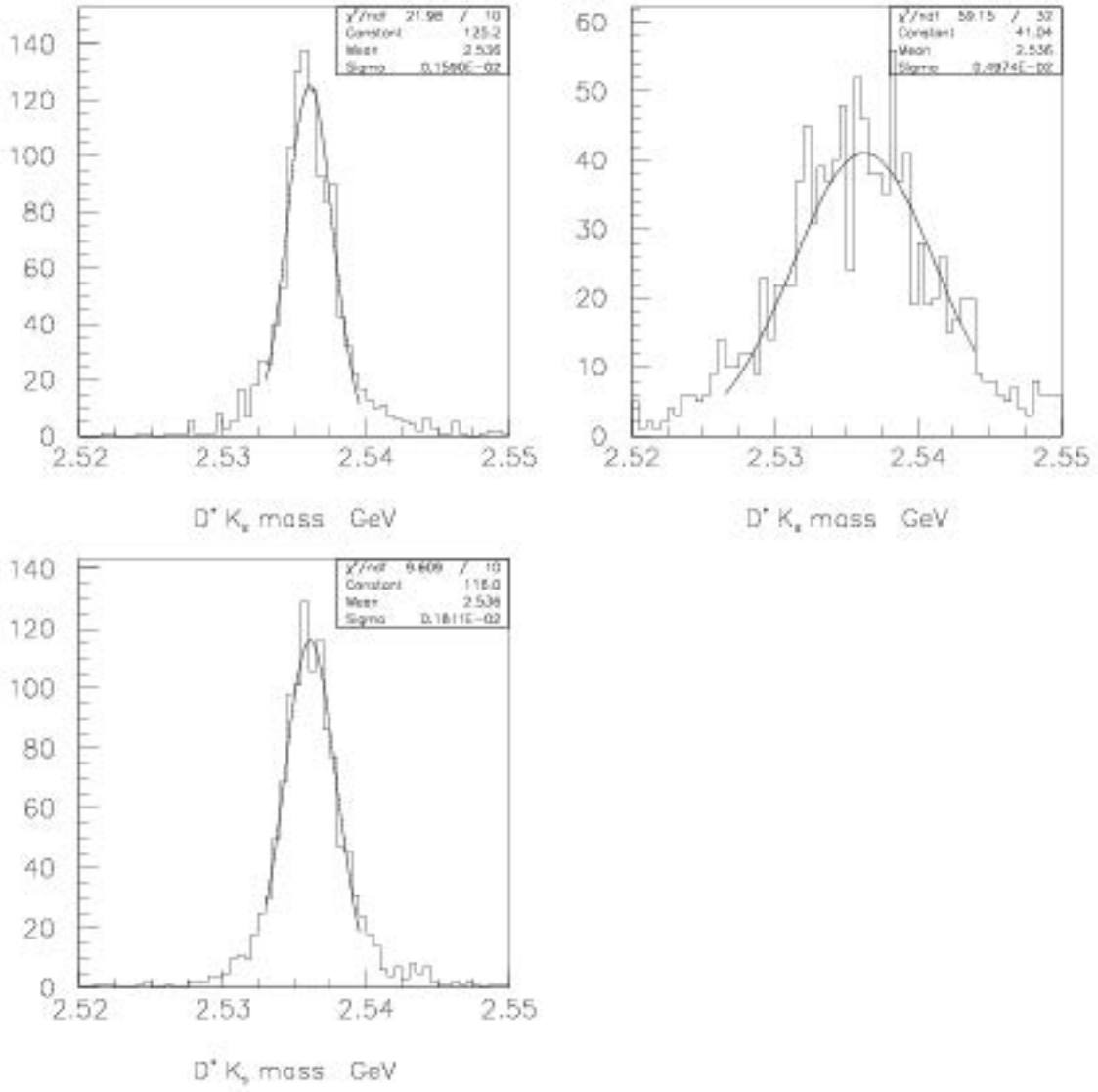

Figure 6.10: Monte Carlo data (a) m(D^* K_s) calculated using nominal values of the D^* and K_s masses, (b) m(D^* K_s) - m(D^*) + 1.8645, (c) m(D^* K_s) - m(D^*) - m(D^*) + 1.8645 + 0.4977

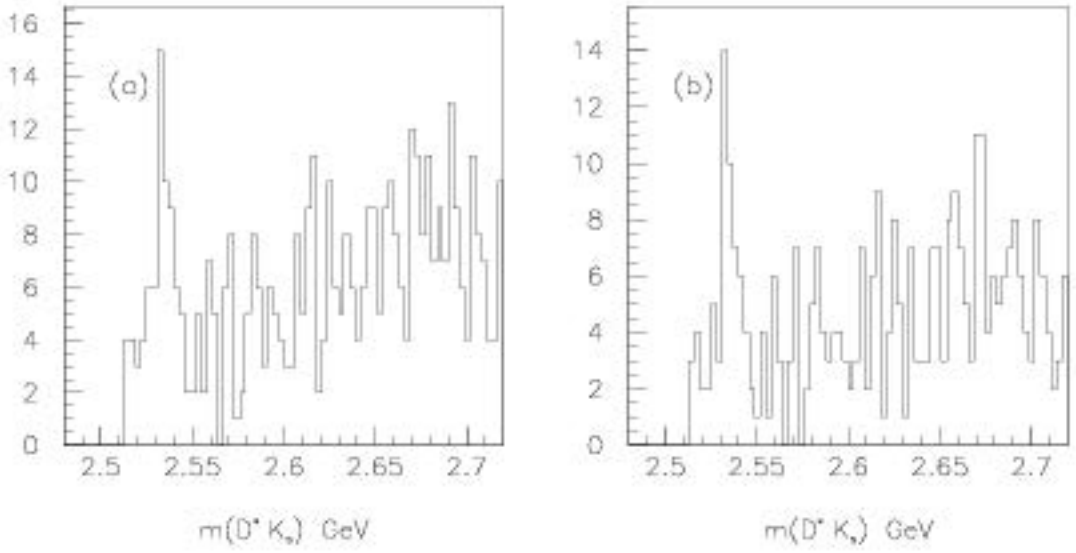

Figure 6.11: m(D^* K_s) (a) no cut on KSDIP (b) KSDIP < 0.5 cm

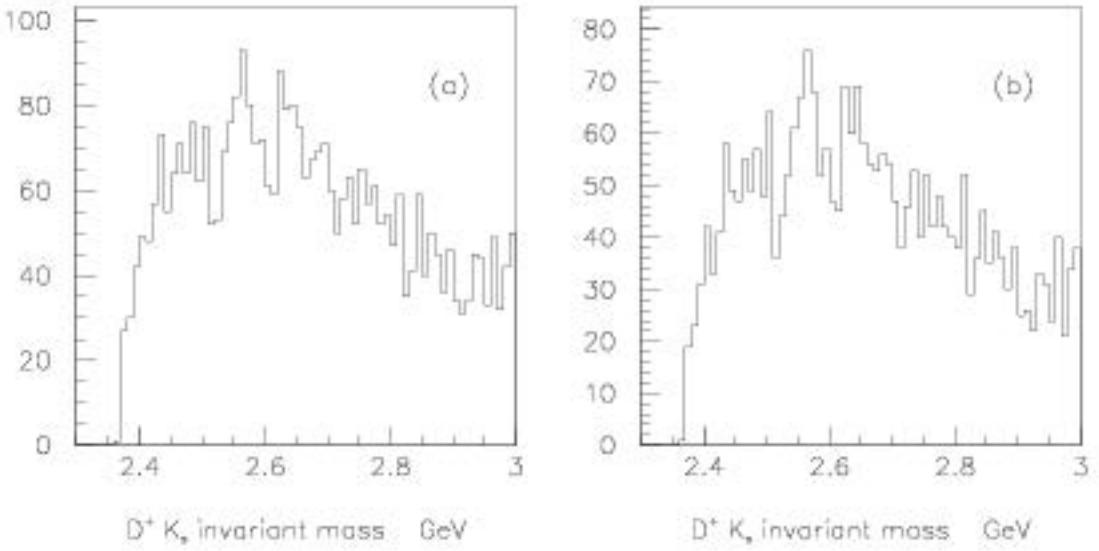

Figure 6.12: D^+ K_s invariant mass, (a) no cut on KSDIP (b) KSDIP < 0.5 cm

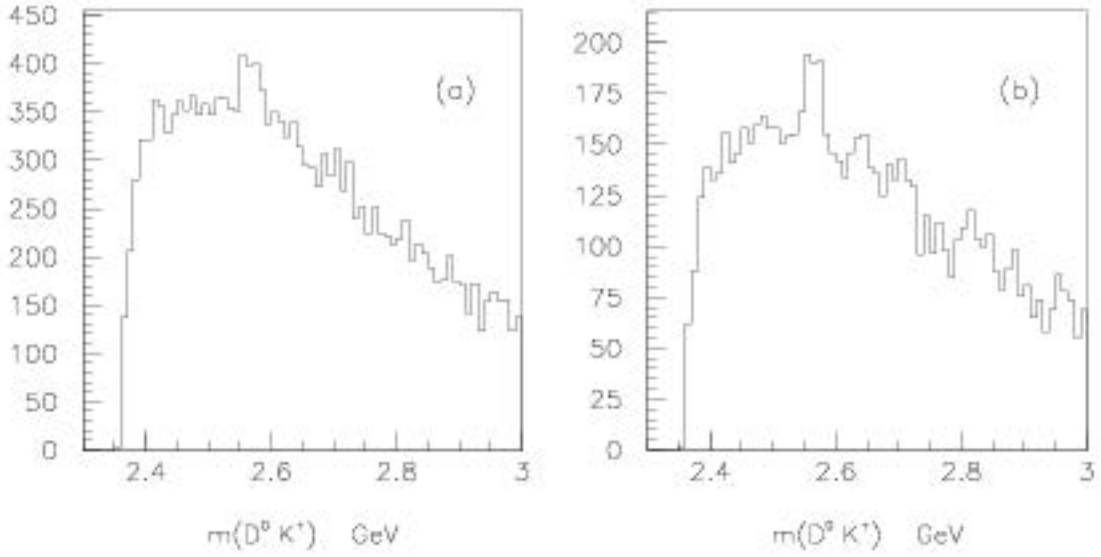

Figure 6.13: D^0 K^+ invariant mass, (a) cut on K^+,$CPRB2(I,4) > 0.13$, (b) cut on K^+,$CPRB2(I,4) > 0.5$

Figure 6.11(a) shows the $D^{*+}K_s$ invariant mass spectrum with no cuts on the K_s. Figure 6.11(b) shows the $D^{*+}K_s$ invariant mass spectrum with KSDIP less than 0.5 cm.

Figure 6.12(a) shows the $D^{+}K_s$ invariant mass spectrum with no cuts on the K_s. Figure 6.12(b) shows the $D^{+}K_s$ invariant mass spectrum with KSDIP less than 0.5 cm.

The D^0K^+ mass spectrum is plotted using the cuts on the D^0 as described above and a $\pm 2\sigma$ mass window. The D^0 is combined with all tracks from the primary vertex that have charge opposite that of the kaon from the D^0 decay and have a Čerenkov kaon probability greater than 0.13. Figure 6.13 shows the D^0K^+ mass spectrum with loose and tight cuts on the Čerenkov kaon probability of the bachelor kaon candidate.

6.4 Background

In order to fit the invariant mass spectra a model for the background shape is needed. The main source of background is combinatoric background where a real or false D combines with a real or false K but the D and the K are not from a D_s^{**} decay. For each of the possible D_s^{**} decay modes I modelled the combinatoric background by taking each D (or D^*) in the signal histogram and combining it with kaons from many other events. It turns out that the background shape is very dependent on the x_P of the D, so I combined each D not with the same number of kaons but rather with enough kaons so that each D in the signal histogram contributed the same number of entries to the mixed event background histogram (*ie.* invariant mass below 3.0 GeV/c^2) In all 3 modes this background shape is fitted to a function of the form

$$const * (x - 2.508)^{P_1} * e^{-P_2 * x} \tag{6.1}$$

Figures 6.14-6.16 show the combinatoric background shape for each of the decay modes.

We also need to consider other sources of background such as reflections from other states where one or more of the decay products is misidentified or where one of the decay products is not observed (eg. π^0 or neutrino).

For the decay modes with a K_s in the final state we need to consider the possibility of misidentifying a Λ^0 as a K_s. Although there are no known $D^*\Lambda^0$ or $D^+\Lambda^0$ resonances, I checked the possibility by plotting the $D^*\Lambda^0$ or $D^+\Lambda^0$ mass and D^*K_s or D^+K_s mass for all events where the K_s was ambiguous with a Λ^0 . There was no significant peak in these plots. I also plotted the D^*K_s and D^+K_s spectra for the ambiguous events (see Fig 6.17).

For the D^0K^+ decay mode there is a possibility that the K^+ is really a π^+ that has passed the Čerenkov cut. I checked this by plotting the D^0K^+ as $D^0\pi^+$. Figure 6.18(a) shows this spectrum with a Čerenkov kaon probability cut $K2ID > 0.13$ on the pion and figure 6.18(b) shows this spectrum with a Čerenkov kaon probability cut $K2ID > 0.5$ on the pion.

There is a significant D^* peak for $K2ID > 0.13$ and still a small fraction of D^*

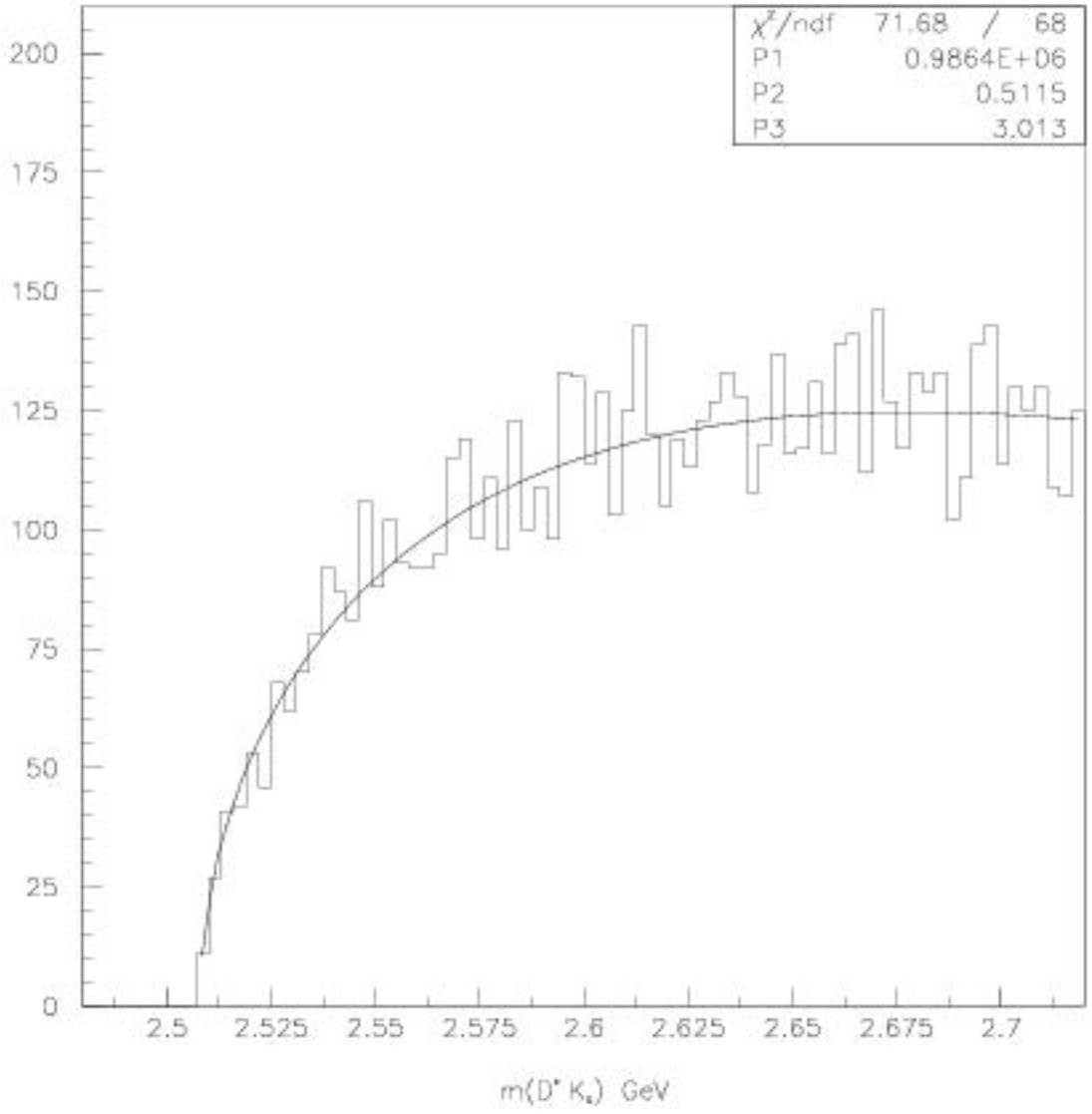

Figure 6.14: D^* K_s combinatoric background from mixed events

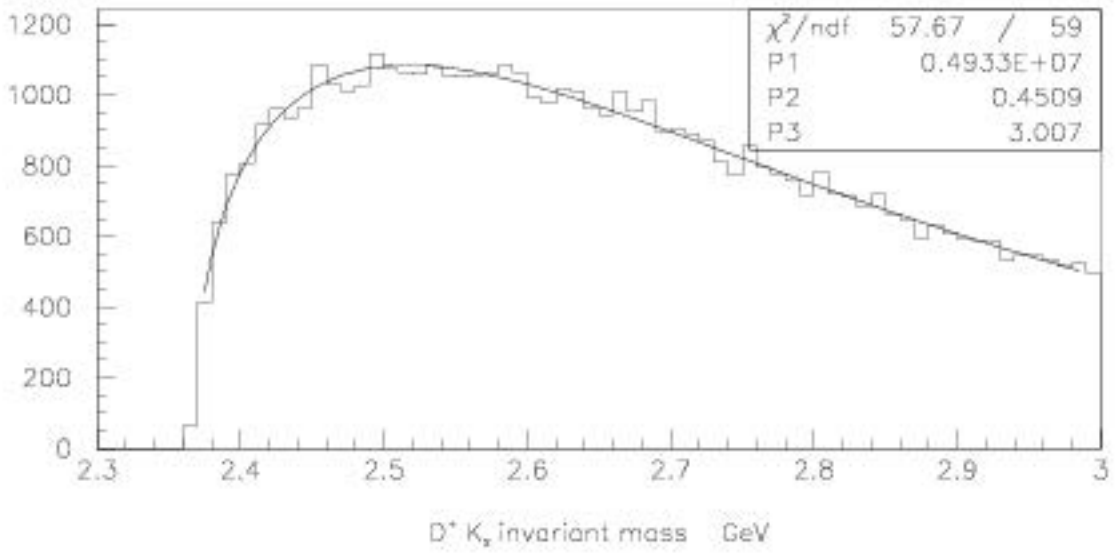

Figure 6.15: D^+ K_s combinatoric background from mixed events

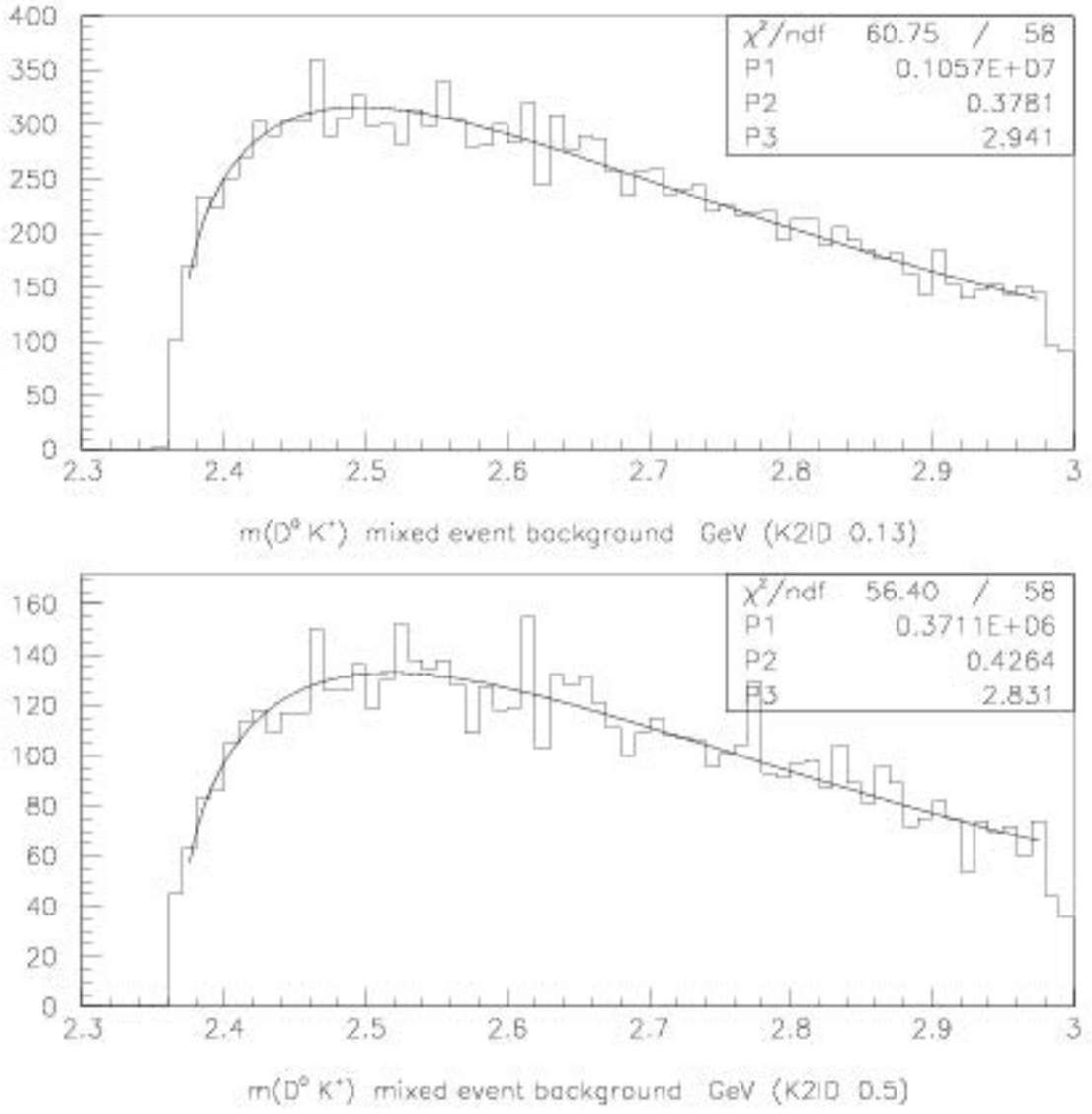

Figure 6.16: $D^0\ K^+$ combinatoric background from mixed events (a) $K2ID > 0.13$ (b) $K2ID > 0.5$

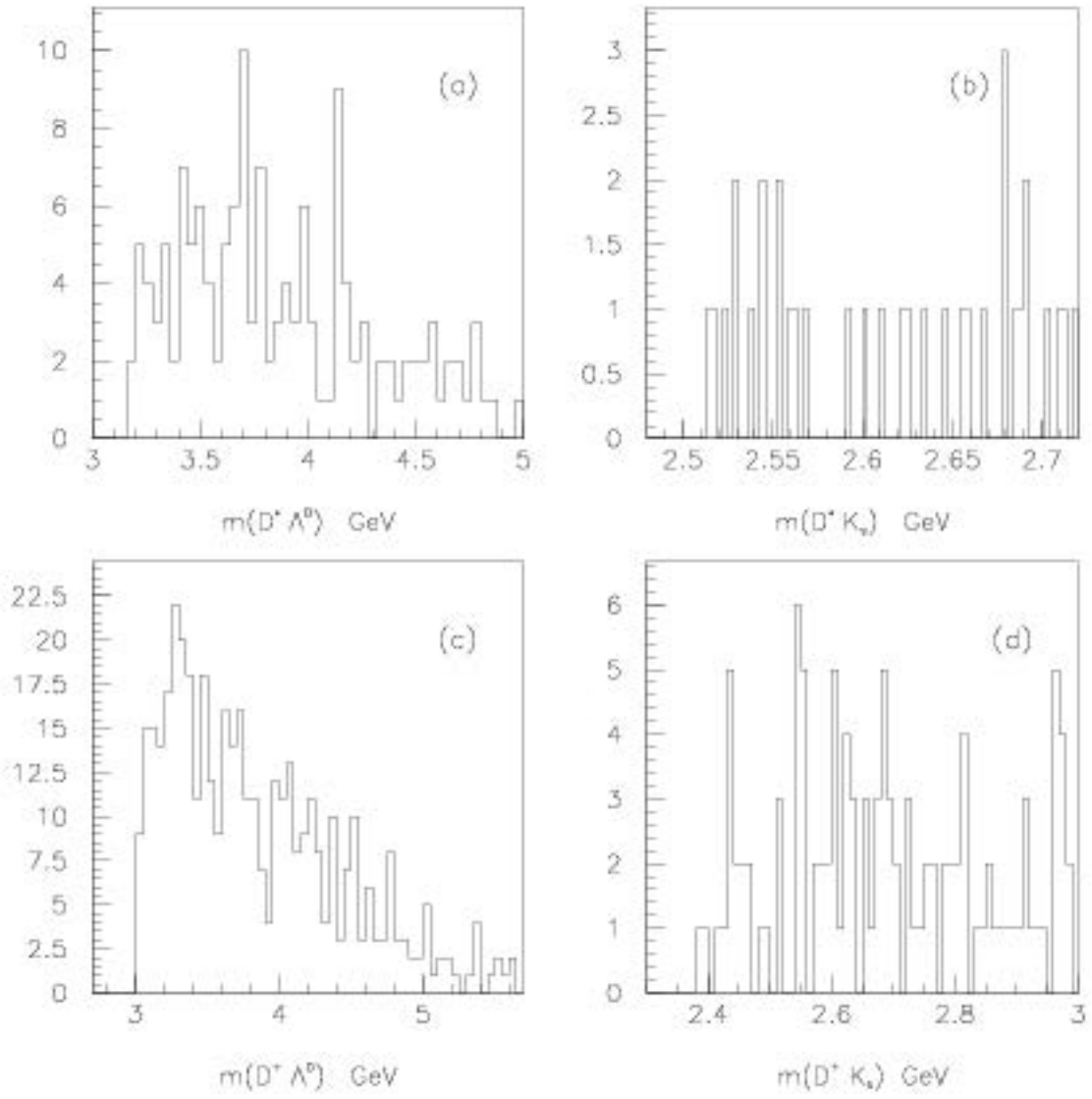

Figure 6.17: Mass spectra for events where the K_s is ambiguous with a Λ^0

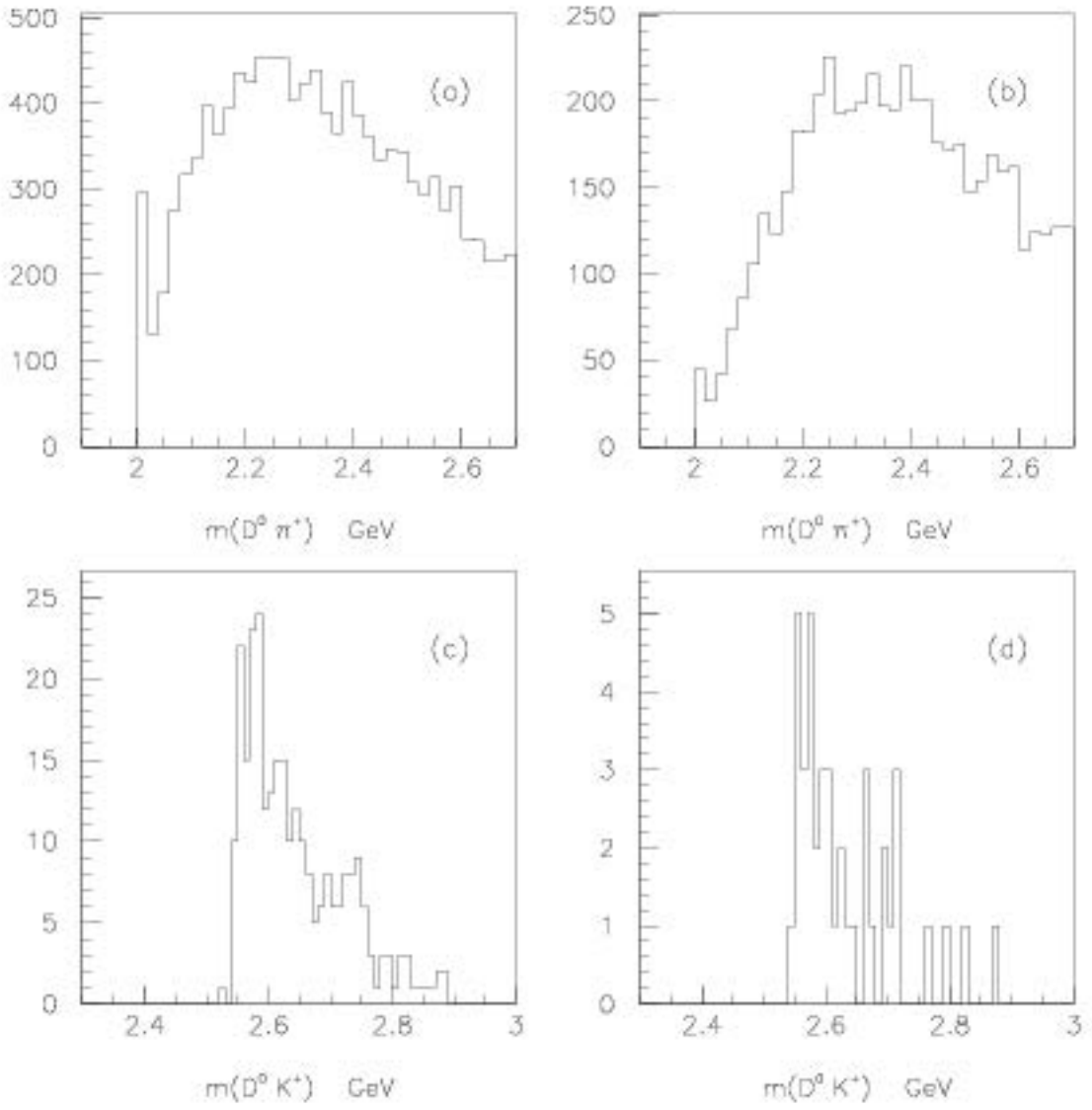

Figure 6.18: (a) $D^0\pi^+$ spectrum where the π^+ has a probability of being a K^+ K2ID>0.13, (b) $D^0\pi^+$ spectrum, K2ID>0.5, (c) D^0K^+ spectrum for events identified as D^*, K2ID>0.13, (d) D^0K^+ spectrum for events identified as D^*, K2ID>0.5

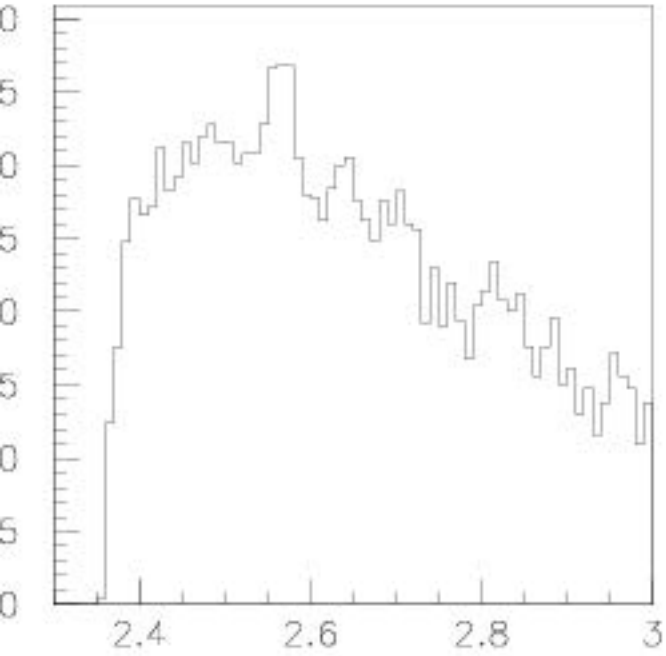

Figure 6.19: D^0K^+ invariant mass spectrum with D^* events removed (K^+ Čerenkov probability > 0.5)

even when the Čerenkov kaon probability is increased to 0.5. There is no evidence of the non-strange D^{**} at 2460 MeV/c^2. Taking the events in the D^* peak and plotting them as D^0K^+, I find a strong peak between 2550 MeV/c^2 and 2600 MeV/c^2 (see Fig. 6.18 (c)). I replot the D^0K^+ invariant mass spectrum removing all events where m($D^0\pi^+$) - m(D^0) is less than 150 MeV/c^2 (see Fig. 6.19).

Chapter 7

THE D^*K_S SPECTRUM

7.1 Fitting the Mass and width of the $D_{s1}^{**}(2535)$

There is a peak in the D^*K_s mass spectrum near the D_s^{**} state at 2535 MeV/c^2. Figure 7.1 shows the result of a fit with combinatoric background as described above and a gaussian. I find a signal with a mass of 2533 ± 1 MeV/c^2 and a gaussian width of 4 ± 1 MeV/c^2. Monte Carlo events were created with an intrinsic width of zero so the reconstructed width gives a measure of the resolution of the spectrometer for this mode. Figure 6.10(a) shows the fitted Monte Carlo peak. It can be seen that the peak has a gaussian width of 1.6 MeV/c^2 which is narrower than the data peak. This could be because the D_s^{**} has an intrinsic width comparable to or larger than the resolution or because the Monte Carlo width is an underestimate of the experimental resolution.

An independent check of the reliability of the Monte Carlo width can be made using the D^* peak. This D_s^{**} decay mode has a low Q value (25 MeV). The $D^{*+} \to D^0\pi^+$ decay also has a low Q value so I compared the width of the Monte Carlo D^* peak with data to see if there was reasonable agreement. The results can be seen in Figure 7.2. The width of the D^* is well modelled in the Monte Carlo when the bachelor pion is a SESTR track, however when the bachelor pion is an ESTR track the D^* is about 30% wider in data than in Monte Carlo. Almost all of the events in the D_s^{**} peak contain an ESTR K_s so it is the ESTR width that is most

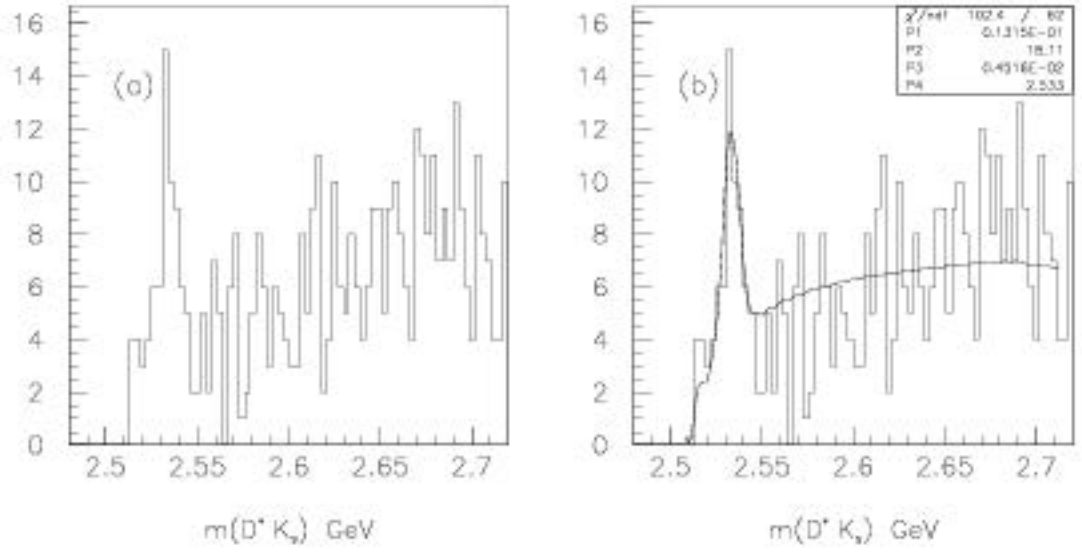

Figure 7.1: (a) D^*K_s spectrum, (b) fit with mixed event background and gaussian signal

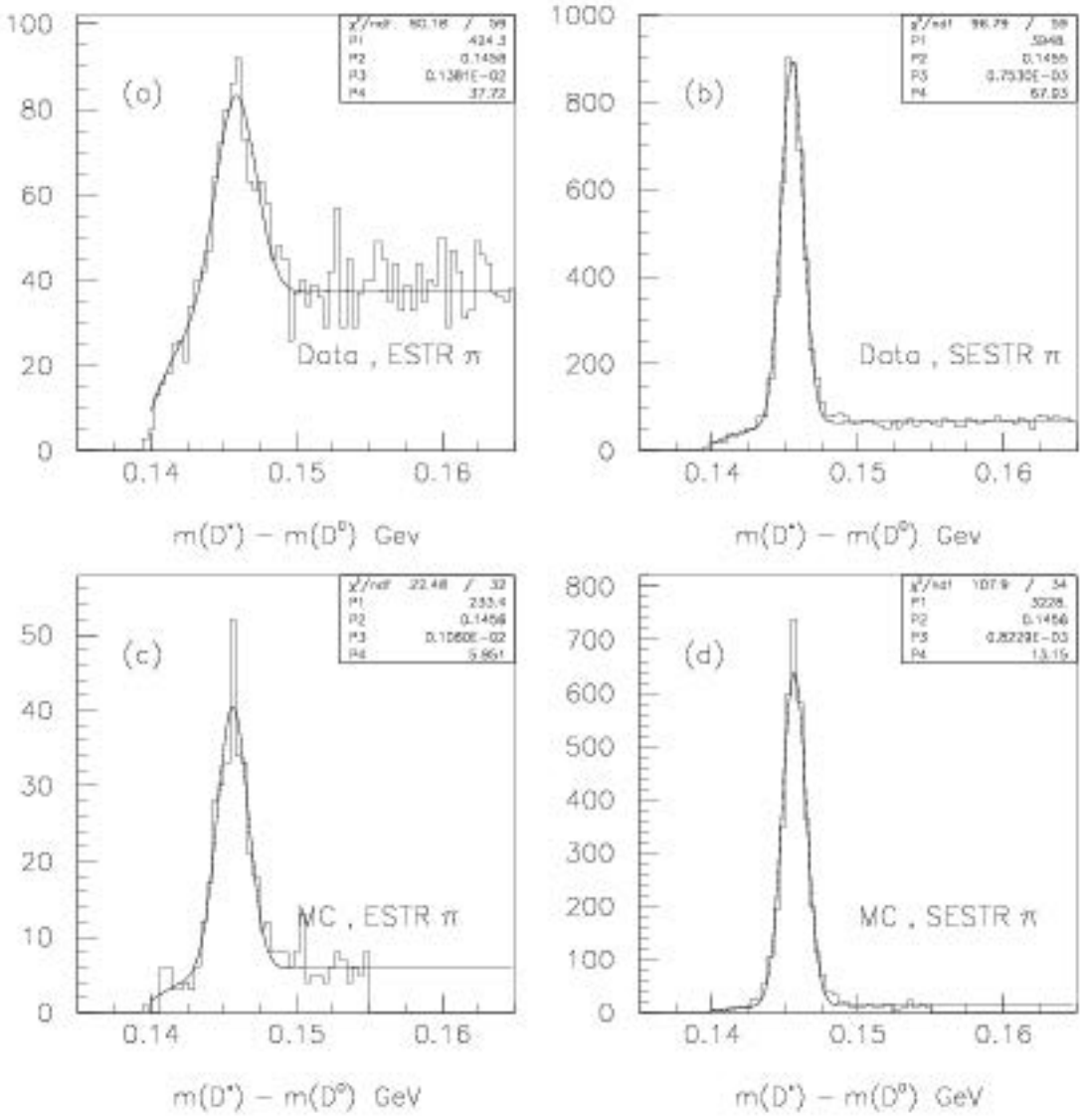

Figure 7.2: D^* width — Comparison of Monte Carlo and Data

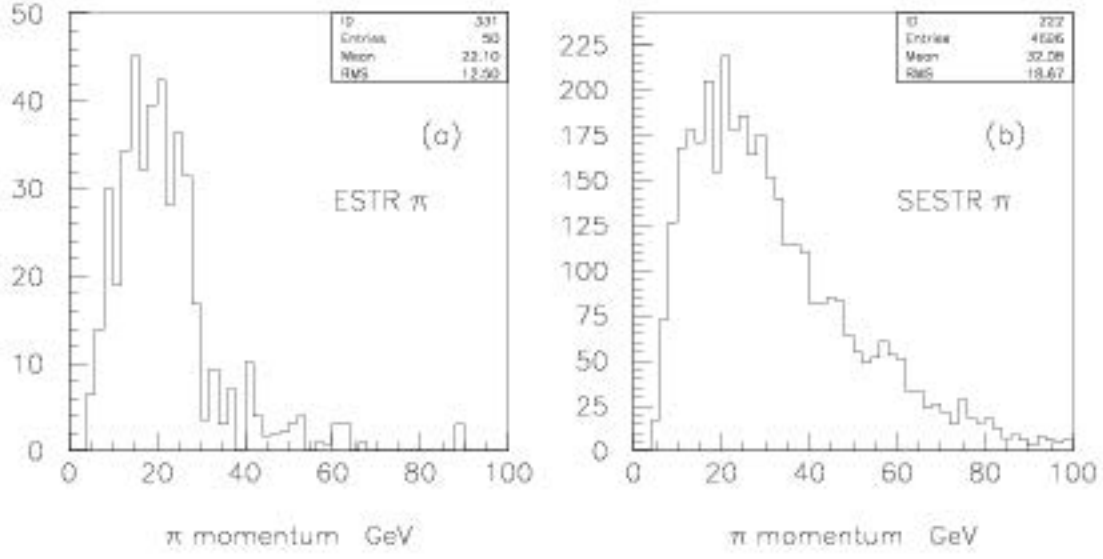

Figure 7.3: Background subtracted momentum distributions of bachelor π in D^* decays

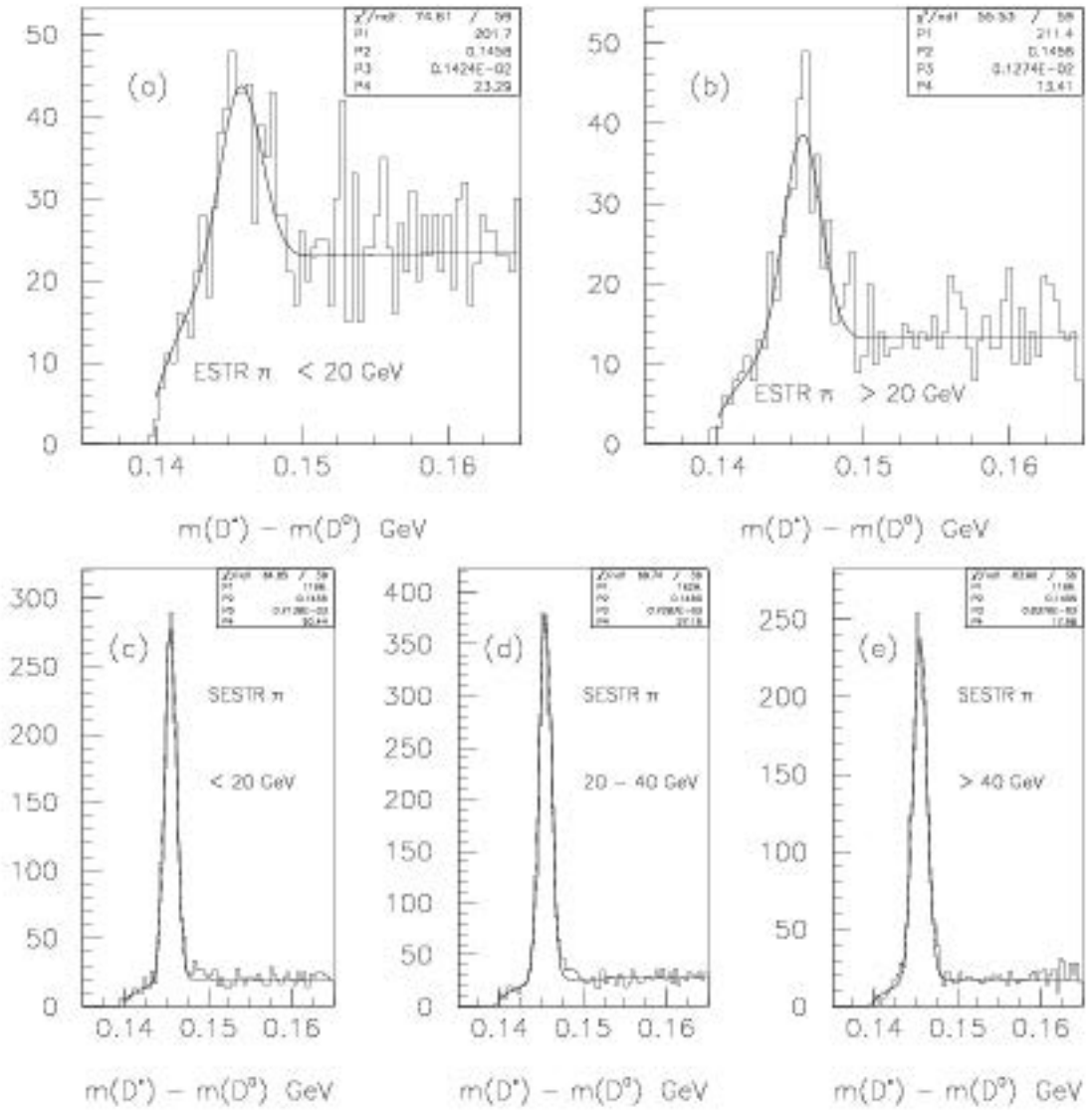

Figure 7.4: D^* width as a function of bachelor π momentum

important to estimate correctly. It is possible that the difference is due to the different momentum distributions in these 2 cases. Figure 7.3 shows the background subtracted momentum distribtutions for the bachelor pions. I checked that the width was not strongly dependent on the momentum of the bachelor pion by plotting the D^* - D^0 mass difference for different momentum bins of the bachelor pion (see Fig. 7.4). It is possible that the increased width of the D^* for ESTR pions is partially due to the fact that the pions underwent larger than average multiple scattering in the SMDs and therefore were not reconstructed there. This is not a problem for ESTR K_ss because they decay downstream of the SMDs. However a comparison of the width of the D^* between Monte Carlo and data can give an estimate of the systematic error due to using the Monte Carlo width in fitting the D_s^{**}.

As the D_s^{**} is wider than the expected resolution I fitted the peak with a Breit-Wigner convoluted with a gaussian. The fit was done both with and without the cut on KSDIP for 2 different widths of gaussian — first with a width of 1.7 MeV/c^2 as predicted by the Monte Carlo and second with the width increased by 30% *ie.* 2.2 MeV/c^2. I used an unbinned maximum likelihood fit and the results are shown in Table 7.1. It can be seen from the table that there is a difference of 0.9 MeV/c^2 between the fitted widths using a loose and tight KSDIP cut. The variation in width from using a different width gaussian is 0.4 MeV/c^2. The projections of the fits using a gaussian width of 1.7 MeV/c^2 are shown in Figure 7.5.

There is a possible systematic error due to not using the correct background shape. I fitted the background outside the peak region with a curve of the same form as the mixed event background to get new parameters P1 and P2 in equation 6.1. Fixing these parameters, I then refitted the peak and background. The results of the new fit are given in Table 7.2 and the projection of the fit is shown in Figure 7.5. With this background shape the fitted Breit-Wigner width increases by about 4.5 MeV/c^2. This is the dominant source of systematic error. The systematic error on the width is obtained by adding in quadrature the errors from the variation in background shape, gaussian width and KSDIP cut. The systematic error on the mass is dominated by the variation in the KSDIP cut plus another 0.5 MeV is added due to the uncertainty

Table 7.1: Results of fit to D^*K_s spectrum, background shape from mixed events

	Gaussian width MeV/c^2	Mass MeV/c^2	Breit-Wigner width MeV/c^2
loose KSDIP cut	1.7	2533.3 ± 1.2	3.3 ± 3.7
	2.2	2533.4 ± 1.4	2.9 ± 3.9
Tight KSDIP cut	1.7	2533.8 ± 1.2	2.4 ± 3.3
	2.2	2533.9 ± 0.9	2.0 ± 3.6

in the D^0 mass.

The mass of the D_s^{**} is measured to be
$(2533.5 \pm 1.4(\text{statistical}) \pm 0.8(\text{systematic}))$ MeV/c^2

The intrinsic width of the D_s^{**} is measured to be
$(5.0 \pm 3.6(\text{statistical}) \pm 2.3(\text{systematic}))$ MeV/c^2

7.2 Angular Distribution of the $D^{*+}K_s$ decay

The distribution of the angle θ between the K from the D^{**} decay and the π from the D^* decay in the D^* rest frame is determined by the spin of the D^{**} (see Section 1.4). The $D^{*+}K_s$ spectrum with a tight KSDIP cut is shown in Figure 7.6. The signal region to be used for determining the angular distribution is shaded. To determine the angular distribution of the background under the signal I use the mixed event sample and scale this to 2 events per bin.

The angular distributions of signal and background are shown in Figure 7.7 together with the distribution from Monte Carlo events. The Monte Carlo events were

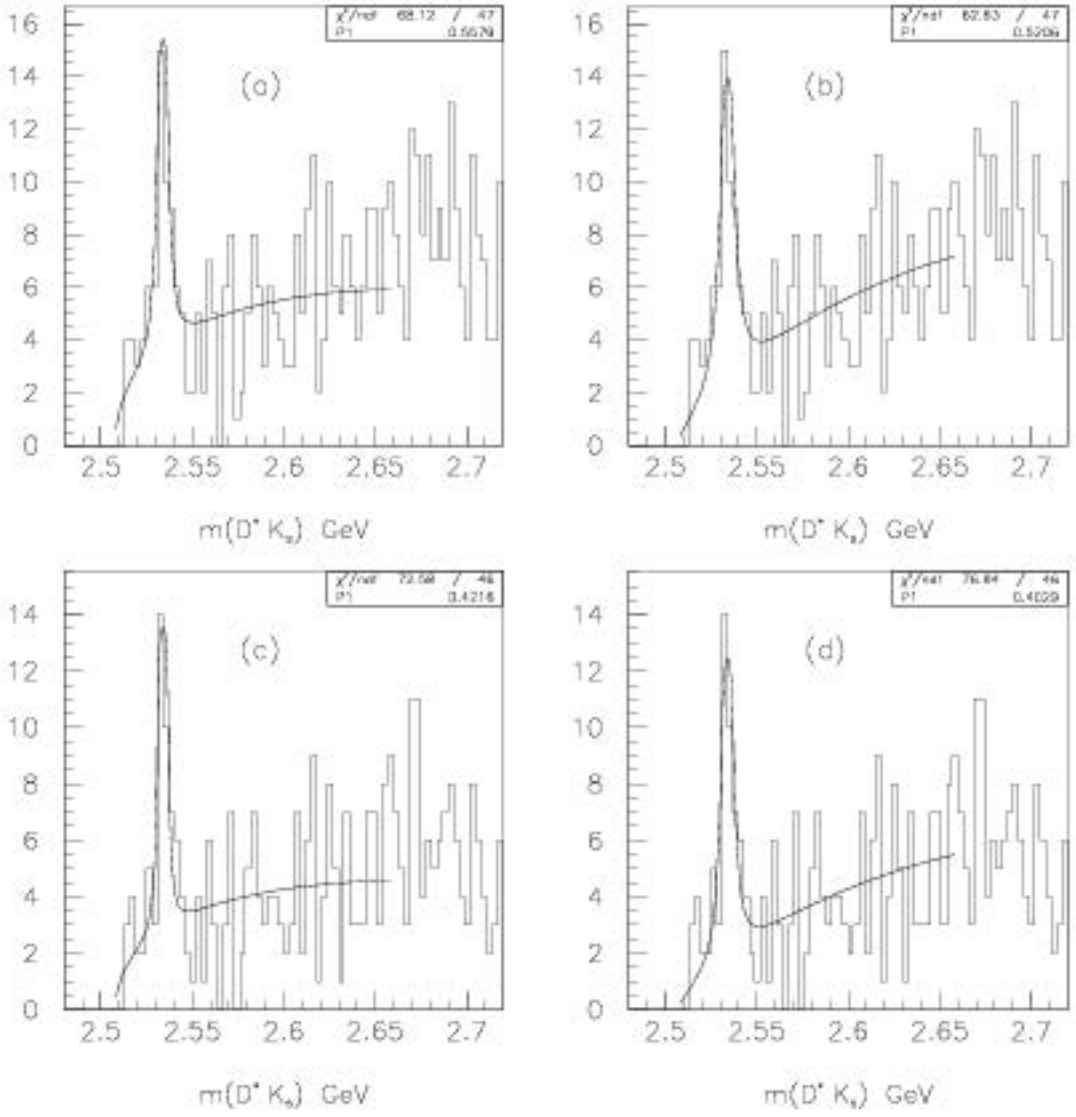

Figure 7.5: D^*K_s spectrum — projection of unbinned fit (a) Loose KSDIP cut, mixed event background, (b) Loose KSDIP cut, background fit to data, (c) Tight KSDIP cut, mixed event background, (d) Tight KSDIP cut, background fit to data

Table 7.2: Results of fit to D^*K_s spectrum, background shape fitted from data

	Gaussian width MeV/c^2	Mass MeV/c^2	Breit-Wigner width MeV/c^2
loose KSDIP cut	1.7	2533.2 ± 1.6	8.0 ± 3.6
	2.2	2533.1 ± 1.6	7.7 ± 3.7
Tight KSDIP cut	1.7	2533.8 ± 1.4	6.8 ± 3.5
	2.2	2533.9 ± 1.4	6.5 ± 3.6

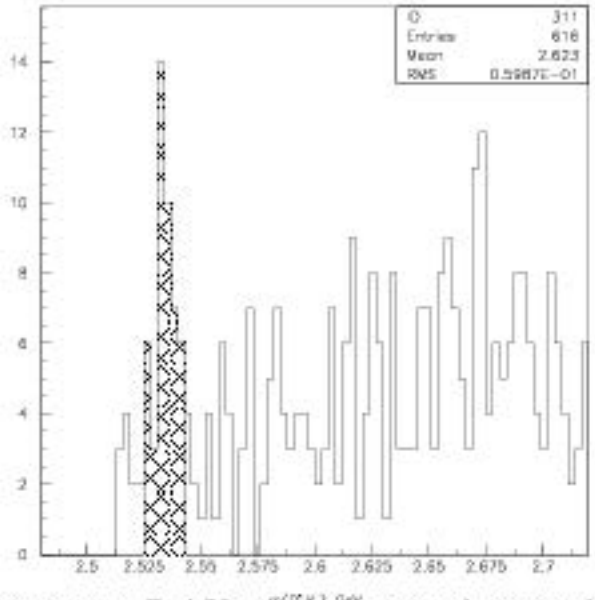

Figure 7.6: $D^{*+}K_s$ spectrum, signal region shaded

generated with a flat distribution and the reconstructed events have a flat distribution within errors. The signal-background disribution is shown in Figure 7.7(d) with a fit to the equation $1 + \beta \cos^2 \theta$. The result of the fit is $\beta = -0.08 \pm 0.68$. This is consistent with the S-wave decay of a $J = 1$ D^{**} meson.

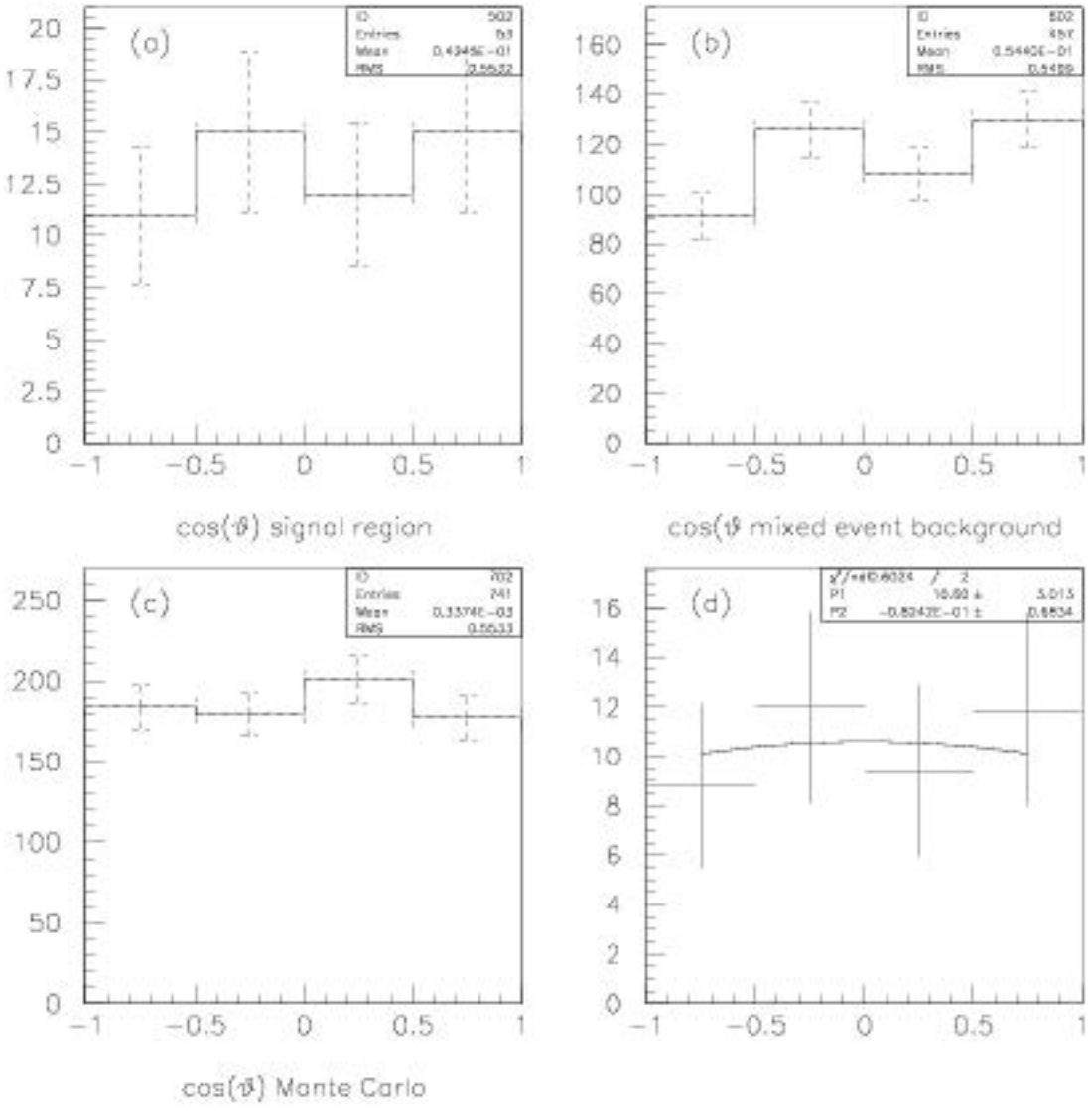

Figure 7.7: $D^{*+}K_s$ angular distribution, (a) signal region, (b) mixed event background, (c) Monte Carlo, (d) signal - scaled background,

Chapter 8

THE D^+K_S AND D^0K^+ SPECTRA

8.1 Fitting the Mass and Width of Observed Peaks

The D^+K_s spectrum appears to show two peaks, neither of which is the state at 2535 MeV/c^2 seen in the D^*K_s spectrum.

Looking at the D^0K^+ spectrum we find that even after removal of events which would be consistent with a D^* we see some evidence of a signal in the region 2550 - 2600 MeV/c^2 and perhaps another peak at about 2640 MeV/c^2.

Although statistics are poor it is interesting that there is some evidence of two peaks in both decay modes. This is unexpected because only two of the D_s^{**} states are expected to be this narrow [26] and as the state at 2535 MeV/c^2 is well established, we would expect to find only one other narrow state.

I fit both these spectra with a background shape from mixed events and two gaussians. The fits are also done with just a single gaussian plus background in order to determine the significance of the second peak. The results of the fits are shown in Figures 8.1 -8.2. The χ^2/degree of freedom decreases from 111/59 to 93/56 for the D^+K_s mode but there is very little improvement in the fit adding a second peak in the fit to the D^0K+ mode.

As in the D^*K_S spectrum the peaks are wider than the resolution as determined from the Monte Carlo. Monte Carlo events were created with zero width at a mass of 2573 MeV/c^2. The fit to the D^+K_s peak is shown in Figure 6.9. It has a width of

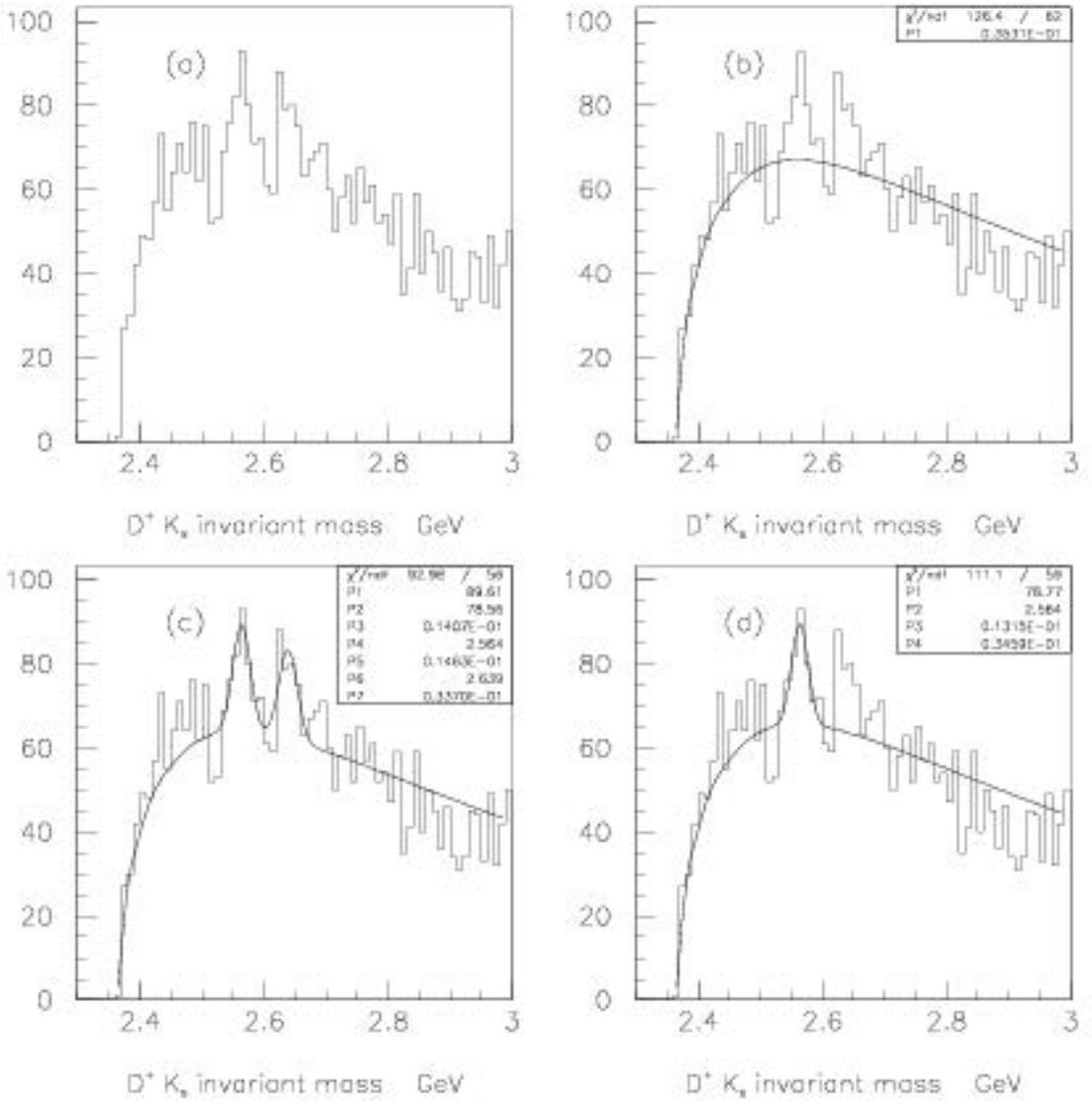

Figure 8.1: Fits to D^+K_s spectrum, (b) mixed event background only, (c) mixed event background plus two gaussians, (d) mixed event background plus one gaussian

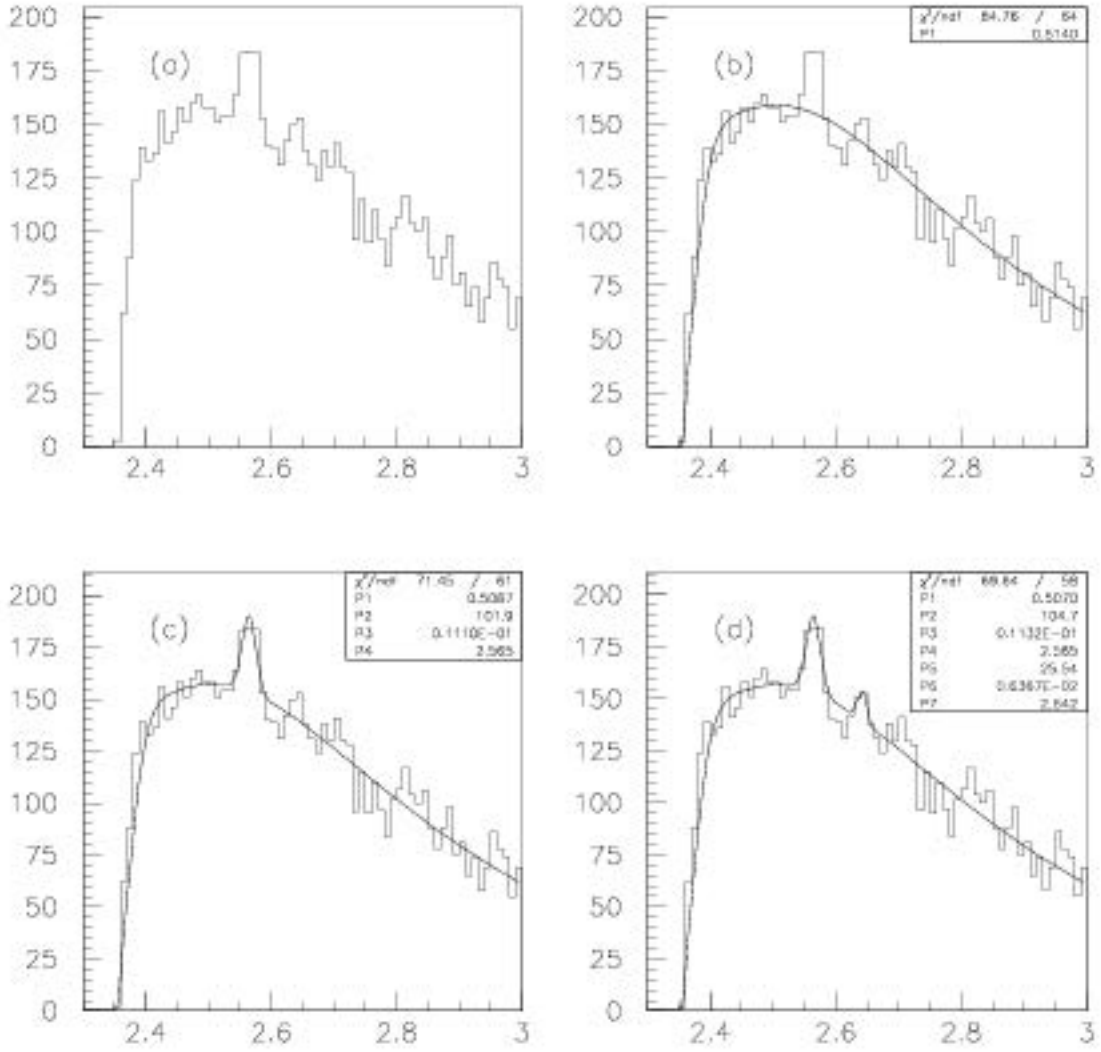

Figure 8.2: Fits to D^0K^+ spectrum, (b) mixed event background only, (c) mixed event background plus one gaussian, (d) mixed event background plus two gaussians

Table 8.1: Results of D_s^{**} fits

fit parameter	Decay Mode D^+K_s	D^0K^+
Mass 1 (MeV/c^2)	2567 ± 5	2565 ± 5
Width 1 (MeV/c^2)	16 ± 12	21 ± 10
Mass 2 (MeV/c^2)	2645 ± 5	2644 ± 7
Width 2 (MeV/c^2)	20 ± 23	11 ± 16

4.5 ± 0.13 MeV/c^2. If we assume that this is underestimated by 30% it is still much narrower than the fitted data peak which has a width of 15 ± 4 MeV/c^2.

The Monte Carlo peak for the D^0K^+ events is shown in Figure 8.3. It can be seen in this case that the width is 3.2 ± 0.2 MeV/c^2 which is narrower than the data peak (11 ± 3 MeV/c^2).

The decay $D_s^{**} \to D^0K^+$ has a similar Q-value to $K_s \to \pi^+\pi^-$. One can compare the width of the K_s peak between Monte Carlo and data to estimate the accuracy of the Monte Carlo width of the D_s^{**}. From Figure 8.4 we can see that the Monte Carlo underestimates the width of the SESTR K_s peak by about 25%.

I refitted both the D^+K_s and D^0K^+ spectra with two Breit-Wigners convoluted with gaussians, using a gaussian width of 5.0 Mev/c^2 for the D^+K_s and 4.3 MeV/c^2 for the D^0K^+. I used a D-wave Breit-Wigner for the lower mass peak because it is predicted to be a spin 2 state which decays through a D-wave. The results are shown in Table 8.1 and the fits are shown in Figure 8.5.

The systematic errors were estimated by studying the variation in fit parameters with

- changes in width of gaussian

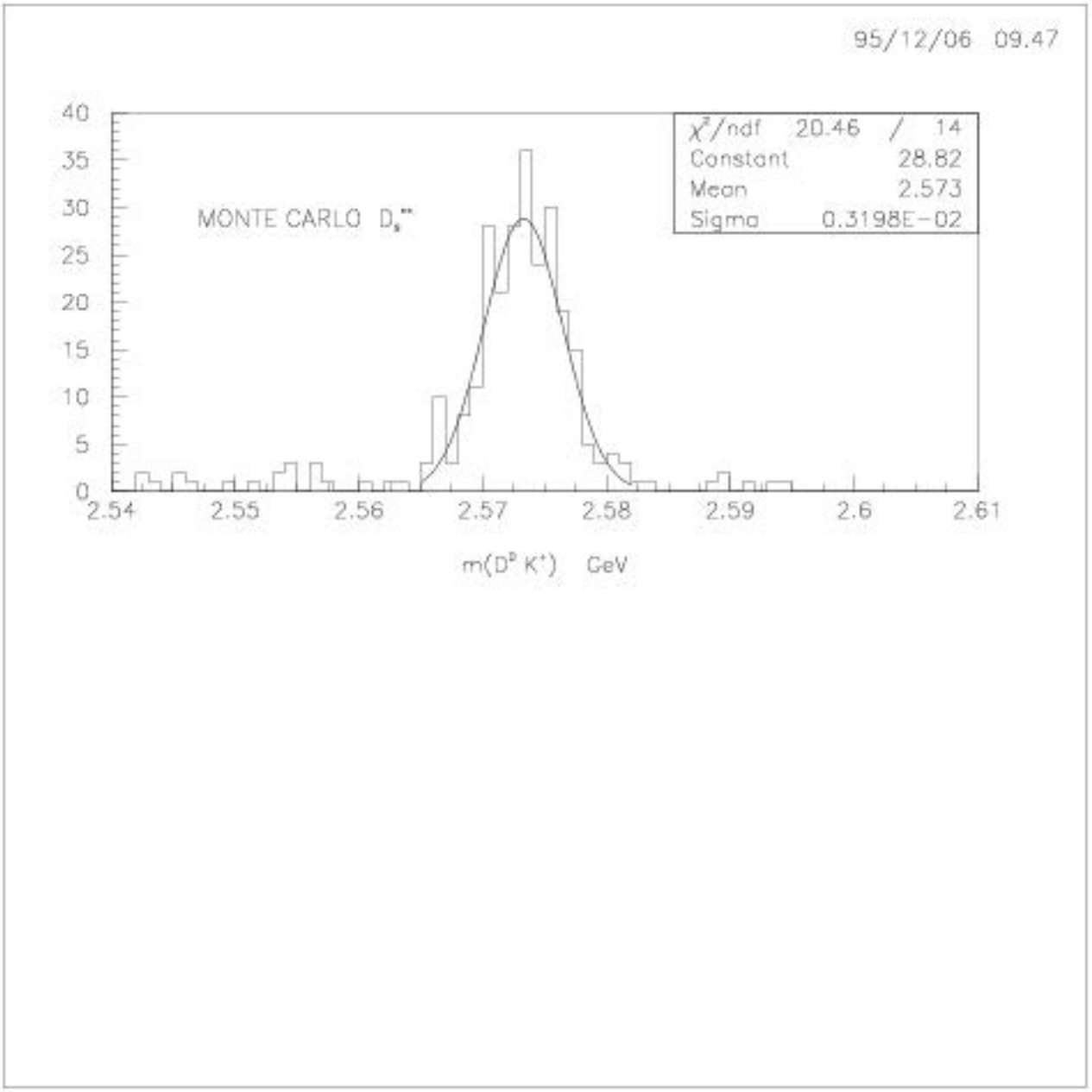

Figure 8.3: Monte Carlo D^0K^+ signal

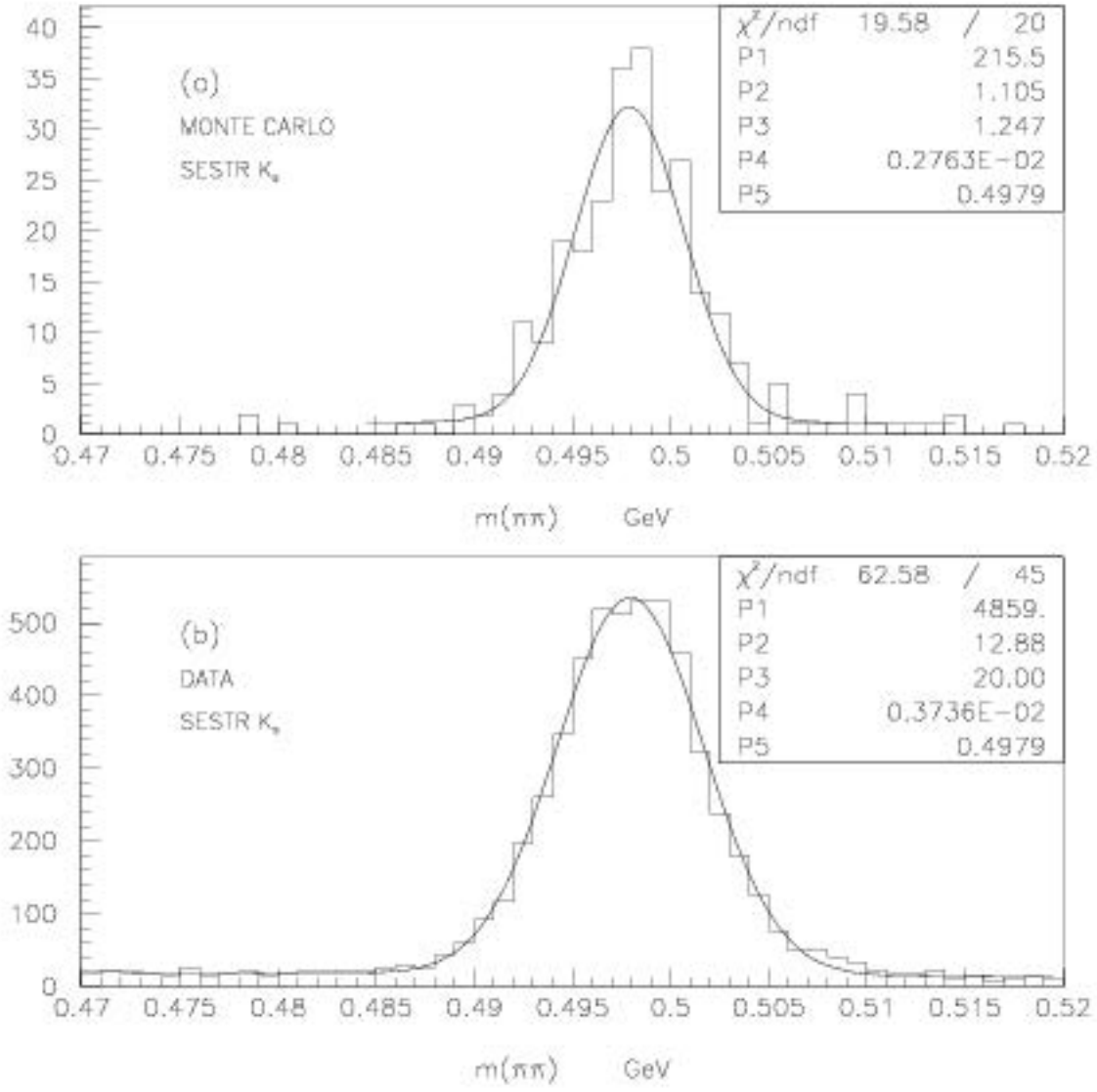

Figure 8.4: SESTR K_s spectrum - comparison of Monte Carlo and Data

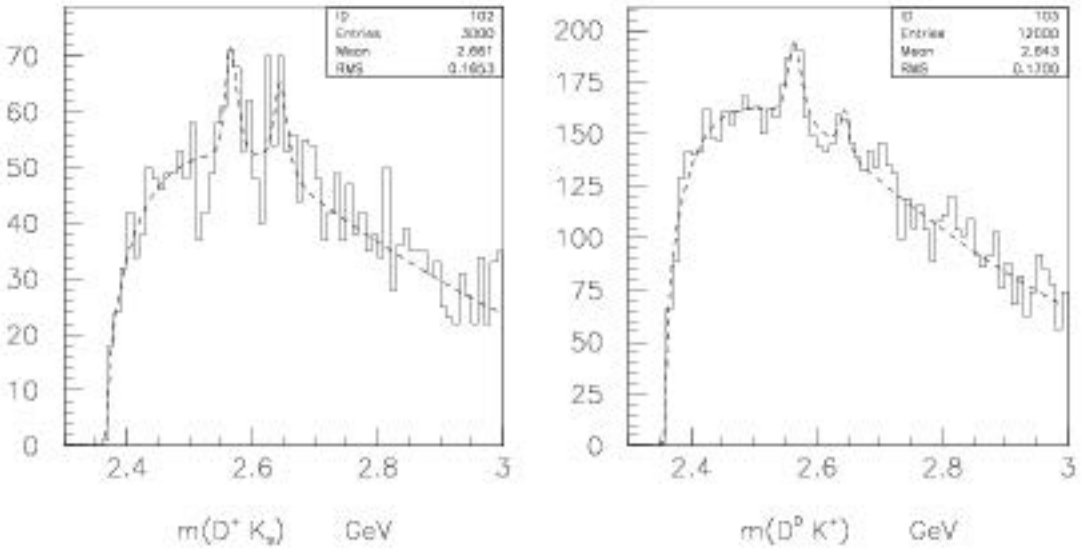

Figure 8.5: Projection of Breit-Wigner convoluted with gaussian fits, (a) D^+K_s, (b) D^0K^+

Table 8.2: Sources of Systematic Errors in D_s^{**} Parameters

source	Contribution to error in MeV/c^2			
	Mass 1	Width 1	Mass 2	Width 2
vary gaussian width by $\pm$ 1.0 MeV/c^2	0.2	2.0	0.2	2.0
use S-wave Breit-Wigner	1.0	2.0	1.0	2.0
vary cuts	5.0	2.0	5.0	2.0
mass scale	0.5	-	0.5	-

- using an S-wave instead of D-wave Breit-Wigner.

- changes in cuts: the dominant source of error came from changing the Čerenkov cut on the kaon from the D^0 and D^+.

For the Monte Carlo peak, the reconstructed value agrees with the thrown value within statistical errors in both decay modes. There is another systematic error due to the fact that all masses are tied to the mass of the D meson which has an uncertainty of 0.5 MeV for the D^0 and 0.7 MeV for the D^+.

The sources of systematic error are shown in Table 8.2.

Possible explanations for the unexpected second peak are:

- The second peak is a statistical fluctuation.

- there is one peak but it is split due to some problem with reconstruction. For example if there were a misalignment between the SMD frame of reference and the Drift Chamber frame. (This would only cause a problem in the D^+K_s mode.) The tracks forming the D^+ are reconstructed in the SMDs but for most of the K_s's the tracks are reconstructed in the Drift Chambers. A misalignment between the two coordinate frames could cause the angle between the D^+ and the K_s to be underestimated in some events and overestimated in others. I plotted the D^+K_s invariant mass for events where $dx/dz(D^+) > dx/dz(K_s)$ and also for events where $dx/dz(D^+) < dx/dz(K_s)$ (see Figs. 8.6). There was no evidence of any separation of peaks due to misalignment. Similarly I checked events for misalignment in the y-direction but found none.

- The two peaks are the 0^+ and 2^+ states. It is very likely that the resonance at 2573 MeV/c^2 is the 2^+ state because we would expect the mass splitting within the $j = 3/2$ doublet to be very close to that of the non-strange $j = 3/2$ doublet. Looking at the p-wave kaons ($K_0^*(1430)$,$K_2^*(1430)$) we see that the $J = 0$ state is slightly heavier than the $J = 2$ state, so it is possible that this is also the case for the charm p-wave mesons.

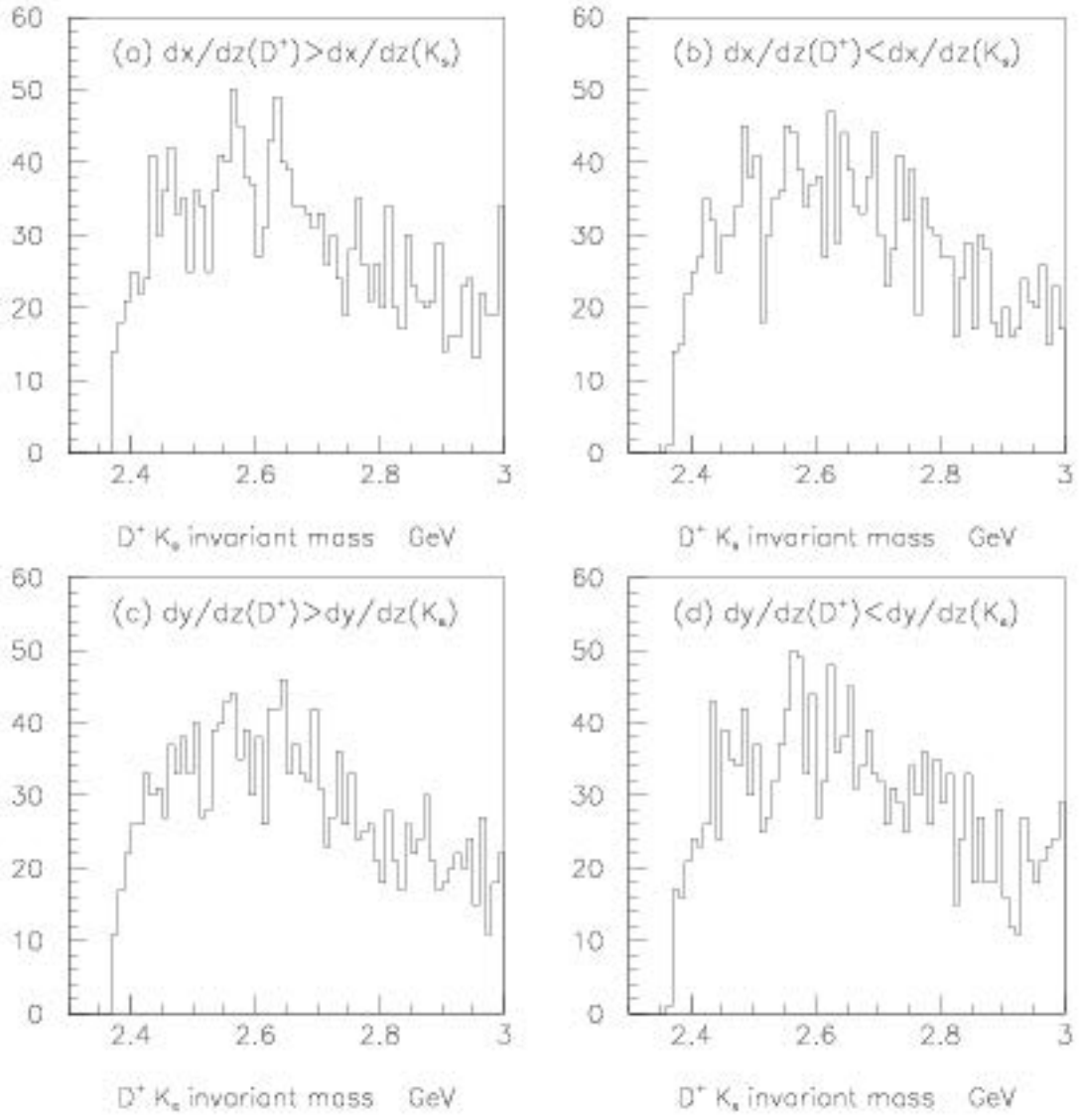

Figure 8.6: D^+K_s spectrum - check on alignment between SMD and Drift chamber systems

Table 8.3: Reconstruction Efficiencies for D_s^{**}

Decay mode	events generated	events reconstructed	MC efficiency	Total Efficiency
$D^+(K\pi\pi)\ K_s(\pi^+\pi^-)$ (2573 MeV/c^2)	49496	1003	0.0203	0.0131 ± 0.0004
$D^+(K\pi\pi)\ K_s(\pi^+\pi^-)$ (2640 MeV/c^2)	47895	890	0.0186	$0.0120 \pm .0.0004$
$D^0(K\pi)\ K^+$ (2573 MeV/c^2)	14831	472	0.0318	0.0155 ± 0.0006
$D^0(K\pi)\ K^+$ (2640 MeV/c^2)	47317	1198	0.0253	0.0123 ± 0.0004

If both peaks are D_s^{**} states then the branching fractions to D^+K^0 and D^0K^+ should be equal. The efficiency of reconstructing each mode can be found from Monte Carlo events and is shown in Table 8.3. The Monte Carlo efficiencies are determined without using any Čerenkov cuts. The efficiencies of the Čerenkov cuts are obtained from data [37]. The number of events reconstructed in each mode is shown in Table 8.4.

The ratio of branching fractions is given by:

$$\frac{\Gamma(D_s^{**}(2573) \to D^+K^0)}{\Gamma(D_s^{**}(2573) \to D^0K^+)} = \frac{N_1/[\epsilon_1 * BR(D^+ \to K^-\pi^+\pi^+) * BR(K^0 \to \pi^+\pi^-)]}{N_2/[\epsilon_2 * BR(D^0 \to K^-\pi^+)]} \tag{8.1}$$

where N_1 and N_2 are the number of events in the lower mass peak of the D^+K_s and D^0K^+ spectra respectively and ϵ_1 and ϵ_2 are the efficiencies for reconstructing each mode. Using the values measured for these variables and the values of the D^+ and

Table 8.4: Number of Reconstructed Events D_s^{**}

Decay mode	Events in peak
$D^+(K\pi\pi)\ K_s(\pi^+\pi^-)$ (2573 MeV/c^2)	71 ± 23
$D^+(K\pi\pi)\ K_s(\pi^+\pi^-)$ (2640 MeV/c^2)	73 ± 27
$D^0(K\pi)\ K^+$ (2573 MeV/c^2)	116 ± 34
$D^0(K\pi)\ K^+$ (2640 MeV/c^2)	39 ± 26

D^0 branching fractions from the Particle Data Group [19] we get

$$\frac{\Gamma(D_s^{**}(2565) \to D^+K^0)}{\Gamma(D_s^{**}(2565) \to D^0K^+)} = 0.93 \pm 0.41 \tag{8.2}$$

Similarly for the higher mass peak we get

$$\frac{\Gamma(D_s^{**}(2645) \to D^+K^0)}{\Gamma(D_s^{**}(2645) \to D^0K^+)} = 2.5 \pm 1.8 \tag{8.3}$$

The peak at 2565 Mev/c^2 is consistent with being the $J^p = 2^+$ charm-strange meson. Better statistics are needed to make a definitive statement about the higher mass peak.

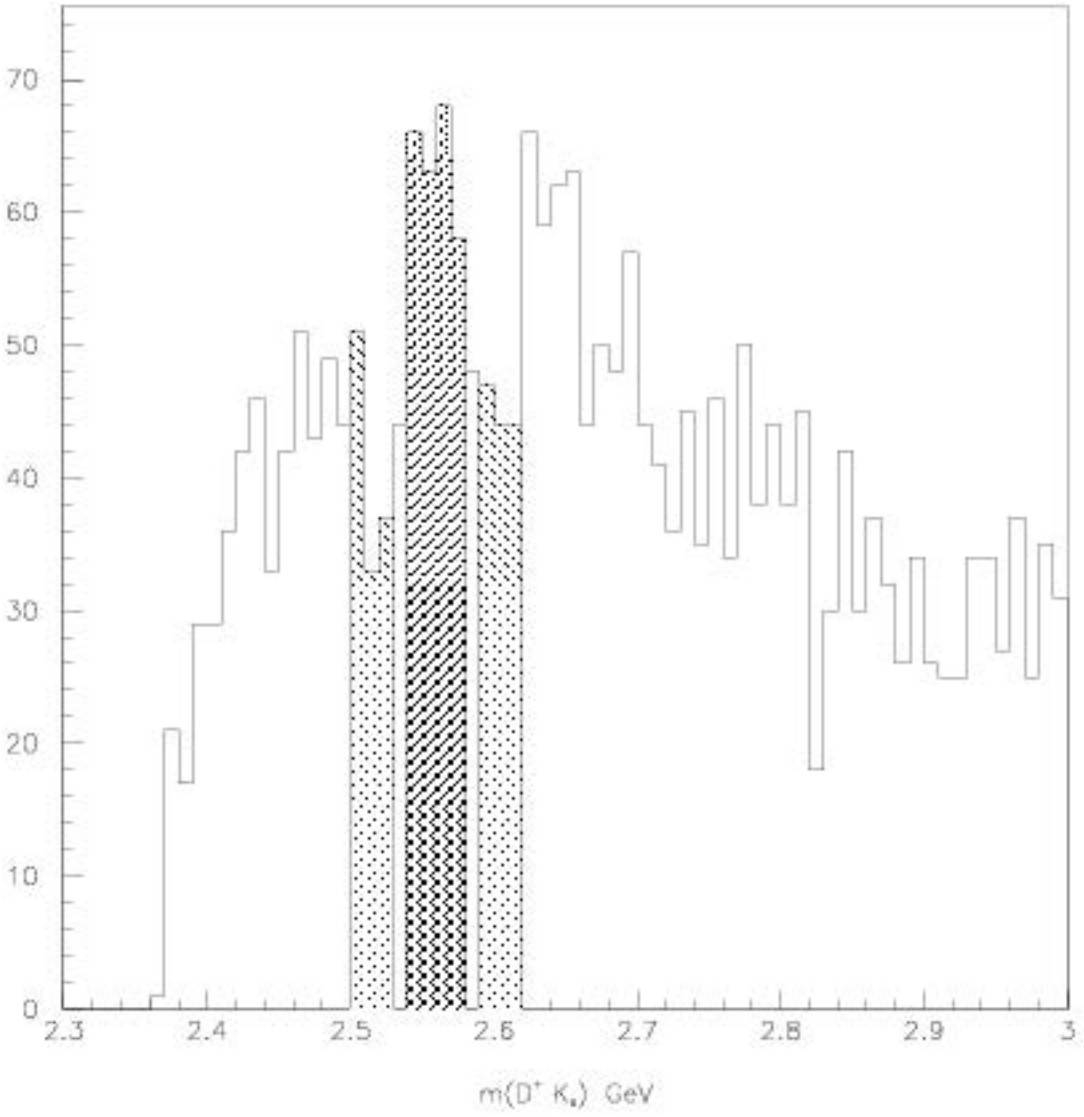

Figure 8.7: D^+K_s spectrum with signal and sideband regions shaded

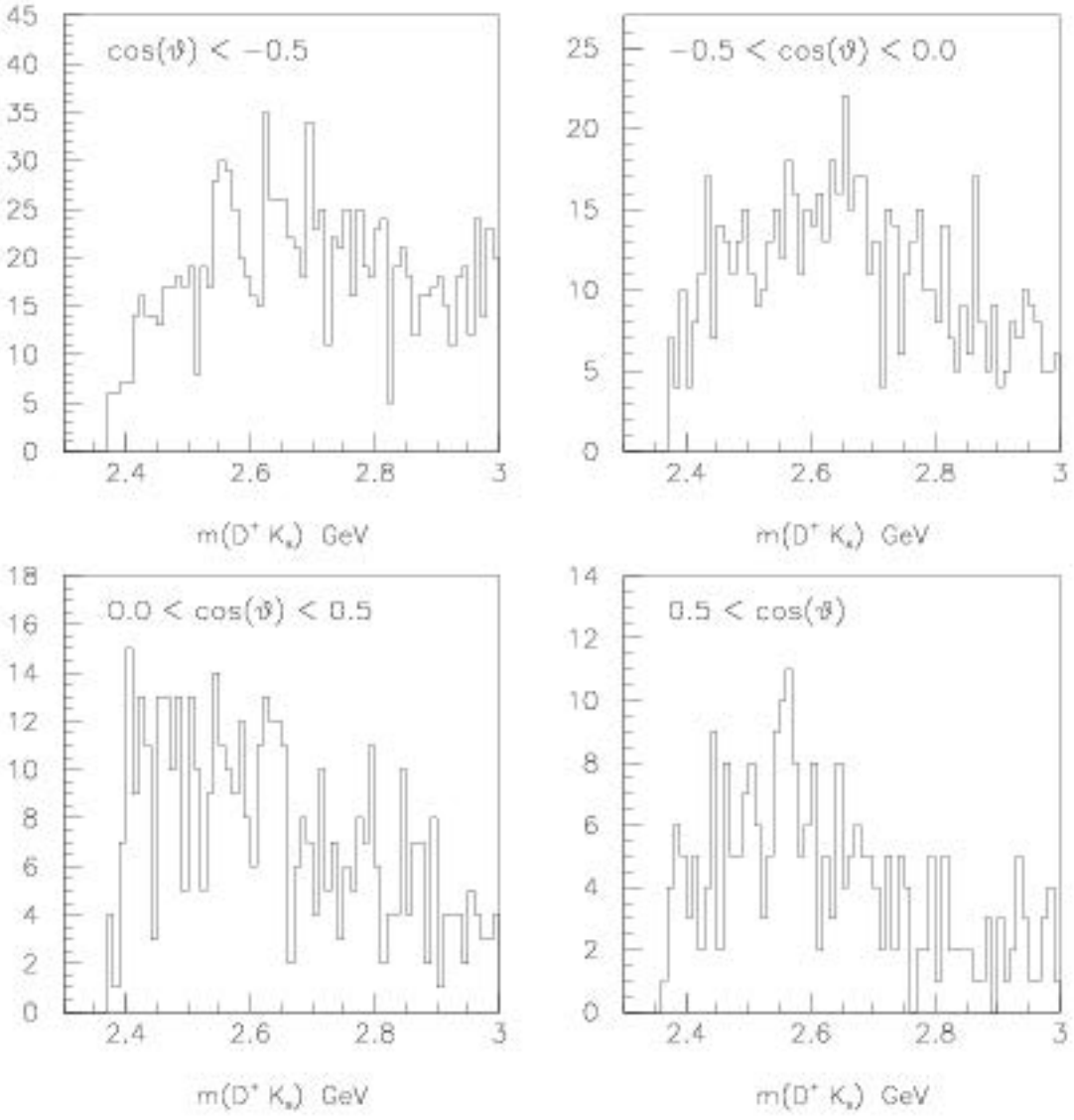

Figure 8.8: D^+K_s spectrum for different bins of $\cos(\theta)$

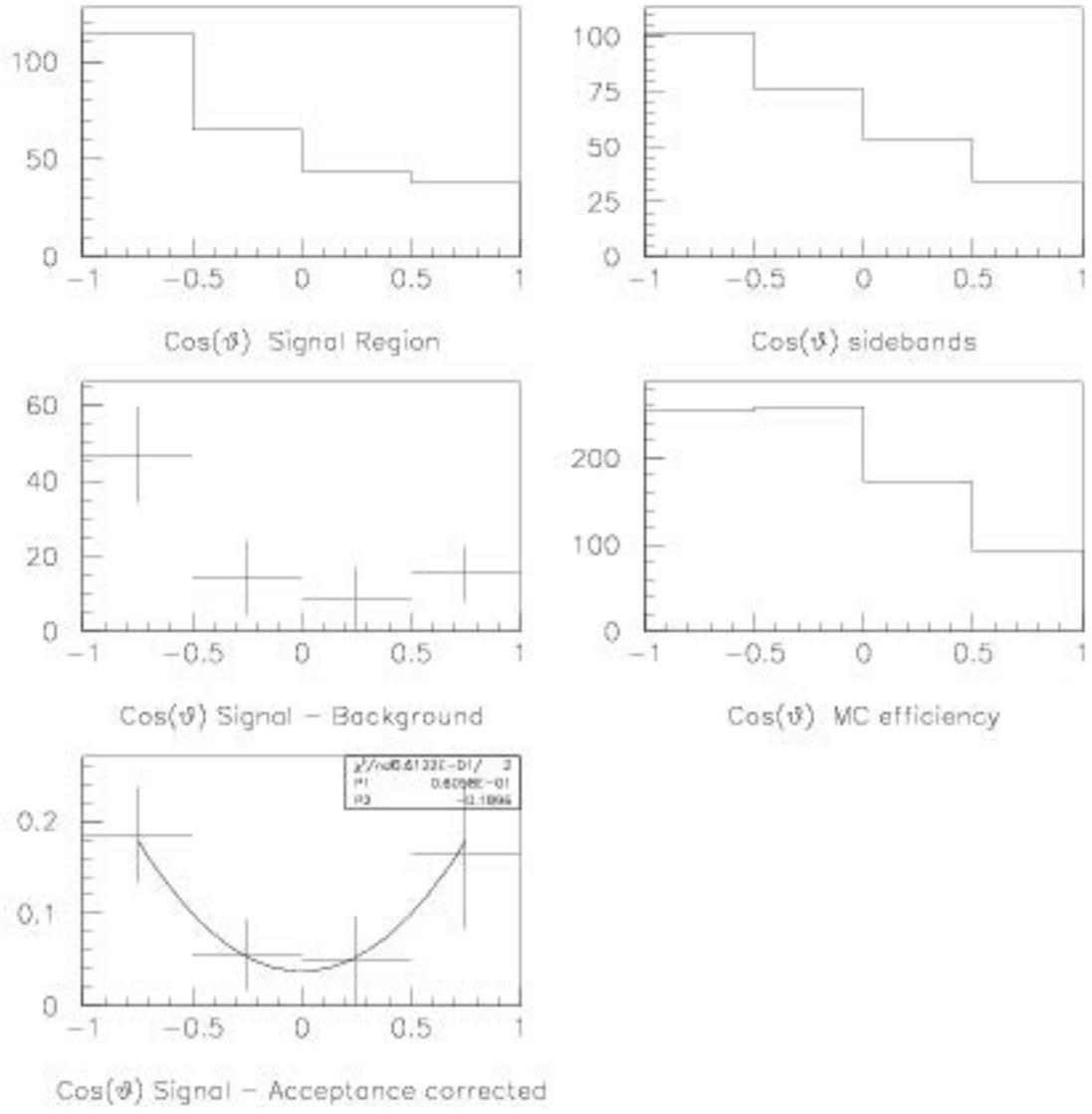

Figure 8.9: Angular distributions for D_s^{**} (a) signal region, (b) sidebands , (c) signal-background, (d) Monte Carlo signal, (e) Acceptance corrected signal

8.2 Angular distributions of D^+K_s and D^0K^+ decays

If we assume that the peak near 2565 Mev/c^2 is the 2^+ state we can measure the Falk-Peskin parameter, $w_{3/2}$, from the angular distribution of the kaons in the D^{**} rest frame. First I consider the D^+K_s mode. I tightened the Čerenkov cut on the kaon from the D^+ decay to get a somewhat cleaner peak. The new mass plot is shown in Figure 8.7, with the regions to be used for signal and background angular distributions shaded. The mass spectrum for different regions of $\cos\theta$ is shown in Figure 8.8. It can be seen in this figure that the low mass peak is predominately in the regions where $|\cos\theta| > 0.5$ but the high mass peak is more uniformly spread over the different bins of $\cos\theta$.

The angular distributions for the signal and background regions are shown in Figure 8.9 together with the background subtracted distribution for the signal region. This final distribution needs to be corrected for acceptance. The Monte Carlo events were created with a flat angular distribution so the measured distribution of the Monte Carlo events will give the experimental acceptance. Figure 8.9(d) shows the angular distribution of the Monte Carlo events with the same cuts as the data. Figure 8.9(e) shows the angular distribution for the signal with background subtracted and corrected for acceptance. The line is the best fit to the equation

$$const * [1 + 3\cos^2\theta - 6w_{3/2}(\cos^2\theta - 1/3)] \tag{8.4}$$

The measured value of the Falk-Peskin parameter $w_{3/2}$ for this decay mode is -0.18 ± 0.26.

Next we consider the D^0K^+ decay mode. The background angular distribution can be determined in two ways; either from the sidebands or from the wrong-sign D^0K^- spectrum. Figure 8.10 shows the D^0K^+ spectrum with the signal and sideband regions shaded. The dotted line shows the wrong-sign spectrum. Both methods of determining the background angular distribution have potential problems.

It can be seen from Figure 8.11 that the angular distribution of the lower mass

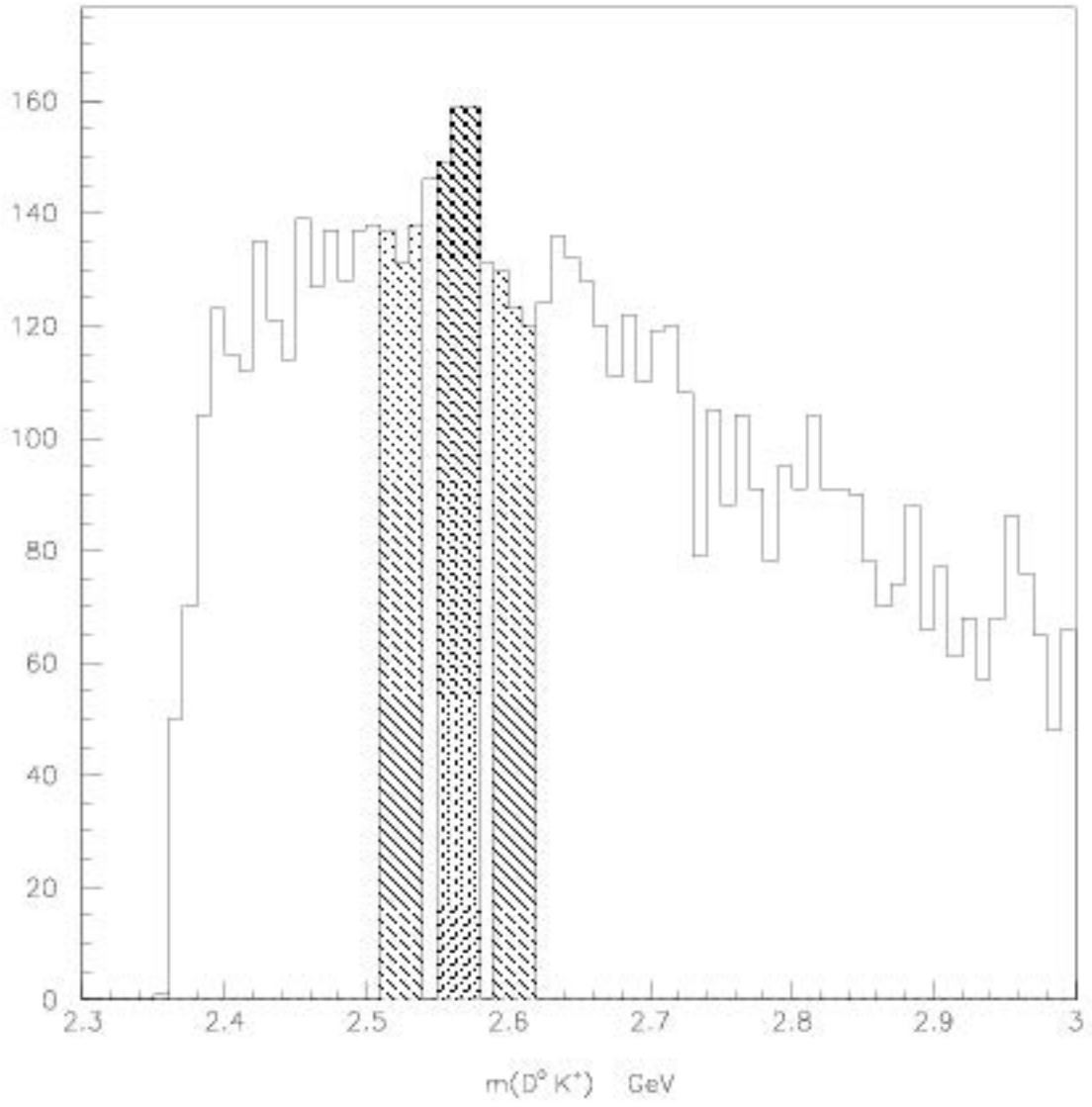

Figure 8.10: D^0K^+ spectrum: regions used for the signal and sideband angular distributions are shaded, the dashed line is the wrong-sign (D^0K^-) spectrum

sideband is very different from that of the higher mass sideband. It is not clear that summing these two distributions would give the best estimate of the angular distribution of the background under the signal.

It can be seen that the wrong-sign spectrum has fewer entries than the right-sign. This is because it is more likely for there to be two opposite sign kaons in an event than two same sign kaons. This can be compensated for by scaling the wrong-sign distribution by the ratio of the number of events estimated as background in the right-sign distribution over the number of events in the wrong-sign distribution. I estimate this to be $441/386 = 1.14$. Figure 8.11(c) shows the angular distribution of the wrong-sign background in the signal region.

Figure 8.12 shows the angular distribution of the right-sign signal region and that of the Monte Carlo signal. The signal − background distribution found by the two methods is shown in Figure 8.13 together with the fits of the acceptance corrected distributions to Equation 8.4. The results are $w_{3/2} = 0.18 \pm 0.30$ using the sideband background and $w_{3/2} = -0.17 \pm 0.30$ using the scaled wrong-sign background.

As $w_{3/2}$ is defined as a probability it must be greater than or equal to zero. A value of zero for $w_{3/2}$ implies that the D^{**}_{s2} is produced with zero population of the extreme helicity states $h = \pm 2$.

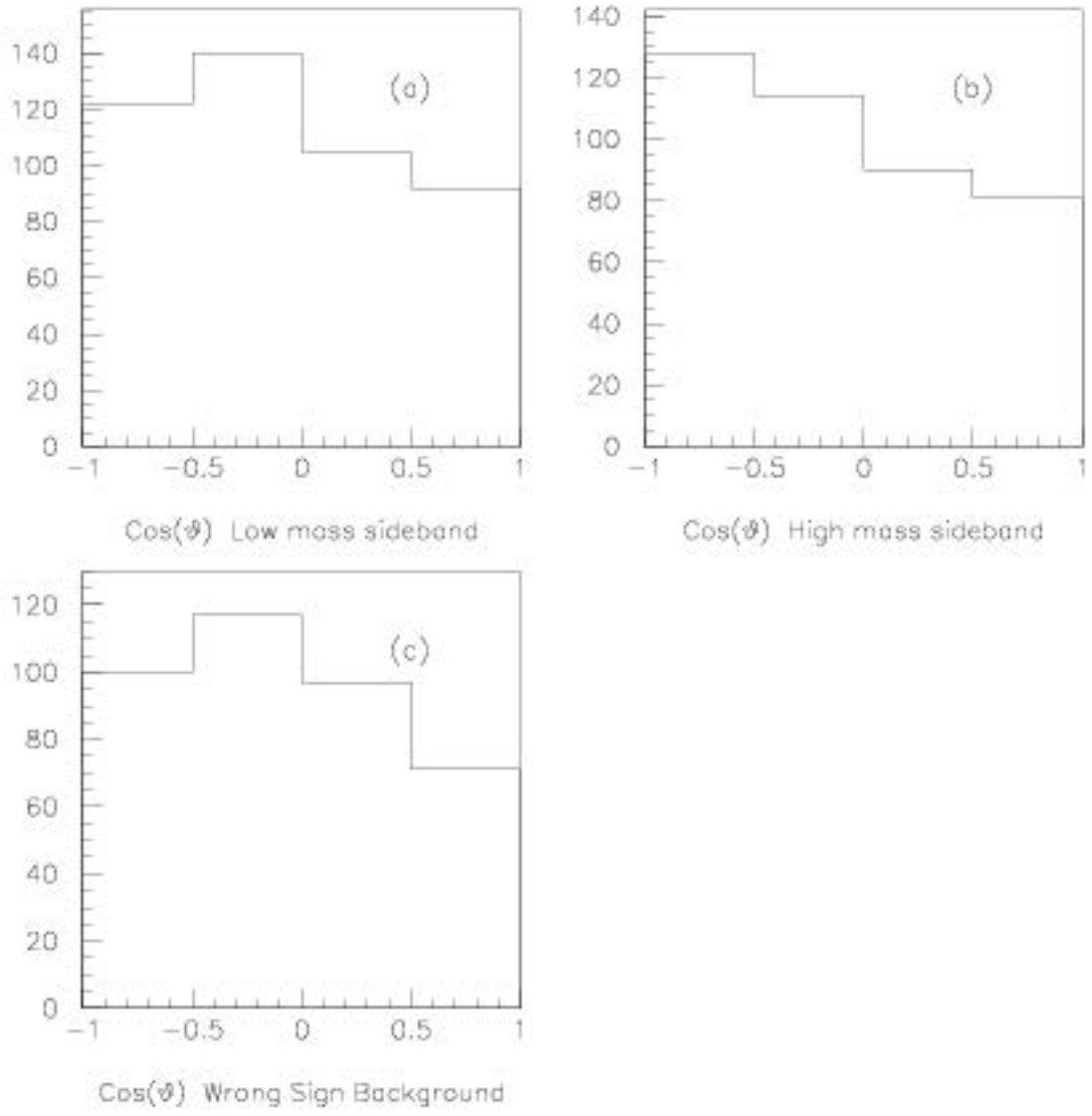

Figure 8.11: Background angular distributions for the D^0K^+ spectrum: (a) low mass sideband, (b) high mass sideband, (c) wrong-sign background

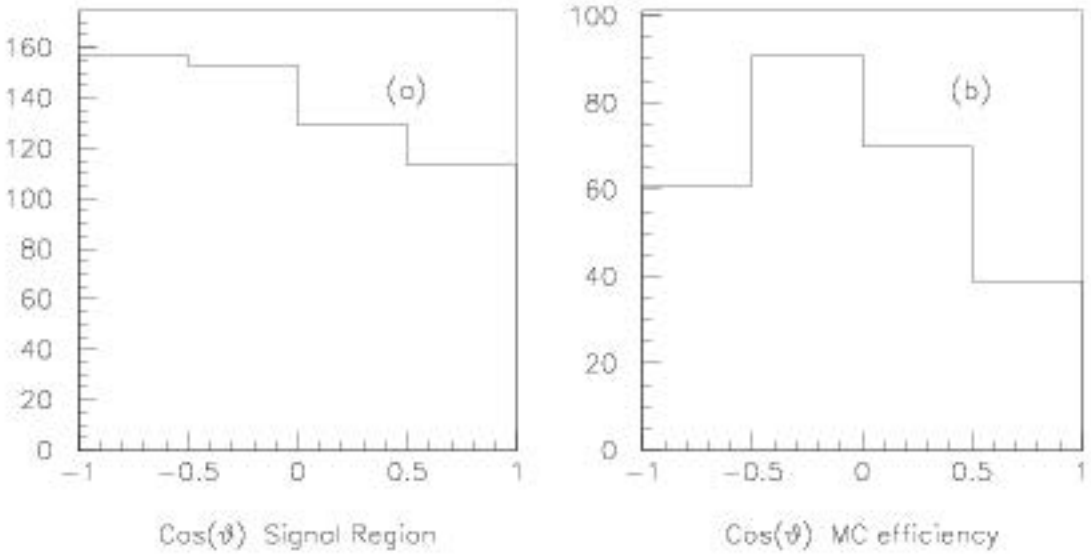

Figure 8.12: Angular distributions for peak at 2565 MeV/c^2 in D^0K^+ spectrum: (a) Signal Region - data, (b) Signal Region Monte Carlo

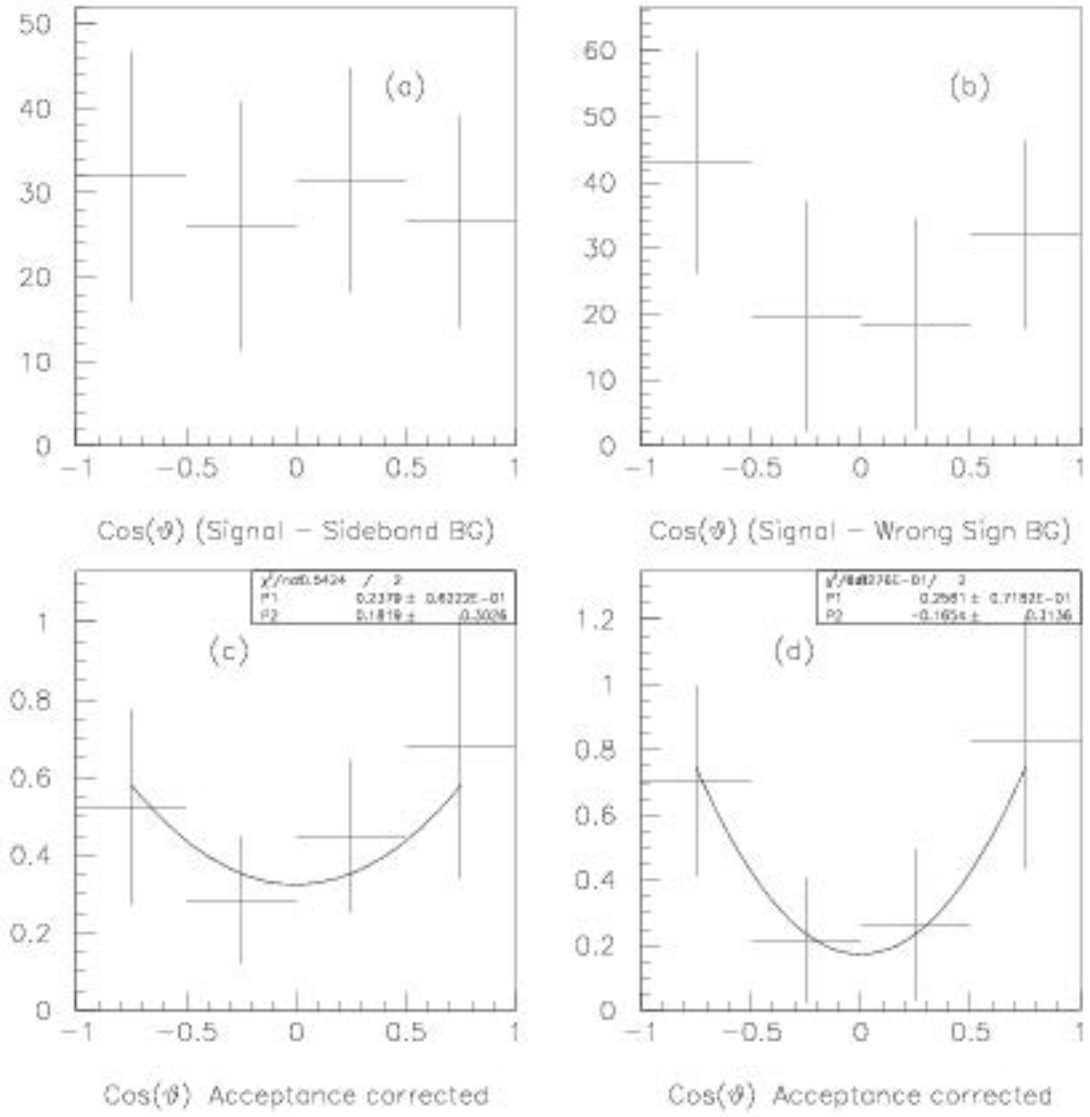

Figure 8.13: Angular distributions for peak at 2565 MeV/c^2 in D^0K^+ spectrum: (a) signal region minus background from sidebands, (b) signal region minus background from wrong-sign spectrum scaled by 1.14, (c) distribution in (a) corrected for acceptance, (d) distribution in (b) corrected for acceptance

Chapter 9

CONCLUSIONS

In this thesis I have reported the first observation of excited charm-strange mesons in a hadroproduction experiment.

The mass and width of the $D_s^{**}(2535)$ have been measured and compared to other experiments (see Table 9.1). The mass measured in E791, $(2533.6 \pm 1.4 \pm 0.3)$ MeV/c^2, agrees within errors but is slightly lower than that measured by other experiments. The other experiments find that the width of the peak is consistent with their resolution and only quote upper limits on the intrinsic width. It appears that our peak is wider than expected from our resolution alone but the errors are large and not inconsistent with a very narrow intrinsic width.

The angular distribution of the bachelor pion in the D^* rest frame with respect to the D^{**} direction is shown in Figure 7.7 and is consistent with being an S-wave decay of a $J = 1$ state.

We observe a peak in the D^0K^+ spectrum at 2565 MeV/c^2 which is consistent within errors with the peak observed by CLEO and ARGUS at 2573 MeV/c^2. We also observe a peak in the D^+K_s spectrum which adds confirmation to the state seen in D^0K^+. We measure the branching ratio between the two modes to be close to unity (0.93 ± 0.41) which is expected by isospin invariance. The peak in the D^+K_s decay mode has not been reported by any other experiment. The measured masses and widths are shown in Table 9.2 together with the results from CLEO and ARGUS. It is interesting to note that a state at 2564 MeV/c^2 decaying to D^*K (6 events) was

once claimed to have been seen in neutrino data from BEBC [42] however this was later retracted [17]. If the state at 2565 MeV/c^2 is a spin 2 state it would be expected to decay to both DK and D^*K. We do not see any evidence for a peak in the D^*K decay mode at 2565 MeV/c^2, however the branching fraction to D^*K is expected to be much smaller than that to DK [26].

If we assume that this state at 2565 MeV/c^2 is the $J^p = 2^+$ state, (its mass is close to the theoretically predicted mass), then it is meaningful to fit the angular distribution to equation 8.4 and get a measurment of the Falk-Peskin parameter $w_{3/2}$ [21]. Our results are shown in Table 9.3 and are consistent with Falk and Peskin's analysis of ARGUS data for the non-strange D^{**} state. It appears that the value of $w_{3/2}$ is close to zero which implies that the ${D_{s2}}^{**}$ is produced with zero population of the extreme helicity states $h = \pm 2$.

We also see some evidence of a peak at 2645 MeV/c^2 in both D^0K^+ and D^+K_s spectra. This peak has a significance of 3 standard deviations in the D^+K_s mode. The peak is not statistically significant in the D^0K^+ mode but is of interest because it is at the same mass as that in the D^+K_s mode. This peak is not seen by CLEO or ARGUS in their D^0K^+ spectra although there is a small excess of events in that region in both experiments and not inconsistent with there being a peak in that region. It is difficult to compare the results of E791 with those of CLEO and ARGUS as both production mechanisms and efficiency of reconstruction may differ greatly. Firstly CLEO and ARGUS are e^+e^- collider experiments where the center-of-mass energy is at one of the upsilon ($b\bar{b}$) resonances or nearby continuum, whereas E791 is a fixed target hadroproduction with a beam momentum of 500 GeV/c. The production ratios of different charm states could be quite different between e^+e^- annihilation and gluon-gluon fusion which is the dominant production mechanism in hadroproduction.

Secondly the cuts required to see the signal above background will be very different if the background is from different sources. In the collider experiments the heavy mesons are produced at low momentum in the lab frame and so the distance between the production and decay vertices cannot be used to identify the D^0 and D^+ states which decay weakly. However the multiplicity of the events is lower so there is less combinatoric background.

Table 9.1: Masses and Widths of the D_{s1}^{**} : E791 Results Compared with previous Experimental Measurements

Experiment	Decay Mode	Mass (MeV/c^2)	Width (MeV/c^2) (limits 90% CL)	# events
E791	$D^{*+}K^0$	$2533.6 \pm 1.4 \pm 0.3$	$5.0 \pm 3.6 \pm 2.3$	30 ± 7
ARGUS [10]	$D^{*+}K^0$	$2535.9 \pm 0.6 \pm 2.0$	<4.3	16 ± 6
ARGUS [10]	$D^{*0}K^+$	$2535.2 \pm 0.5 \pm 1.5$	<3.9	28 ± 10
CLEO II[8]	$D^{*+}K^0$	$2534.8 \pm 0.6 \pm 0.6$		44 ± 8
CLEO II [8]	$D^{*0}K^+$	$2535.3 \pm 0.2 \pm 0.5$	<2.3	134 ± 22
E687[16]	$D^{*+}K^0$ $D^{*0}K^+$	$2535.0 \pm 0.6 \pm 1.0$	<3.2	9 ± 3 44 ± 9
BEBC[17]	$D^{*+}K^0$,$D^{*0}K^+$	2534.2 ± 1.2	<2.3	44 ± 9

In the next two years charm data sets an order of magnitude larger will be available from Fermilab experiment FOCUS(E831) and from CLEO. The increased statistics should help confirm or reject the enhancement observed at 2645 MeV/c^2.

Table 9.2: Masses and Widths of the D_{s2}^{**} : E791 Results Compared with previous Experimental Measurements

Experiment	Decay Mode	Mass (MeV/c^2)	Width (MeV/c^2)	# Events
E791	D^+K^0	$2567 \pm 5 \pm 5$	$16 \pm 12 \pm 4$	71 ± 23
E791	D^0K^+	$2565 \pm 5 \pm 5$	$21 \pm 10 \pm 4$	116 ± 34
ARGUS [15]	D^0K^+	$2574.5 \pm 3.3 \pm 1.6$	$10.4 \pm 8.3 \pm 3.0$	93 ± 37
CLEO II [6]	D^0K^+	$2573.2 \pm 1.7 \pm 0.8$	$16 \pm 5 \pm 3$	217 ± 54

Table 9.3: Falk-Peskin Parameter $w_{3/2}$: E791 Results compared with previous measurement

Experiment	Decay Mode	$w_{3/2}$
E791	$D_{s2}^{**} \to D^+K^0$	-0.18 ± 0.26
E791	$D_{s2}^{**} \to D^0K^+$	0.005 ± 0.30
ARGUS [21]	$D_2^{**} \to D^0\pi^+$	-0.3 (<0.24 @90% CL)

Bibliography

[1] J. Rosner, "P-Wave Mesons with One Heavy Quark", *Comments Nucl. Part. Phys.* **16**, 109-129 (1986)

[2] N. Isgur and M. Wise, "Spectroscopy with Heavy-Quark symmetry", *Phys. Rev. Lett* **66**, 1130-1133 (1991)

[3] ARGUS Collaboration, [1] H. Albrecht et al., "Observation of a New Charmed Meson", *Phys. Rev. Lett.* **56**, 549-552 (1986)

[4] Fermilab E691 Collaboration[1], J. C. Anjos et al., "Observation of Excited Charmed Mesons", *Phys. Rev. Lett.* **62**, 1717-1720 (1989)

[5] CLEO Collaboration[1], P. Avery et al., "P-Wave charmed mesons in e^+e^- annihilation", *Phys. Rev. D* **41**, 774-784 (1990)

[6] CLEO Collaboration[1], Y. Kubota et al., "Observation of a New Charmed Strange Meson", *Phys. Rev. Lett.* **72**, 1972-1975 (1994)

[7] CLEO Collaboration[1], P. Avery et al., "Production and decay of $D_1(2420)^0$ and $D_2^*(2460)^{0m}$", *Phys. Lett. B* **331**, 236-239 (1994)

[8] CLEO Collaboration[1], J.P. Alexander et al., "Production and Decay of the $D_{s1}^+(2536)$", *Phys. Lett. B* **303**, 377-340 (1993)

[9] ARGUS Collaboration[1], H. Albrecht et al., "Observation of the $D^{*0}(2459)$ in e^+e^- Annihilation", *Phys. Lett. B* **221**, 422-426 (1989)

[1] These references have more than 50 authors, only the first author is listed here

[10] ARGUS Collaboration[1], H. Albrecht et al., "Observation of a new Charmed-Strange Meson", *Phys. Lett. B* **230**, 162-166 (1989)

[11] ARGUS Collaboration[1], H. Albrecht et al., "Observation of the Charged Isospin Partner of the $D^*(2459)^0$", *Phys. Lett. B* **231**, 208-212 (1989)

[12] ARGUS Collaboration[1], H. Albrecht et al., "Resonance Decomposition of the $D^*(2420)^0$ through a Decay Angular Analysis", *Phys. Lett. B* **232**, 398-402 (1989)

[13] ARGUS Collaboration[1], H. Albrecht et al., "Observation of a new charmed Baryon", *Phys. Lett. B* **317**, 227-331 (1993)

[14] ARGUS Collaboration[1], H. Albrecht et al., "Reconstruction of the Decay $B^- \to D_1^0(2414)\pi^-$" *Phys. Lett. B* **335**, 527-531 (1994)

[15] ARGUS Collaboration[1], H. Albrecht et al., *Measurement of the Decay* $D(s2)^{*+} \to D^0K^+$, DESY-95-129, July 1995

[16] Fermilab E687 Collaboration[1], P.L.Frabetti et al., "Measurement of the Masses and Widths of $L = 1$ Charmed Mesons", *Phys. Rev. Lett.* **72**, 961 (1994)

[17] A. Asratyan et al.[1], " Observation of $D_s^{**}(2536)$ meson production by neutrinos in BEBC," *Z. Phys. C* **61**, 563-566 (1994)

[18] DELPHI Collaboration[1], "Observation of Orbitally Excited B Mesons", *Phys. Lett. B* **345**, 598-602 (1995)

[19] Particle Data Group, "Review of Particle Properties", *Phys. Rev. D* **50**, 1173-1826 (1994)

[20] Shekhar Shukla, *Excited Charm States*, FERMILAB-Conf-94/401

[21] A. F. Falk and M. E. Peskin, "Production, decay, and Polarization of excited heavy mesons", *Phys. Rev. D* **49**, 3320-3332 (1994)

[22] Tzu Chiang Yuan, *Helicity Probabilities For Heavy Quark Fragmentation into Excited Mesons*, U. C. Davis preprint UCD-94-26

[23] Tzu Chiang Yuan, *Helicity Probabilities For Heavy Quark Fragmentation into Heavy-Light Excited Mesons*, UCD-95-7

[24] T. Appelquist and H. D. Politzer, "Heavy Quarks and e^+e^- annihilation", *Phys. Rev. Lett* **34**, 43-46 (1975);

[25] T. Appelquist,A. De Rujula, H. D. Politzer, S. L. Glashow, "Charmonium Spectroscopy", *Phys. Rev. Lett* **34**, 365-368 (1975)

[26] S. Godfrey and R. Kokoski, "Properties of P-Wave mesons with one heavy quark", *Phys. Rev. D* **43**, 1679 (1991)

[27] A. De Rujula et al., "Charm Spetroscopy via Electron-Positron Annihilation", *Phys. Rev. Lett.* **37**, 785-788 (1976)

[28] E. Eichten, C.T. Hill and C. Quigg, *Spectra of Heavy-Light Mesons*, Fermilab Report No. FERMILAB-CONF-94/117-T

[29] E. Eichten, C.T. Hill and C. Quigg, *Orbitally Excited Heavy-Light Mesons Revisited*, FERMILAB-CONF-94/118-T

[30] R. Jedicke, *Flavour Dependence of Hadroproduced Charm-Strange Mesons*, PhD. Thesis, University of Toronto, Canada (1991) (unpublished)

[31] R. Yamada, "FERMILAB Magnet Mapping System", *Nuc. Instr. and Methods* **138**, 567-599 (1976)

[32] D.J. Summers, *A Study of the Decay $D^0 \to K^-\pi^+\pi 0$ in High Energy Photoproduction*, PhD. Thesis, University of California, Santa Barbara (1984) (unpublished)

[33] D. Bartlett et al.[1], "Performance of the Cerenkov Counters in the Fermilab Tagged Photon Spectrometer Facility", *Nuc. Instr. and Methods* **A260**, 55-85 (1987)

[34] V. K. Bharadwaj et al.[1], "A Large Area Liquid Scintillation Multi-Photon Detector", *Nuc. Instr. and Methods* **228**, 283-297 (1985)

[35] S. Amato, J. de Mello Neto, J. de Miranda, C. James, D. Summers, S. Bracker, "The E791 Parallel Architecture Data Acquisition System", *Nuc. Instr. and Methods* **A324**, 535-551 (1993)

[36] H. -U. Bengtsson and T. Sjostrand, *Computer Physics Commun*, **46**, 43-501 (1987)

[37] H. da Silva Carvalho, *E791 Čerenkov Kaon ID Efficiency Study*, E791 Document 223, April 1995 (unpublished)

[38] Arun Tripathi, *A Compilation of the Cuts used in the Release 6 Strip*, E791 Document 115, April 1995 (unpublished)

[39] C. James and J. Slaughter, *Content and Usage of Release 7 Filtering*, E791 Document 123, April 1995 (unpublished)

[40] J. Slaughter, *Release 7.1 Stripping Instructions and Description*, E791 Document 156, April 1995 (unpublished)

[41] S. Kwan, *A Study of* Σ_c *Production in E791* , E791 Document 232, September 1995 (unpublished)

[42] A. Asratyan et al.[1], "Studying $(\bar{c}s)$ Spectroscopy in $\bar{\nu}N$ collisions," *Z. Phys.* **40**, 483-486 (1988)